Årgang LXXXVII, Nr. 2-4, juni 2016

BYGNINGSSTATISKE MEDDELELSER

udgivet af

DANSK SELSKAB FOR BYGNINGSSTATIK

Proceedings of the Danish Society for Structural Science and Engineering

KØBENHAVN 2016

ISSN 0106-3715 (trykt udgave)

ISSN 1601-6548 (online)

Årgang LXXXVII, Nr. 2-4, juni 2016

BYGNINGSSTATISKE MEDDELELSER

udgivet af

DANSK SELSKAB FOR BYGNINGSSTATIK

Proceedings of the Danish Society for Structural Science and Engineering

KØBENHAVN 2016

Artikler offentliggjort i Bygningsstatiske Meddelelser har gennemgået review.

Papers published in the Proceedings of the Danish Society for Structural Science and Engineering have been reviewed.

Bridge Deck Flutter Analysis

BYGNINGSSTATISKE MEDDELELSER
Proceedings of the Danish Society for Structural Science and Engineering
Edited and published by the Danish Society for Structural Science and Engineering
Volume 87, No. 2-4, 2016, pp.37-123

Bridge Deck Flutter Analysis

Allan Larsen [1]

1. Introduction

This thesis presents a review of theoretical analysis of bridge deck flutter. The objective is partly to present the authors original contribution to the analysis of one-degree-of-freedom torsion flutter, partly to present an update of classical two-degree-of-freedom flutter analysis. This involves extension into three-degrees-of-freedom by including horizontal modes and an evaluation hereof considering three cases of cable supported bridges. The presentation is self-contained emphasizing the underlying physics of the flutter problems discussed. Much of the development in bridge flutter analysis within the past three decades is scattered in scientific journals and conference proceedings and is less accessible to newcomers. The thesis attempts to improve on this situation by offering a storehouse of concepts and methods available to the flutter analyst. Wind tunnel techniques applied in flutter testing of bridge decks is only covered in sufficient detail to illustrate how experimental data needed for analysis is obtained.

2. Definition of Bridge Deck Flutter

Flutter refers to a condition by which a bridge deck becomes unstable and oscillates in an otherwise steady wind flow. The phenomenon is often divided in two categories according to the physics involved: 1) One-degree-of-freedom flutter or "torsion flutter" and 2) Two-degree-of-freedom flutter or "classical flutter", although some controversy exists over the use of the term one-degree-of-freedom flutter. For One-degree-of-freedom flutter the wind loading causes the bridge girder to oscillate in pure torsion at a frequency equal to the eigenfrequency of the structural torsion mode. The response will grow approximately linearly with increasing wind speed once a threshold wind speed is exceeded. Two-degree-of-freedom combines torsion and bending oscillations at a common frequency in between the structural eigenfrequencies of the participating modes. The response will grow exponentially with increasing wind speed once the threshold or critical wind speed is exceeded.

[1] BSc, PhD, COWI A/S, Copenhagen

3. Historical Background

3.1 Early suspension bridges

Early suspension bridges in Europe and North America had a strange tendency to be damaged or destroyed by storm winds. From 1818 to 1889 a total of 10 suspension bridges were seriously damaged some of them several times. On 29th November 1836 the third span of the Brighton Chain Pier was wrecked in a storm described as being as strong as a tropical hurricane by Lieutenant Colonel Reid of the Royal Corps of Engineers. In a written record of the incident, Reid describes how oscillations of the bridge deck preceded the fatal "undulating motion" shown in an accompanying sketch Figure 3.1. To the trained eye the sketch displays the first asymmetrical vertical or torsion eigenmode of a typical suspension bridge indicating that the collapse was linked to dynamic resonant excitation.

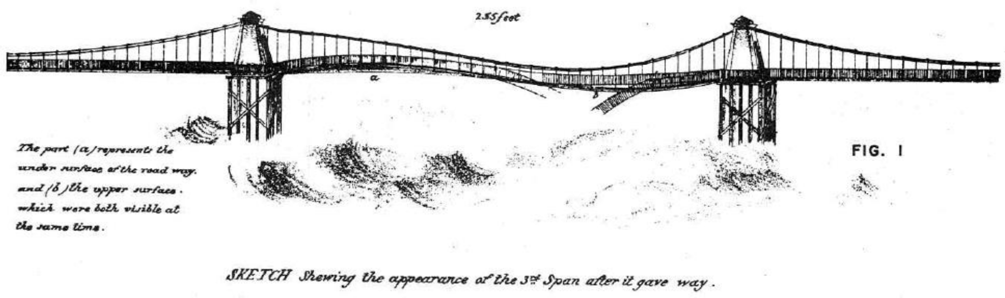

Figure 3.1 Fatal undulating motion of the third span of the Brighton Chain Pier in the storm of 1836 sketched by Ried (J.S. Russell, 1839).

The Menai Strait Bridge in North Wales, UK is another historic suspension bridge that suffered severe damage in storms in 1826, 1836 and 1839. The resident engineer Provis [1] describes the first incident in 1826 as follows: "*The motion which had been anticipated was that of a simple undulation flowing in right angles to the length of the bridge* (along the span) … *The movement of this undulating wave, however, was oblique with the general direction of the bridge. In other words, when the summit of the wave was at a given point on the windward side of the bridge, it was not opposite this point on the leeward side, but, in relation to the flow of the wave, considerably behind it; the motion appearing to be generated on the windward side, and by the time it had crossed to the leeward it had moved forward along that on which it had commenced… The motion was observed to be greatest about half way between the pyramids* (the towers) *and the centre of the bridge. The wave increased in its progress from the pyramid till it attained its maximum amplitude at the first quarter, and at the same instant the extreme depression was near the third quarter. The wave then gradually diminished to the centre of the bridge and afterwards increased to the third quarter, when it attained its greatest height at the same time that the first quarter was most depressed. The platform (*the deck*) and the main chains were equally subjected to* *this undulatory motion"*. On the amplitudes attained by the bridge in the 1836 storm Provis writes: "*It is not easy to define correctly the rise and fall of the roadway, but the bridge keeper stated that there was a little less than 16 feet (*5.3 m*) between the extreme rise and the lowest point of depression*". Figure 3.2 shows a sketch prepared by the author according to the observations above. Again it is noted that the bridge must have moved in the first asymmetrical torsion eigenmode perhaps combined with the vertical bending mode indicating one or two-degree-of-freedom flutter respectively.

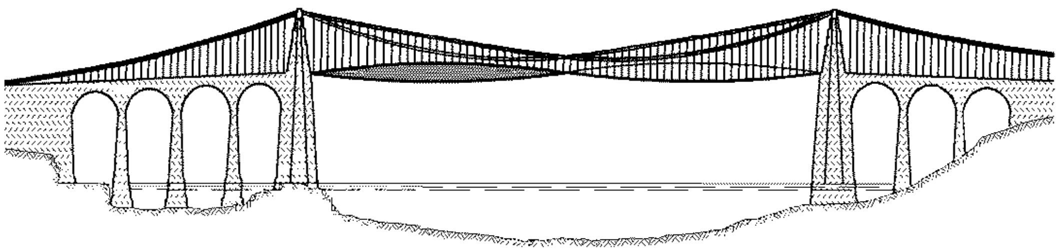

Figure 3.2 Authors' sketch of the undulations of the Menai Bridge in the storms of 1826 and 1836 as inferred from the bridge keepers account.

The wrecking of the early suspension bridges by high winds did not promote theoretical research into the observed behavior. One reason being that the science of aerodynamics had not matured to an understanding of how forces (crosswind) were to develop on a structure perpendicular to the general direction of the wind flow. The necessary physical understanding coined in the Kutta-Jukowski theorem which then turned potential flow theory into a powerful aerodynamic tool emerged only as the 19th century turned into the 20th century.

The Victorian bridge engineers responded to the wind susceptibility of their structures by increasing the stiffness of the bridges by adding stiffening trusses in conjunction with the roadway decks. This without knowing exactly what stiffening of the structure accomplished in terms of aerodynamic stability. However, the stiffening truss proved effective for securing wind stability but at the expense of materials and increased construction costs.

3.2 The Tacoma Narrows Bridge collapse

A little more than 50 years went by from the collapse of the Niagara-Clifton suspension bridge in a storm in 1889 to the spectacular collapse of the Tacoma Narrows suspension bridge in a 19 m/s gale in 1940. The Tacoma Narrows Bridge had been oscillating vertically in the wind from its opening on 1 July 1940 to the amusement of the public who nicknamed the bridge "Galloping Gertie" but to great concern of the engineers. In order to gain insight into the motions the bridge was monitored by motion picture cameras, which ensured the astonishing and now world famous footage of the oscillations leading to the collapse of the bridge on 7 November 1940.

Figure 3.3 Catastrophic torsion oscillations of the Tacoma Narrows Bridge, 7 November 1940. (top row) view from a quartering angle. (bottom row) view along the deck. Tacoma Camera Shop.

Figure 3.3 reproduces single frames approximately 2.5 sec. apart extracted from the movie issued by the Tacoma Camera Shop, demonstrating that the fatal oscillations was in the asymmetrical torsion eigenmode at 0.2 Hz and that the deck twisted about 30 - 35 deg. at the quarter span points, very similar to what is sketched for the Menai Bridge in Figure 3.2.

Two days after the collapse the Federal Works Administration initiated a thorough investigation led by Amman, von Kármán and Woodruff the foremost experts of the day in suspension bridge design, aerodynamics and structural engineering. The outcome of the investigation sometimes referred to as the Carmody report [2] was delivered on 28th March 1941. The report's conclusion on tests of an elastically suspended section model of the bridge at California Institute of Technology (GALCIT) states: *Convincing evidence from the oscillatory tests are that beyond a certain wind velocity negative aerodynamic damping is to be expected in almost any suspended bridge structure when it oscillates torsionally*. A condition named "self-induced" oscillations. Flow visualization pictures, Figure 4.24, demonstrated that large vortex structures were formed alternatively on the upper and lower sides of the roadway when the deck section model was oscillating in torsion.

Besides stating the now obvious fact that: "*The Tacoma Narrows Bridge failure resulted from excessive oscillations caused by wind action*" and the attempt to clarify the aerodynamic mechanisms involved in the collapse quoted above, the Carmody report concluded that: "*Further experiments and analytical studies are desirable to investigate the action of aerodynamic forces on suspension bridges*". The latter conclusion prompted the construction of the suspension bridge wind tunnel laboratory at the University of Washington that conducted elaborate tests on a 1:50 scale full aeroelastic bridge model of the original bridge to further study the aerodynamics involved in the collapse. More important the laboratory conducted extensive full aeroelastic model tests to verify the wind resistance of the new truss stiffened suspension bridge to be built as a replacement for "Galloping Gertie" [3].

3.3 Development of theoretical flutter analyses of bridge deck

The first attempt to apply theoretical aerodynamic analysis to bridge deck flutter known to the author is due to Bleich in 1948 [4] who worked as a consultant to the Federal Works Administration during the Tacoma Narrows investigations. Bleich noted an important aspect of the GALCIT wind tunnel tests of elastically suspended  shaped section models similar to the Tacoma Narrows but with varying edge girder depth to deck width ratio d/B. For d/B > 6% all models tested displayed "self-induced" torsion oscillations at a frequency equal to the still air frequency starting at some threshold wind speed but with amplitudes growing proportionally to the wind speed once the threshold was exceeded. For section models having d/B < 6% "self-induced" oscillations also started at some but different threshold wind speed. However, the oscillations now took on a combined vertical bending / torsion form at a common frequency in between the still air vertical bending and torsion frequencies. This characteristic is similar to flutter of wing sections (sometimes referred to as classical flutter or two-degree-of-freedom-flutter) for which Theodorsen [5] developed a very successful theoretical treatment 13 years earlier (the flat plate theory). Bleich noted that the truss-stiffened section tested for the new Tacoma Narrows Bridge also displayed classical flutter indicating that the truss located under the roadway deck was of little importance for aerodynamic instability. Thus, classical flutter was the aerodynamic instability mode to be considered for future suspension bridges. Besides presenting an operational method for calculation of flat plate wind speeds of bridge decks Bleich also proposed an extension of the flat plate theory to include oscillatory aerodynamic forces generated at the windward edge of the girder. This theoretical extension required determination of two empirical constants from wind tunnel tests, which however proved difficult in practice.

Theodorsens flat plate flutter theory predicts the threshold wind speed for onset of flutter, which is a governing parameter in the design of long span cable supported bridges. The method is somewhat complicated to apply to practical design cases if the analyst does not have access to a computer, as it requires determination of the roots of a third and a fourth order algebraic equation. To make flutter speed calculations more accessible to practitioners Selberg [6] proposed a simple formula for the critical wind speed for onset of flutter based on Bleichs adaptation of Theodorsens theory. Selbergs formula (to be discussed in section 5.8) is remarkable in the sense that it only incorporates the structural parameters of the bridge as variables (mass, mass moment of inertia, eigenfrequencies and deck width). All aerodynamic information is lumped in just one constant.

Design of the Severn suspension bridge in UK and the Lillebælt suspension bridge in Denmark in the 60ies saw development of a new type of bridge deck cross section the trapezoidal or semi-streamlined box girder. Aerodynamically this type of cross section behaves even more like a flat plate than the truss sections studied by Bleich. The advent of the semi-streamlined deck prompted Frandsen [7] to take a new graphical approach to the solution of Theodorsens flat plate equations and to study the range of validity of Selbergs formula. Frandsens graphical method is very simple use and his calculations established that Selbergs formula is accurate for torsion to vertical bending frequency ratios larger than 1.5.

The realization that bridge deck sections in general are aerodynamically different from flat plates or airfoils let Scanlan and Tomko [8] to re-launch Theodorsen´s theory but now with the theoretically determined aerodynamic flutter coefficients preplaced by experimental data obtained from wind tunnel testing of bridge deck section models. The aerodynamics of the deck sections is captured in six coefficients $A^*_{1..3}$, $H^*_{1..3}$ (often referred to as aerodynamic derivatives) measured as function of the non-dimensional wind speed. These coefficients allows a clear distinction between the aerodynamics of one-degree-of-freedom and two-degree-of-freedom flutter, Figure 3.4. The flutter coefficients of the airfoil (labelled A) all display an increase with increasing non-dimensional wind speed V/NB where $V$is wind speed $N$is frequency and $B$is deck width, a behavior indicating two-degree-of-freedom flutter. Deck section 4, the deep truss, displays a similar aerodynamic behavior in the sense that the A^*_2 (the aerodynamic damping in torsion) and the A^*_3 (the aerodynamic stiffness in torsion) displays similar behavior as the airfoil thus two-degree-of-freedom flutter is expected for this deck. Deck section 1, the original Tacoma Narrows Bridge, behaves distinctly different. The A^*_2 coefficient starts out being negative as is the case for the airfoil however, at some non-dimensional wind speed it changes sign to become positive, which is an indication of one-degree-of-freedom flutter. It is also noted that the aerodynamic stiffness coefficient A^*_3 for the Tacoma section is negligible indicating that torsion flutter will occur at the same frequency as the structural eigenfrequency in absence of wind. Deck sections 2 and 3 displays both monotonically increasing A^*_3 coefficients and zero crossing of A^*_2 indicating that the flutter mode for these decks will depend on which aerodynamic phenomenon sets in at the lowest non-dimensional wind speed. Scanlan and Tomkos approach to flutter analysis will be discussed in much more detail in section 5.

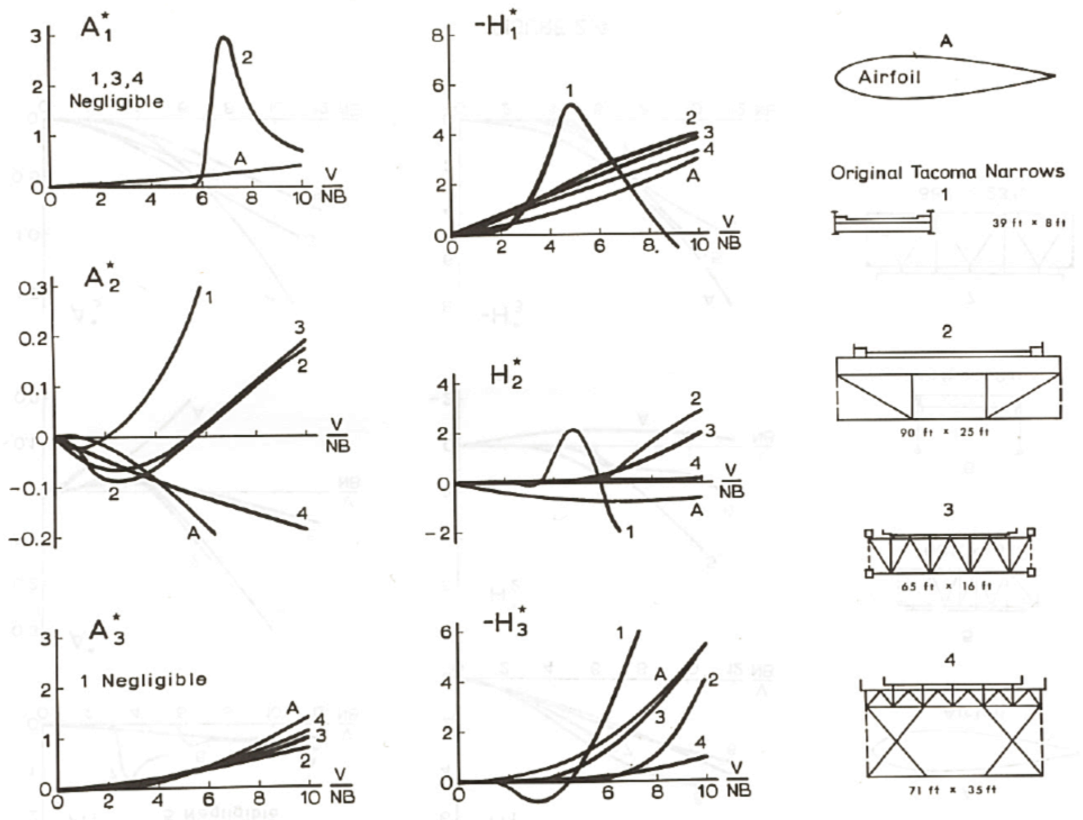

Figure 3.4 Flutter coefficients or aerodynamic derivatives measured for different bridge deck sections. Adapted from [8].

4. One-degree-of-freedom Flutter

Following the Tacoma Narrows incident designers shied away from plate girders with deep facia beams for long span suspension bridges and with good reason. Plate girder deck sections akin to a shallow H or an inverted channel (sometimes referred to as π-sections) are however, still very popular for medium span cable-stayed bridges on the account of economy and constructability. For these types of bridges, the torsion stiffness can often be enhanced considerably by anchoring the cable-stays at the edges of the girder and thus secure a high critical wind speed for flutter. Notable examples of bridges featuring plate girder cross sections are Alex Fraser (Canada), Busan-Goje (Korea), Second Severn and Kessock (UK). Evaluation of flutter of plate girder bridges during design relies on direct wind tunnel testing or extraction of flutter derivatives form the literature for decks of similar geometry. This chapter presents an analytical treatment of the one-degree-of-freedom flutter problem with the objective of understanding the physics involved and arriving at a simple formula for the critical wind speed similar to the Selberg formula applicable to two-degree-of-freedom-flutter. In order to pursue this goal some fundamental mechanical concepts and results from the original Tacoma Narrows wind tunnel tests will be revisited.

4.1 Work supplied to a rotary mechanical system

Fundamental mechanics defines the instantaneous power at time (t) supplied by an external moment rotary mechanical system as:

$$P(t) = M(t)\dot{\alpha}(t) \tag{4.1}$$

Where $M(t)$ is the external moment and $\dot{\alpha}(t)$ is the angular velocity which are both functions of time t. As power is the time derivative of work:

$$P = \frac{dW}{dt} \tag{4.2}$$

The work done by the external moment over a time interval t_0 to t is obtained as:

$$W = \int_{t_0}^{t} M(t)\dot{\alpha}(t)dt \tag{4.3}$$

As a basic example, let us consider the work dissipated by viscous damping during one period of stationary rotary oscillations. The moment $M_d(t)$ supplied by viscous damping is proportional to the angular velocity which is $\pi/2$ phase shifted relative to the angular displacement $\alpha(t) = \alpha\sin(\omega t)$:

$$M_d(t) = \frac{\delta_s}{\pi} I\omega^2\alpha\cos(\omega t) = \frac{\delta_s}{\pi} I\omega^2\alpha\sin(\omega t - \pi/2) \tag{4.4}$$

Where ω is radian frequency, δ_s is the logarithmic decrement and I is the mass moment of inertia of the oscillating body. The work dissipated by viscous damping over one circle of oscillation with period $2\pi/\omega$ is obtained from (4.3):

$$W_d = \int_0^{\frac{2\pi}{\omega}} M(t)\dot{\alpha}(t)dt = \frac{\delta_s}{\pi} I\omega^3\alpha^2 \int_0^{\frac{2\pi}{\omega}} \cos^2(\omega t)\, dt = \delta_s I\omega^2\alpha^2 \tag{4.5}$$

A well-known textbook result.

4.2 Early wind tunnel test of the Tacoma Narrows cross section and analysis

Before embarking on the development of a model for one-degree-of-freedom flutter, it is instructive to review some of the aerodynamic characteristics of the Tacoma Narrows cross section as presented in the Carmody report [2], Figure 4.1. The damping vs wind speed diagram (left) was obtained from recordings of the oscillatory response of an elastically suspended section model, Figure 4.2. At low wind speeds the model was excited by hand in torsion and decay traces recorded from which the logarithmic damping decrement was estimated. At higher wind speeds torsion oscillations would self-start and grow to an equilibrium position once the model was released. The logarithmic decrement of the growth of the oscillations was referred to as "negative damping". From Figure 4.1 it is observed that the damping-mass parameter δ/μ changes from positive to negative at a non-dimensional wind speed $V/bn \approx 4$ at which "self-induced" oscillations starts.

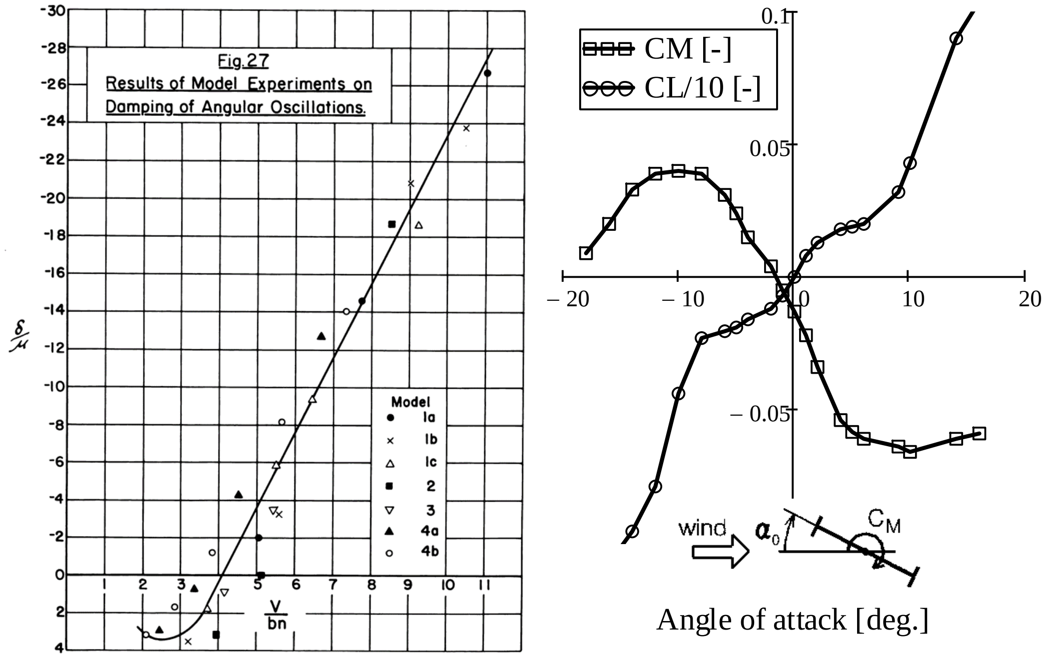

Figure 4.1 Aerodynamic damping to model mass ratio δ/μ vs non-dimensional wind speed V/bn (left) and moment and lift coefficients C_M, C_L vs angle of attack α_0 (right). Note that the lift coefficient is plotted as $C_L/10$ to fit the scale of C_M.Data extracted from the Carmody report [2].

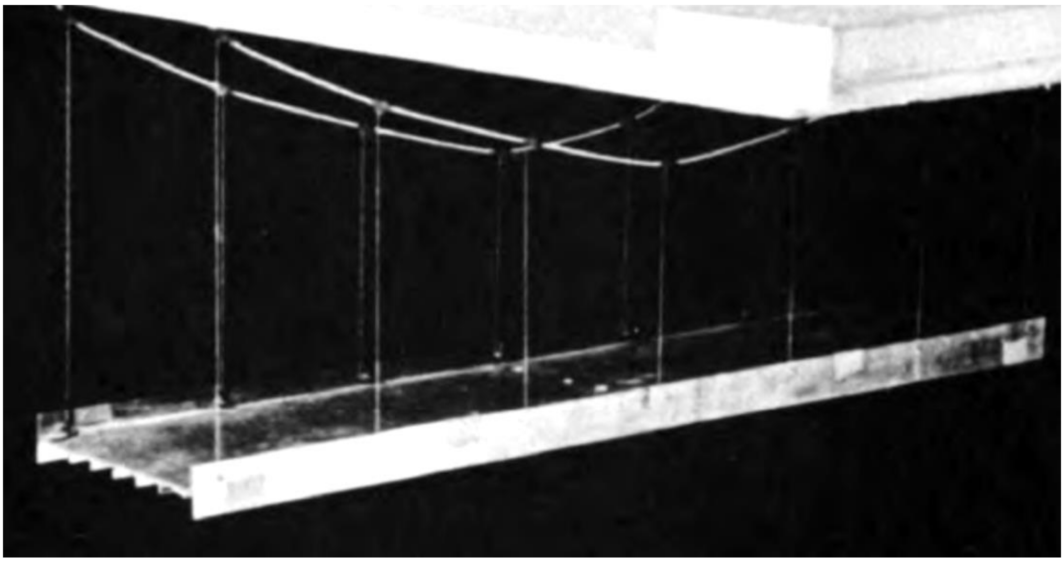

Figure 4.2 Elastically suspended 1:80 scale section model of the Tacoma Narrows Bridge in the GALCIT wind tunnel [2].

The steady state aerodynamic moment and lift coefficients of the original deck section are plotted in Figure 4.1 (right). It is noted that the slope of the C_M curve is negative $\partial C_M/\partial\alpha_0 \approx$ - 0.49 but that the lift slope is positive $\partial C_L/\partial\alpha_0 \approx$ 2.4.

A comment on the damping mass parameter δ/μ in Figure 4.1 (left) is appropriate. δ is the logarithmic decrement of the aerodynamic damping i.e. the total damping measured for model oscillations in the wind flow subtracted the mechanical damping of the model measured with no wind flow in the tunnel (hereafter referred to as δ_a). $\mu = \rho B^2/m$ is the mass ratio i.e. the density of air ρ multiplied by deck width B squared divided by model (or bridge) mass per unit length m. The Carmody report states μ = 0.0207 for the Tacoma Narrows Bridge. It is noted that δ/μ is identical in form to the Scruton number $Sc = 2\delta m/\rho B^2$ save a factor of 2.

Prediction of the critical wind speed for onset of one-degree-of-freedom flutter from experimental data such as Figure 4.1 (left) follows from balancing the aerodynamic and structural damping. Figure 4.3 shows the mean line of the aerodynamic damping-mass parameter as function of the non-dimensional wind speed U/fB as given in the Carmody report. The critical wind speed is obtained as the abscissa of the intersection of the δ_a/μ curve and a horizontal line at the ordinate δ_s/μ. From Figure 4.3 the non-dimensional wind speed for onset of one-degree-of-freedom flutter for the Tacoma Narrows cross section is identified as U/fB = 4.8. The equivalent full scale wind speed is then obtained as 4.8$\cdot B \cdot f$ = 4.8·11.9 m ·0.2 Hz = 11.5 m/s by inserting the deck width of 11.9 m and the torsion frequency 0.2 Hz (Table 4.1).

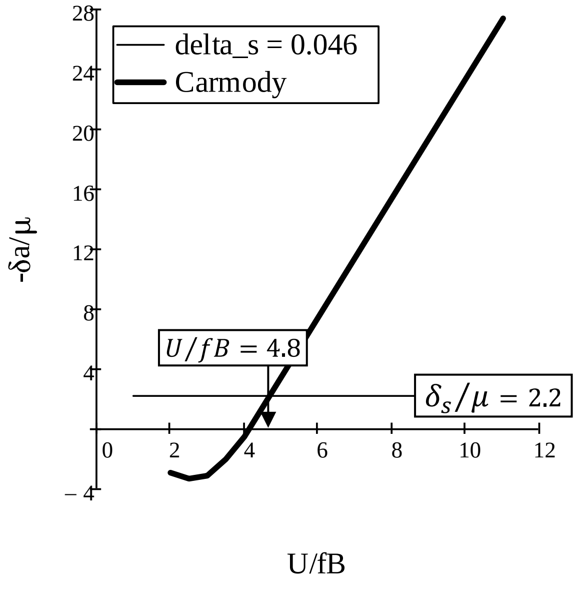

Figure 4.3 Identification of the critical wind speed for onset of one-degree-of-freedom flutter from wind tunnel data by balancing the aerodynamic and structural damping.

At this point, it is of interest to investigate to what degree the static aerodynamic data given in Figure 4.1 (right) can explain the "self-induced" oscillations observed in the dynamic wind tunnel test. We start out by considering a one-degree-of-freedom oscillator model subjected to an external forcing moment.

$$I\ddot{\alpha} + \frac{\delta_s}{\pi} I\omega_\alpha \dot{\alpha} + I\omega_\alpha^2 \alpha = ½\rho U^2 B^2 \frac{\partial C_M}{\partial \alpha_0} \theta(t) \tag{4.6}$$

Where $\omega_\alpha$is the eigenfrequency, U is the mean wind speed and $\theta(t)$ is the apparent angle of attack as function of time. Modelling of the external forcing moment adapts the classic quasi-steady approach, assuming that it is proportional to the moment slope multiplied by the apparent angular deflection $(\partial C_M/\partial \alpha_0)\theta$. From Figure 4.1 this (right) model is estimated to be valid for angles of attack in the interval $-5^0 < \theta < 5^0$.

The apparent angular deflection θ for a cross section in angular motion in a fluid flow is different from that of a stationary section or a section performing oscillations in a quiescent fluid as the fluid flow creates a pressure distribution which is asymmetrical with respect to the centre line of the section. From geometrical considerations (see section 5.1) it can easily be shown that:

$$\theta = \alpha + \frac{rB}{U}\dot{\alpha} \tag{4.7}$$

where r is the non-dimensional location of the centre of pressure away from the mid-chord position and can be found from steady state load measurements as the ratio of the moment slope to the lift slope.

$$r = \frac{\partial C_M}{\partial \alpha_0} \Big/ \frac{\partial C_L}{\partial \alpha_0} \tag{4.8}$$

For a classical flat plate airfoil having $\partial C_M/\partial \alpha_0 = \pi/2$ and $\partial C_L/\partial \alpha_0 = 2\pi$, r is 0.25. For the Tacoma Narrows deck section r = -0.49 / 2.4 = -0.204.

Introducing (4.7) in (4.6) and assuming that the response is harmonic in time (4.6) can be rewritten as:

$$\begin{aligned} I(\omega_\alpha^2 - \omega^2)\alpha \sin(\omega t) + \frac{\delta_s}{\pi} I\omega_\alpha \omega\alpha \cos(\omega t) \\ = ½\rho U^2 B^2 \frac{\partial C_M}{\partial \alpha_0} \alpha \left(\sin(\omega t) + \frac{rB\omega}{U}\cos(\omega t) \right) \end{aligned} \tag{4.9}$$

The wind tunnel tests proved that oscillation frequency with and without wind was identical and equal to the eigenfrequency $\omega = \omega_\alpha$ (aerodynamic stiffness is negligible) thus the stiffness and inertia term in (4.9) cancels leaving the structural damping and aerodynamic forcing to balance. The work dissipated by structural damping was obtained in (4.5). The work performed by the aerodynamic moment is obtained from (4.3) as:

$$
\begin{aligned}
W_a &= ½\rho U^2 B^2 \frac{\partial C_M}{\partial \alpha_0} \omega \alpha^2 \int_0^{\frac{2\pi}{\omega}} \left(\sin(\omega t) + \frac{rB\omega}{U} \cos(\omega t) \right) \cos(\omega t) dt \\
&= ½\rho U^2 B^2 \frac{\partial C_M}{\partial \alpha_0} \omega \alpha^2 \int_0^{\frac{2\pi}{\omega}} \frac{rB\omega}{U} \cos^2(\omega t)\, dt \\
&= ½\pi r \rho U^2 B^2 \frac{\partial C_M}{\partial \alpha_0} \left(\frac{B\omega}{U} \right)
\end{aligned}
\tag{4.10}
$$

By equating the work dissipated by viscous damping over one cycle to the work performed by the aerodynamic moment the resulting aerodynamic damping is obtained as follows

$$
\delta_a \left(\frac{U}{\omega B} \right) = \frac{\pi}{2} \left(\frac{\rho B^4}{I} \right) \left(\frac{U}{\omega B} \right) r \frac{\partial C_M}{\partial \alpha_0}
\tag{4.11}
$$

Where $U/fB = 2\pi\, U/\omega B$ is the non-dimensional wind speed. A graphical presentation of (4.11) compared to the aerodynamic damping curve of the Carmody report applying structural and aerodynamic data relevant to the Tacoma Narrows Bridge, Table 4.1. Equation (4.11) illustrates that purely quasi steady considerations produces aerodynamic damping that remains positive at ever increasing wind speeds, thus one-degree-of-freedom flutter instability will not occur if other aerodynamic effects are not present.

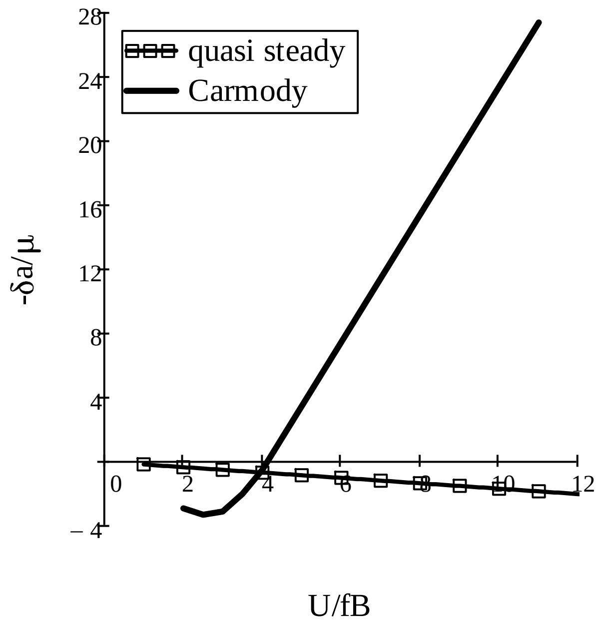

Figure 4.4 Aerodynamic damping obtained from quasi-steady considerations compared to aerodynamic damping reported for the GALCIT measurements of the Tacoma Narrows cross section. It is noted that the quasi steady aerodynamic damping remains positive for ever increasing wind speeds whereas the experimental data displays a shift from positive to negative values at U/fB = 4.

m [kg/m]	I [kgm^2/m]	f [Hz]	B [m]	$(\partial C_M/\partial\alpha_0)$	$(\partial C_L/\partial\alpha_0)$	δ_s [-]
8483	177730	0.2	11.9	-0.49	2.4	0.046

Table 4.1 Structural and aerodynamic properties of the Tacoma Narrows Bridge relevant to evaluation of (11). $\delta_s$is the still air structural damping estimated from the GALCIT wind tunnel tests [2].

4.3 Flow simulations for a generic Tacoma Narrows Bridge section

Flow simulations for a generic representation of the Tacoma Narrows cross section was carried out in order to obtain a deeper insight into the fluid structure interaction than can be obtained from the Carmody report.

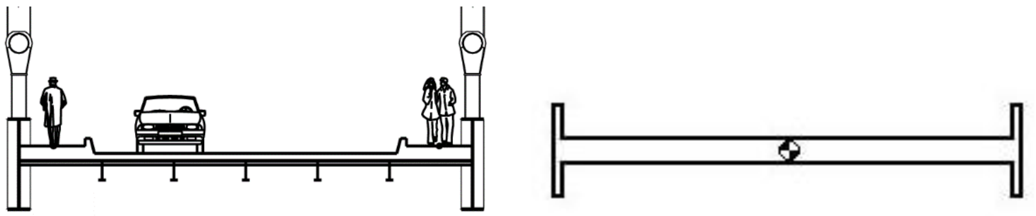

Figure 4.5 Tacoma Narrows Bridge cross section (left) and two-dimensional DVMFLOW section model (right) composed of 200 surface panels.

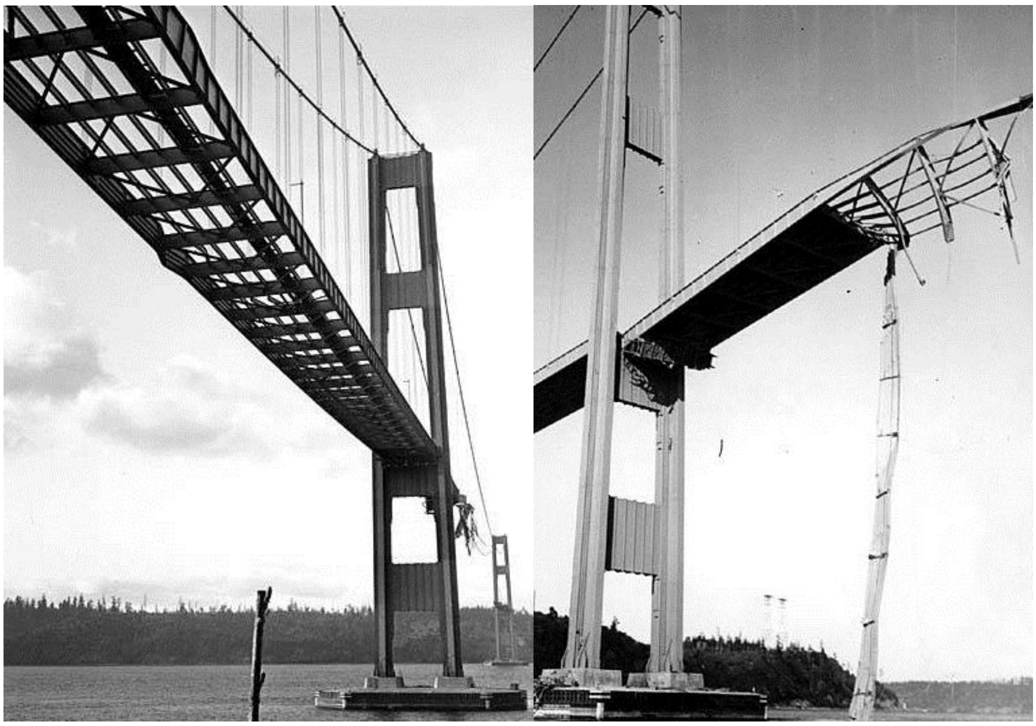

Figure 4.6 Pictures of the wrecked Tacoma Narrows Bridge displaying the layout of the cross girders, longitudinal stringers and K-bracing supporting the concrete roadway slab.

The cross section of the bridge girder is shown in Figure 4.5 (left) and the surface panel model applied in the discrete vortex flow simulations is shown to the right.

The panel model reproduces the generic external H-shaped form of the cross section but neglects the finer details of the roadway geometry and the longitudinal stringers. The three-dimensional arrangement of the cross beams and K-bracings supporting the roadway slab are shown in the pictures reproduced in Figure 4.6 and are obviously neglected in the discrete vortex model. A detailed description of the discrete vortex code DVMFLOW applied in the following discussion is presented by Larsen and Walther [9].

The steady state external moment an lift acting on the cross section was obtained by running the panel model at 23 angles of attack α_0 (incidence to the horizontal inflow) in the range -40^0 < α_0 < 40^0 Figure 4.7.

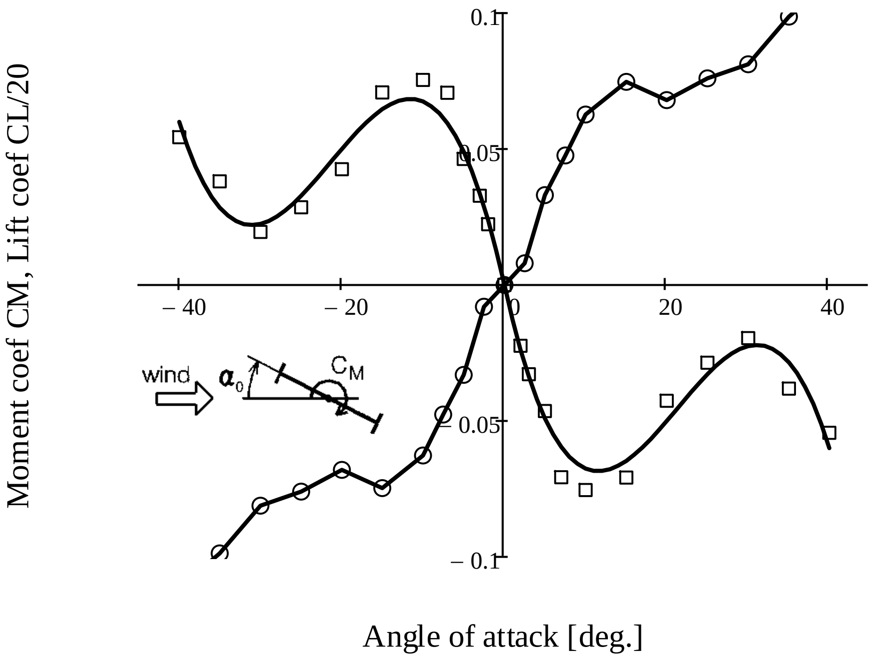

Figure 4.7 Moment coefficient C_M (□) and lift coefficient C_L/20 (○) for the generic H-shaped cross section obtained from discrete vortex simulations. Polynomial fit to C_M (▬).

The discrete points of the C_M curve obtained from the flow simulations are fitted by third order polynomials yielding the following expression for the moment coefficient as function of angle of attack.

$$C_M(\alpha_0) = \begin{cases} -0.774\alpha_0 - 2.627\alpha_0^2 - 2.352\alpha_0^3, & \alpha_0 < 0 \\ -0.774\alpha_0 + 2.627\alpha_0^2 - 2.352\alpha_0^3, & \alpha_0 \geq 0 \end{cases} \qquad (4.12)$$

The moment slope $\partial C_M/\partial\alpha_0$ = -0.774 obtained from the flow simulations quoted above is very close to the value $\partial C_M/\partial\alpha_0$= -0.77 obtained from high Reynolds number experiments conducted in a compressed air wind tunnel, Schewe [10].

The smaller moment slope $\partial C_M/\partial \alpha_0 \approx$ - 0.49 estimated from the GALCIT tests is speculated to be due to three-dimensional flow around the ends of the section model shown in Figure 4.2. An observation first made by Farquharson [3] part I, which lead to introduction of end plates on the section models used in the later tests of the Tacoma Narrows wind tunnel investigations.

In order to gain insight into possible phase shifts between structural motion and aerodynamic forces a simulation was run in which the section angle of attack was changed instantaneously form 0 deg. (horizontally aligned with the direction of flow) to 10 deg. nose up at the non-dimensional time $tU/B = 10.0$, Figure 4.8. From the simulation it is noted that a large coherent clock-wise rotating vortex structure is created once the cross section changes angle of attack. As time progresses the vortex structure travels downwind from a position close to the upwind vertical girder where it is created towards the cross section centroid. At $tU/B = 11.0$ the vortex structure is at a position approximately above the upwind quarter chord point. At $tU/B = 12.0$ the vortex has travelled to a position right above the centroid and at $tU/B = 13.0$ to a position roughly over the downwind quarter chord point.

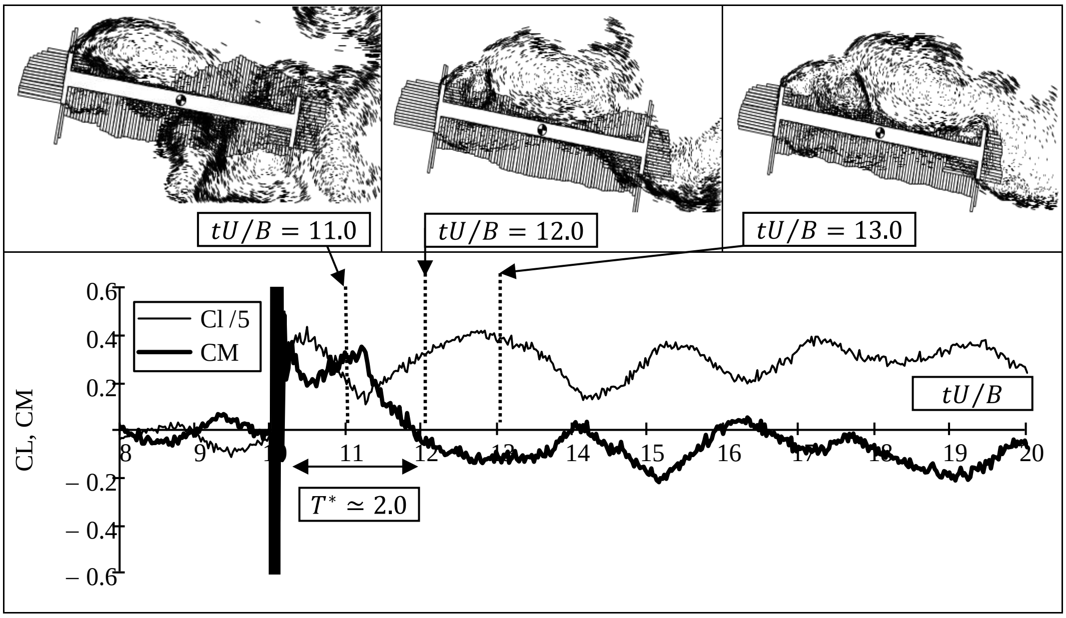

Figure 4.8 Vortex formation and development of lift and moment coefficients following a sudden change of angle of attack of the generic Tacoma Narrows cross section and the definition of the vortex drift time $T = T^{*}\cdot B/U$. The moment coefficient is multiplied by a factor 5 to fit the same scale as the lift coefficient.

From the development of lift (C_L) and moment coefficient (C_M) about the cross section centroid the following observations are made: At $tU/B < 10.0$ before the sudden change of angle of attack the force and moment coefficients oscillates about a zero mean value. At $tU/B = 10.0$ following the abrupt change in angle of attack and short duration transients, the lift coefficient changes to oscillate about a positive mean value of $C_L \simeq 1.5$. The moment coefficient on the other hand starts out at $tU/B = 10.0$ being positive $C_M \simeq 0.4$ (nose-up) but decreases with increasing time. At $tU/B = 12.0$ $C_M \simeq 0.0$ which coincides with the large travelling vortex structure being located above the cross section centre line. At $tU/B > 12.0$ when the travelling vortex has moved to a position downwind of the centre the moment coefficient becomes negative. At $tU/B = 14.0$ the travelling vortex structure passes the downwind vertical girder and the moment coefficient shortly reverts to $C_M \simeq 0.0$. At $tU/B > 14.0$ the moment coefficient oscillates about a negative mean value while the lift coefficient remains positive. Figure 4.8 demonstrates that the creation and drift of the large coherent vortex structure introduces a phase lag between the angular displacement and the steady state force. In case there had been no phase delay, the mean of the moment coefficient would have become negative and proportional to the angular displacement immediately upon the step change of the inflow angle in agreement with Figure 4.7.

Of particular importance to the physical model for the resulting instability to be presented in section 4.5 is the drift-time T^* i.e. the non-dimensional time it takes the vortex to travel from the position where it is formed at the upwind girder to the position above the cross section centre. From Figure 4.8 the drift time is estimated as $T^* \simeq 2$ in good agreement with physical observations made by Kubo et. al. that coherent vortex structures travels along the surface of a bluff section at a speed of about 25% of the speed of the free flow, [12]. The formation and drift of coherent vortices shown in Figure 4.8 allows formulation of the following physical model for the fluid-structure interaction:

1) Each time the cross section changes angle of attack away from main direction of the flow a vortex will be shed just behind the upwind vertical girder. When the cross section changes angle of attack to a nose-up position the vortex rotates clock-wise and is shed at the upper horizontal part of the cross section. When the cross section changes angle of attack to a nose-down position the vortex rotates counter clock-wise and is shed at the lower horizontal part of the cross section.

2) Once created a vortex structure will travel along the upper or lower horizontal part of the cross section with a speed corresponding to roughly $1/4$ of the speed of the free flow.

A key assumption in the development of the flutter derivatives as presented by Scanlan [8] and shown in Figure 3.4, is that they are independent of the amplitude of motion of the deck cross section. In the present case of the generic shallow H-section Figure 4.5, the A_2^* aerodynamic derivative was obtained from DVMFLOW forced motion simulations for four different torsion amplitudes α = 5^0, 10^0, 20^0 and 45^0 and is shown in Figure 4.9. The result (adopting Scanlans original normalization by twice the dynamic head ρU^2) reveals that A_2^* assumes more or less the same values for α = 5^0 and 10^0 but decreases with increasing amplitude.

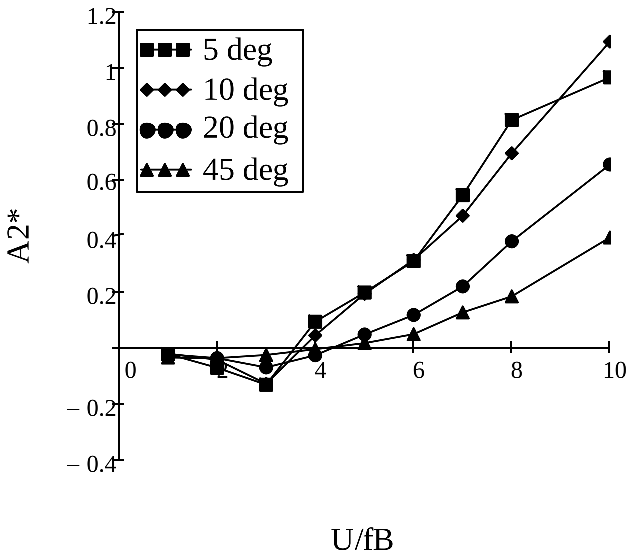

Figure 4.9 DVMFLOW simulations of the A_2^* aerodynamic derivative for torsion amplitudes α = 5^0, 10^0, 20^0 and 45^0.

If A_2^* obtained for α = 20^0 and 45^0 are multiplied by α/α_{ref} where α_{ref} = 10^0, the A_2^* derivatives will more or less collapse on one curve Figure 4.10 suggesting a $1/\alpha$ dependence of the A_2^* aerodynamic derivative for α > 10^0.

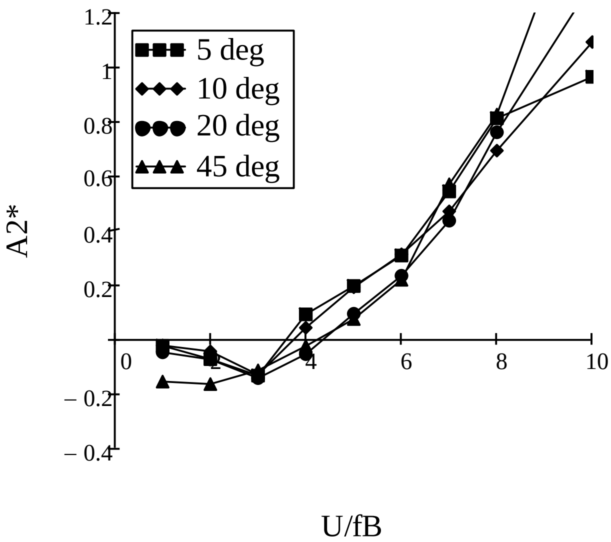

Figure 4.10 The simulated A_2^* curves shown above collapsed through multiplication with the ratio of actual amplitude α to $\alpha_{ref} = 10^0$.

4.4 Year 2000 travelling point vortex model for one-degree-of-freedom-flutter

At the 60 year anniversary of the Tacoma incident the present author utilized a rather busy sketch, Figure 4.11, to develop a physical model for the threshold wind speed of one-degree-of-freedom flutter which lead to the collapse of bridge [13]. This model has generally been accepted as providing a satisfactory physical explanation for aerodynamic excitation leading to the collapse [14], [15]. The argument involved in the development of the model was based on the vortex dynamics observed in Figure 4.8 and on the power supplied to the cross section by the fluid over a half period of oscillation.

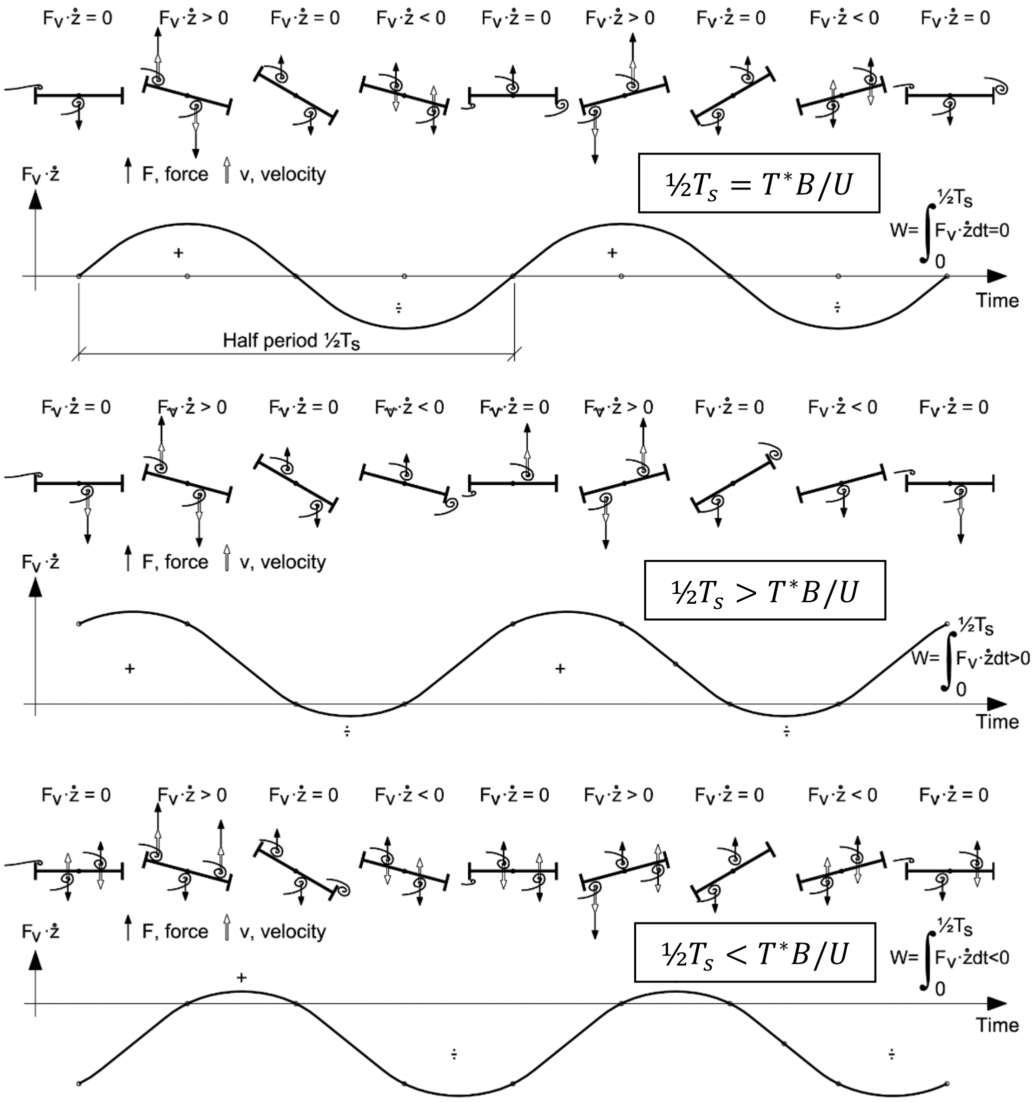

Figure 4.11 Instability model based on work supplied to the cross section by the fluid (travelling point vortices). From [13].

When the vertical vortex force F_v is in the same direction as the local vertical velocity $\dot{z}$ of the cross section just below the vortex the fluid supplies a power input to the cross section. When the vortex force and the structural velocity are opposite power is extracted from the cross section. Summing the power exchange over half a period of structural (torsion) oscillation $½T_s$ it is illustrated that the work is positive if half the oscillation period is longer than the drift time $½T_s > T^*B/U$, the work is negative if half the oscillation period is shorter the drift time $½T_s < T^*B/U$ and exactly balances if half the oscillation period becomes equal to the drift time $½T_s = T^*B/U$. Taking $T^* = 2$ the incipient or critical wind speed for the associated instability is obtained as:

$$½T_s \geq T \Rightarrow \; U_c \geq 4f_\alpha B \tag{4.13}$$

Where $f_\alpha = 1/T_s$ is the structural torsion frequency and B is the over all section width.

4.5 Point vortex model for the Tacoma one-degree-of-freedom flutter

The above argument can be recast in a compact mathematical form by expressing the power supplied by the vortex to the deck section as the scalar product of the vortex force which is taken as constant in time and the vertical velocity of the deck at the location of the vortex. Alternatively the power may be expressed as the scalar product of the aerodynamic moment and angular velocity of the deck about the elastic axis.

In mathematical terms the vertical force F_v acting on the deck due to the vortex and the angular displacement and velocity $\alpha, \dot{\alpha}$ of the bridge deck are expressed as follows:

$$F_v = ½\rho U^2 B C_L, \qquad \alpha = \alpha\sin(\omega t), \qquad \dot{\alpha} = \alpha\omega\cos(\omega t) \tag{4.14}$$

Where α is the torsion amplitude (in radians) and $\omega = 2\pi f$ the torsion radian frequency.

The torsion velocity of the deck at the location of the vortex then becomes:

$$\dot{\alpha} = \alpha\omega\cos(\omega t)\frac{B}{2}\left(1 - \frac{t}{T}\right) \tag{4.15}$$

Alternatively the aerodynamic moment supplied by the travelling vortex $M_v(t)$ may be taken as a function of time:

$$M_v(t) = F_v\frac{B}{2}\left(1 - \frac{t}{T}\right) = \frac{\rho B^2 U^2 C_{M0}}{4}\left(1 - \frac{t}{T}\right) \tag{4.16}$$

The work performed by the travelling leading edge vortex is obtained combining (4.3) and (4.16):

$$W_v = \int_0^{2T} M(t)\dot{\alpha}(t)dt = \frac{\rho B^2 U^2 C_{M0}}{4}\alpha\int_0^{2T}\left(1 - \frac{t}{T}\right)\alpha\omega\cos(\omega t)\,dt \tag{4.17}$$

Where the upper limit of the integral $t = 2T$ is the time it takes for the point vortex to travel from the leading edge to the trailing edge of the deck section.

Evaluation of the integral in (16) yields (see Appendix A):

$$W_v = \frac{\rho B^2 U^2 C_{M0}}{4} \alpha \left(\frac{1}{\omega T} (1 - \cos(2\omega T)) - \sin(2\omega T) \right) \tag{4.18}$$

Introduction of the non-dimensional vortex drift time $T = T^* B/U = 2B/U$ allows the work performed by the travelling vortex to be expressed in terms of the non-dimensional wind speed $U/\omega B$:

$$W_v = \frac{\rho B^2 U^2 C_{M0}}{4} \alpha \left(\frac{U}{2\omega B} \left(1 - \cos\left(\frac{4\omega B}{U}\right)\right) - \sin\left(\frac{4\omega B}{U}\right) \right) \tag{4.19}$$

In order to recast (4.19) in the form of aerodynamic damping, W_v is set equal to the work W_d dissipated by viscous damping during the time interval $0 \leq t < 2T$:

$$W_d = \frac{\delta_a}{\pi} I\omega^3 \alpha^2 \int_0^{2T} \cos^2(\omega t)\, dt = \frac{\delta_a}{2\pi} I\omega^2 \alpha^2 \left(2\omega T + \frac{\sin(4\omega T)}{2} \right) \tag{4.20}$$

or when introducing the vortex drift time $T = T^* B/U = 2B/U$:

$$W_d = \frac{\delta_a}{2\pi} I\omega^2 \alpha^2 \left(\frac{4\omega B}{U} + \frac{1}{2} \sin\left(\frac{8\omega B}{U}\right) \right) \tag{4.21}$$

Finally putting $W_d = W_v$ yields an expression for the aerodynamic damping δ_{ap} associated with the travelling point vortex as function of non-dimensional wind speed:

$$\delta_{ap}\left(\frac{U}{\omega B}\right) = \frac{\pi}{2} \left(\frac{\rho B^4}{I} \right) \left(\frac{U}{\omega B} \right)^2 \frac{C_{M0}}{\alpha} \frac{\left(\frac{U}{2\omega B} \left(1 - \cos\left(\frac{4\omega B}{U}\right)\right) - \sin\left(\frac{4\omega B}{U}\right) \right)}{\left(\frac{4\omega B}{U} + \frac{1}{2} \sin\left(\frac{8\omega B}{U}\right) \right)} \tag{4.22}$$

From (4.22) it is noted that the aerodynamic damping associated with the travelling point vortex displays a $1/\alpha$ dependence as indicated by the A_2^* DVMFLOW simulations discussed in section 4.3.

The aerodynamic damping divided by mass ratio δ_{ap}/μ as function of non-dimensional wind speed $U/fB = 2\pi U/\omega B$ obtained from (4.22) is plotted in Figure 4.12 with the mean curve of the damping measurements given in the Carmody report Figure 4.1 (left). It is assumed that $C_{M0} = 0.4$ in accordance with Figure 4.18

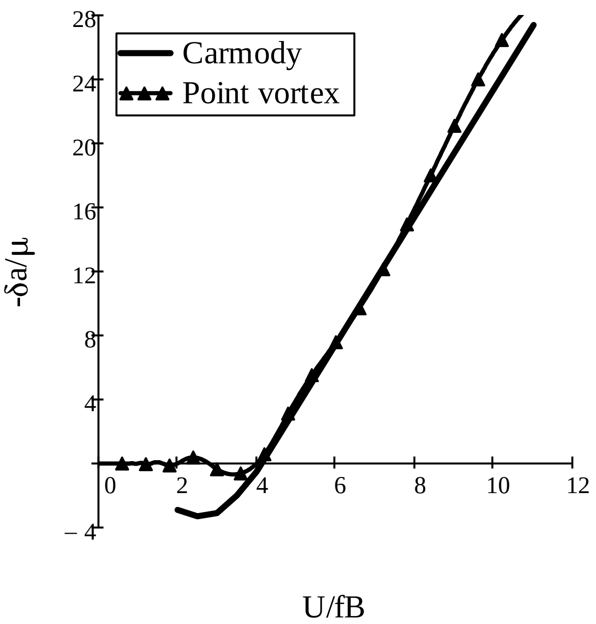

Figure 4.12 Aerodynamic damping / mass ratio as function of non-dimensional wind speed obtained from (4.22) and compared to the mean curve published in Figure 27 of the Carmody report. $\alpha = 10^0$, $C_{M0} = 0.4$, $\mu = 0.0207$.

4.6 Critique of the travelling point vortex model

Green and Unruh [16] reviewed the travelling point vortex model proposed by the author (section 4.4) above and agreed that it predicts the onset wind speed of the instability. From Green and Unruhs mathematical representation of work done by the travelling vortex, they found that the theory predicted the expected onset of the instability at a non-dimensional wind speed of about 4 but that it failed at higher wind speeds. First, they observed that the behaviour of their predicted damping curve displayed a peak value at a full-scale wind speed of approximately 22 m/s and decreasing at higher wind speeds, Figure 4.13 (left), was never observed in wind tunnel tests. Secondly, Green and Unruh argued that the physics of the flow at high wind speeds is different to that of a travelling point vortex. Rather, the vortex formed when the leading edge starts to raise stays attached to the windward vertical girder and grows to cover the whole deck during the first quarter of the oscillation period. When the windward girder starts to travel downward again, this large vortex will detach and is swept across the deck past the downwind vertical girder. The action of the distributed vortex may thus be different to that of a travelling point vortex.

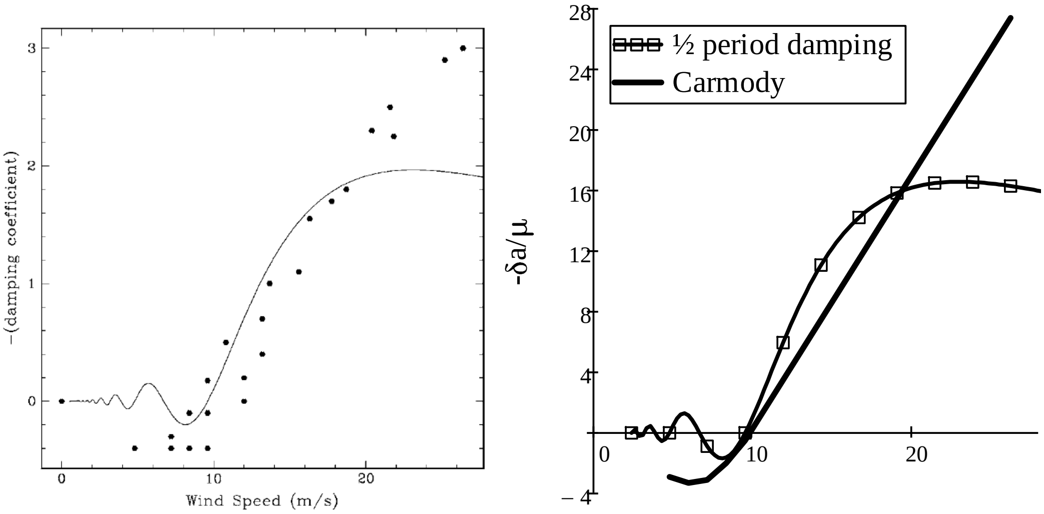

Figure 4.13 Predicted normalized aerodynamic damping as function of full scale wind speed. Left: Adapted from Green and Unruh [16]. Right: Authors prediction (21) assuming that the work supplied by the travelling vortex is balanced by damping dissipated over half an oscillation cycle. $\alpha = 5^0$, $C_{M0} = 0.4$.

In an attempt to clarify the alleged failure of the point vortex model at higher wind speeds, the author experimented with different mathematical models. One attempt involved balancing the work performed by the travelling point vortex by work dissipated by viscous damping over half an oscillation cycle of the deck. The result given in (4.23) taking T^* = 2 is displayed in Figure 4.13 right. It is noted that the damping curve in Figure 4.13 left and right are identical (save a difference on the amplitude scale) indicating that Green and Unruh based their conclusion on an incorrect balance of work.

$$\delta_{ap}\left(\frac{U}{\omega B}\right) = \left(\frac{\rho B^4}{I}\right)\left(\frac{U}{\omega B}\right)^2 \frac{C_{M0}}{2\alpha}\left(\frac{U}{2\omega B}\left(1 - \cos\left(\frac{4\omega B}{U}\right)\right) - \sin\left(\frac{4\omega B}{U}\right)\right) \quad (4.23)$$

Green and Unruh's mathematical model for the growing/travelling vortex at high wind speeds is not quite clear from their physical explanation neither from their resulting mathematical expression for work given in [16].

4.7 Extension of the travelling point vortex model to high wind speeds

The comments by Green and Unruh inspired the present author to extend the travelling point vortex model to include quasi steady effects that might become important once half the oscillation period becomes longer than the time it takes for the vortex to travel from the leading edge to the trailing edge of the deck section. When the travelling vortex has swept past the trailing edge at $T^* = 4$ the cross section is still subject to an aerodynamic moment having a non-zero mean, By combining the travelling vortex and the quasi-steady moment the physical model sketched in Figure 4.14 is arrived at. This model is expected to be applicable at high wind speeds when a vortex sweeps faster across the deck than half the period of the torsion motion, i.e. at wind speeds $U \geq 8Bf$.

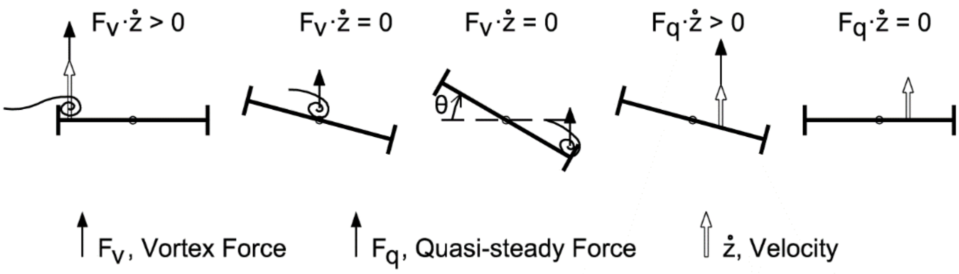

Figure 4.14 High wind speed model combining travelling vortex and quasi-stationary aerodynamic forces on a shallow H section.

The high wind speed behavior is summarized as follows: At the start of the oscillation period when the windward edge rises a vortex is formed which will travel across the deck precisely as in the low wind speed case. However, the vortex will have swept past the downwind edge before the deck has completed half a period of the torsion oscillation. When the windward girder reaches the highest point of the oscillation the vortex covers the whole deck section. Once the vortex is clear of the deck section its presence is no longer felt by the deck and the quasi-steady wind forces govern the aerodynamic action on the deck. As the quasi-stationary moment is negative (opposite the angle of attack) the action is to force the cross section to lower angles of attack. The work exerted by the vortex and the quasi-steady aerodynamic forces in combination is now found simply as the sum of the contributions from the drifting point vortex and the quasi-steady moment:

$$W_v + W_q = \int_0^{2T} M_v \cdot \dot{\alpha} dt + \int_{2T}^{½T_s} M_q \cdot \dot{\alpha} dt \tag{4.24}$$

The evaluation of the first integral proceeds exactly as for (4.17) reference is made to appendix A. For evaluation of the second integral the quasi-steady moment is expressed as $M_q = ½\rho U^2 B^2 C_M(\alpha)$ where $C_M(\alpha)$ is the moment coefficient as a function of the angle of attack. The work W_q exerted by the quasi-steady aerodynamic forces over the period $2T \leq t \leq ½T_s = 2T \leq t \leq \pi/\omega$ is obtained as:

$$W_q = ½\rho B^2 U^2 \int_{2T}^{\frac{\pi}{\omega}} C_M(\alpha)\alpha\omega \cos(\omega t)\, dt \tag{4.25}$$

Assuming that the angle of attack dependence of the moment coefficient can be expressed in a linear fashion similar to (4.6), (4.25) is rewritten as:

$$W_q = ½\rho B^2 U^2 \int_{2T}^{\frac{\pi}{\omega}} \left(\alpha \left(\sin(\omega t) + \frac{rB\omega}{U} \cos(\omega t)\right)\right) \alpha\omega \cos(\omega t)\, dt \tag{4.26}$$

Upon which the integral is evaluated to yield:

$$W_q = -\frac{1}{4}\rho B^2 U^2 \alpha^2 \left(\sin^2(2\omega T) + \frac{rB\omega}{U}\left(\pi - 2\omega T - \frac{\sin(4\omega T)}{2} \right) \right) \tag{4.27}$$

The work W_d dissipated by viscous damping during the time interval $2T \leq t \leq \pi/\omega$ is obtained as:

$$W_d = \frac{\delta_a}{\pi} I \omega^3 \alpha^2 \int_{2T}^{\frac{\pi}{\omega}} \cos^2(\omega t)\, dt = \frac{\delta_a}{2\pi} I \omega^2 \alpha^2 \left(\pi - 2\omega T - \frac{\sin(4\omega T)}{2} \right) \tag{4.28}$$

Finally, setting $W_d = W_q$ and substituting $T = T^* B/U = 2B/U$ yields an expression for the aerodynamic damping δ_{aq} supplied by the quasi-steady aerodynamic forces as function of non-dimensional wind speed:

$$\delta_{aq}\left(\frac{U}{\omega B}\right) = \frac{-\pi}{2}\left(\frac{\rho B^4}{I}\right)\left(\frac{U}{\omega B}\right)^2 \frac{\sin^2\left(\frac{4\omega B}{U}\right) + \frac{rB\omega}{U}\left(\pi - \frac{4\omega B}{U} - \frac{\sin\left(\frac{8\omega B}{U}\right)}{2} \right)}{\left(\pi - \left(\frac{4\omega B}{U}\right) - \frac{\sin\left(\frac{8\omega B}{U}\right)}{2} \right)} \tag{4.29}$$

Evaluation of (4.29) is shown in Figure 4.15. It is noted that the effect of quasi-steady aerodynamics is to produce positive aerodynamic damping at non-dimensional wind speeds $U/fB < 8$. At higher wind speeds the quasi-steady aerodynamics becomes negative adding to the effect of the travelling vortex. The combined effect of the quasi-steady aerodynamics and the travelling vortex on the damping is obtained by adding δ_{ap} and δ_{aq} given by (4.22) and (4.29). The result is also shown in Figure 4.15 compared to the travelling vortex model alone and the mean damping given in the Carmody report. The comparison demonstrates that the quasi-steady aerodynamics are not particularly important and probably within the experimental uncertainty indicated by the measurement points shown in the original plot from the Carmody report.

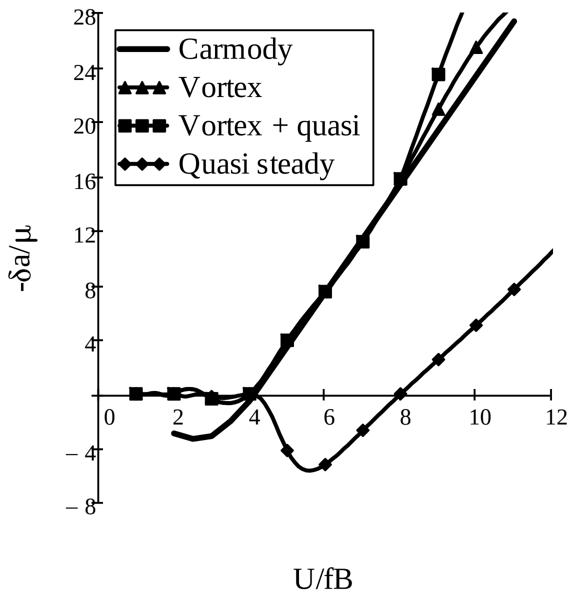

Figure 4.15 Aerodynamic damping obtained from the vortex term (▲) (4.22), from the quasi-steady term (♦) (4.29) and the combined effect $\delta_{av} + \delta_{aq}$ (■) compared to the mean aerodynamic damping curve of the Carmody report.

4.8 Expanding vortex model

The point vortex model discussed in section 4.5 may be criticized on two accounts: 1) Realistic T and C_{M0} must be obtained from other sources for the model to work. 2) The concept of a travelling point vortex does not fit actual observations of the travelling vortex. Flow simulations and experiments show that the vortex formed at the leading edge will at first grow in size until the centre reaches mid chord. Then the vortex will break away from the leading edge and travel to the ¾ chord point where it starts to be lifted off the cross section by recirculating flow filling in over the downwind vertical girder, Figure 4.8. To model this situation a continuous supply of circulation in time at the upwind girder is needed.

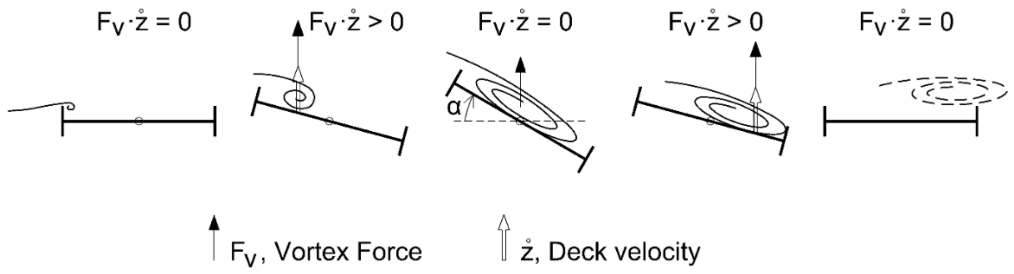

Figure 4.16 Model of expanding vortex being created at the upwind vertical girder and travelling across the deck.

In order to set up a model for the speed along the bridge deck of the center of an expanding vortex it is assumed that the upwind corner of the vertical girder above the deck is the primary source of circulation. A first step is to estimate the circulation Γ_0 of this starting vortex once it is fully developed and assumed to have a diameter roughly equal to the vertical height h of the upwind girder. The condition that the wind does not flow through the upwind girder is met in accordance with classical potential flow theory by introducing a mirror vortex of equal but negative circulation below the deck, Figure 4.17 (left).

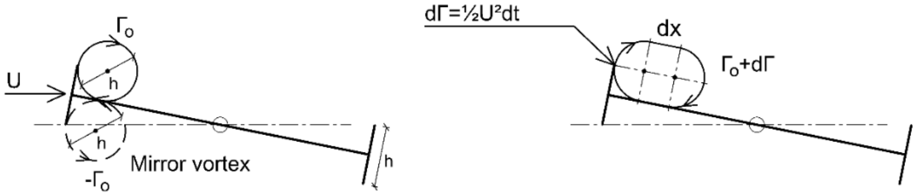

Figure 4.17 Determination of the circulation strength Γ_0 of the leading edge vortex (left). Model for the expanding leading edge vortex (right).

The sum of the tangential induced velocities of this vortex pair must then match the oncoming wind speed U, thus:

$$\Gamma_0 = \frac{\pi}{2} hU \tag{4.30}$$

By virtue of the vorticity equation the vorticity (circulation divided by area: Γ/A) in a quiescent inviscid region is constant. The wake region formed behind the upwind girder and above the deck when the section twists away from horizontal is assumed to fulfil this condition, thus:

$$\frac{\Gamma_0 + d\Gamma}{\frac{\pi}{4}h^2 + hdx} = \frac{\Gamma_0}{\frac{\pi}{4}h^2} \tag{4.31}$$

Solving (4.31) for $d\Gamma$ and inserting in (4.30) yields:

$$d\Gamma = 2Udx \tag{4.32}$$

The time rate of production of circulation at a corner of a bluff body is introduced as proposed by Sapkaya [17]:

$$d\Gamma \approx ½U^2dt \tag{4.33}$$

which when inserted in (4.33) yields the following estimate of the growth rate of the vortex front:

$$\frac{dx}{dt} \approx \frac{U}{4} \tag{4.34}$$

Hence, the apparent travelling speed U_v of the vortex is estimated as:

$$U_v = \frac{dx}{dt} \approx \frac{U}{4} \tag{4.35}$$

With the source of circulation fixed at the upper edge of the vertical windward girder the time rate of circulation shed over the deck is approximated by the time integral of Sapkaya's source equation:

$$\Gamma = ½U^2 t \tag{4.36}$$

The vortex force assuming to be acting on the deck section at the centre of the vortex and the aerodynamic moment about the half chord point (centre of rotation) then becomes:

$$\begin{aligned} F_v(t) &= \rho U \Gamma = ½\rho U^3 t \\ M(t) &= F_v(t)\frac{B}{2}\left(1-\frac{t}{T}\right) = ½\rho U^3 \frac{B}{2}\left(1-\frac{t}{T}\right)t \end{aligned} \tag{4.37}$$

Yielding a time dependent moment coefficient:

$$C_M(t) = \frac{1}{2}\left(1-\frac{t}{T}\right)t\frac{U}{B} \tag{4.38}$$

C_M has maximum $C_{Mmax} = 1/4$ at $t = T/2$ as illustrated in Figure 4.18.

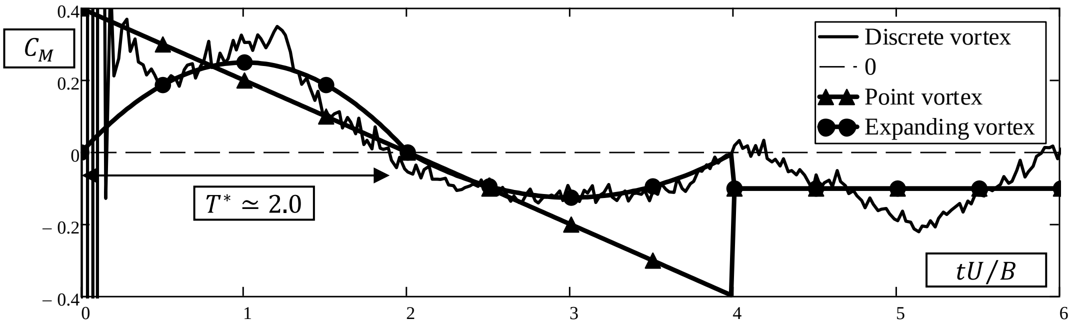

Figure 4.18 Comparison of $C_M(t)$ functions adopted for the travelling point vortex and expanding vortex model superimposed on the $C_M(t)$ signal obtained from DVMFLOW simulations also shown in Figure 4.8.

The $C_M(t)$ function given in (4.38) can only be expected to be valid in the time interval $0 < t < T$ where the vortex sits close to the horizontal portion of the deck surface. For $T < t < 2T$ when the vortex has drifted past the section mid chord point, it tends to be lifted off the section by recirculating flow filling in from the wake and thus loosing strength. As a consequence the moment coefficient at $t = 3T/2$ is half the value and negative $C_{Mmin}(3T/2) = -½C_{Mmax}(T/2)$.

The work exerted on the section by the expanding vortex follows the same procedure as for (4.17):

$$W_v = \int_0^{2\cdot T} M(t)\dot{\alpha}(t)dt$$
$$= \frac{\rho B U^3 \alpha\omega}{4}\left[\int_0^T \left(1-\frac{t}{T}\right) t\cos(\omega t)\,dt - \frac{1}{2}\int_0^T \left(1-\frac{t+T}{T}\right)(t+T)\cos(\omega(t+T))\,dt\right] \tag{4.39}$$

After some tedious but straight forward mathematical manipulations the expressions for the aerodynamic damping of the expanding vortex becomes:

$$\delta_{ae}\left(\frac{U}{\omega B}\right) = \frac{\pi}{2\alpha}\left(\frac{\rho B^4}{I}\right)\left(\frac{U}{\omega B}\right)^3 \frac{\left(\frac{U}{2\omega B}\right)\sin\left(\frac{2\omega B}{U}\right)\left(3-2\cos\left(\frac{2\omega B}{U}\right)\right)+\frac{1}{2}\left(\cos\left(\frac{4\omega B}{U}\right)-\cos\left(\frac{2\omega B}{U}\right)\right)-1}{\left(\frac{4\omega B}{U}+\frac{1}{2}\sin\left(\frac{8\omega B}{U}\right)\right)} \tag{4.40}$$

Progressing from Eq. (4.39) to (4.40) it is assumed that $T = B/2U_v \approx 2B/U$ following Eq. (4.35).

The aerodynamic damping obtained from (4.40) divided by mass ratio δ_{ae}/μ as function of non-dimensional wind speed $U/fB = 2\pi U/\omega B$ is plotted in Figure 4.19 with the mean curve of the damping measurements given in the Carmody report Figure 4.1 (left). The damping/mass ratio δ_{ap}/μ obtained from the travelling point vortex model (4.22) is also included for comparison. It is noted that both models provide quite accurate fits to the experimental data for non-demensional wind speeds in the range $4 < U/fB < 8$. The expanding vortex model displays a better agreement than the point vortex model at $4 < U/fB$.

Equation (4.40) can be used as the basis for development of a handy formula for the critical wind speed for the onset of one-degree-of-freedom flutter. Taking the derivative of δ_{ae} with respect to the non-dimensional wind speed at $U/fB = 4$.

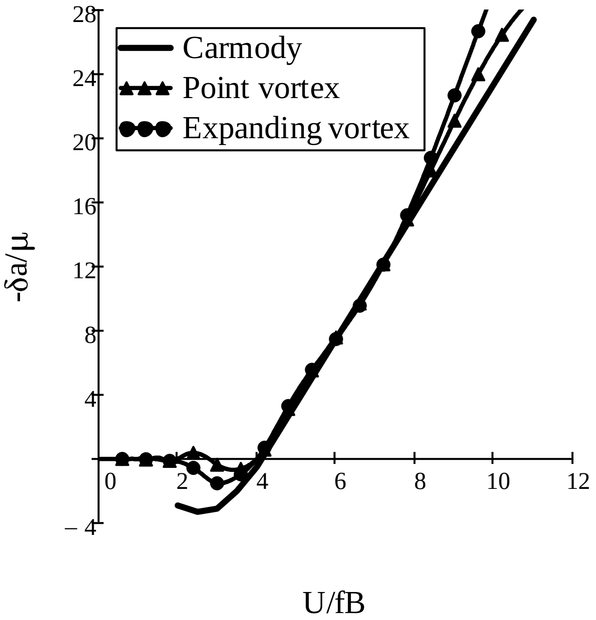

Figure 4.19 Comparison of travelling point vortex model (4.22) and expanding vortex model (4.40) to the mean curve published in Figure 27 of the Carmody report. $\alpha = 10^0$, $\mu = 0.0207$.

Solving for U/fB and balancing the result to the structural damping δ_s yields the following expression for the critical wind speed for onset of one-degree-of-freedom torsion flutter:

$$U_c = f_\alpha B\left(4 + \frac{\pi^3}{3}\frac{\alpha}{\alpha_{ref}}\left(\frac{I}{\rho B^4}\right)\delta_s\right) \tag{4.41}$$

For $\alpha \geq \alpha_{ref}$ taking $\alpha_{ref} = 10^0$ (= 0.175 rad).

Equation (4.41) is the one-degree-of-freedom equivalent of Selberg's formula which is applicable to two-degree-of-freedom flutter as will be discussed in section 5.8.

4.9 Water tunnel flow visualization test

The conclusions drawn relating to the excitation of torsion galloping of the shallow H-section rests on the formation and drift of the large coherent leading edge vortex as perceived from the numerical flow simulations, section 4.3. It was thus desirable to establish if the drifting leading edge is a true physical phenomenon or a function of the numerical simulation procedure. In order to investigate the formation and drift of the leading edge vortex a flow visualization experiment was carried out in the closed circuit water tunnel of the Fluid Dynamics Institute, ETH, Zürich, Switzerland, Figure 4.20, which has a rectangular cross section 0.1 m high and 0.3 m wide. Models are mounted on a 0.25 m diameter base-plate inserted in the ceiling of the measurement section approximately 0.3 m downstream of the inlet contraction. The water speed in the tunnel is freely adjustable in the range 0.05 m/s - 1.0 m/s. The water tunnel incorporates a number of flow visualization systems including multi-coloured dye and a pulsed 50 Volt DC voltage supply designed for hydrogen bubble generation. The hydrogen bubble flow visualization system was applied in the present tests.

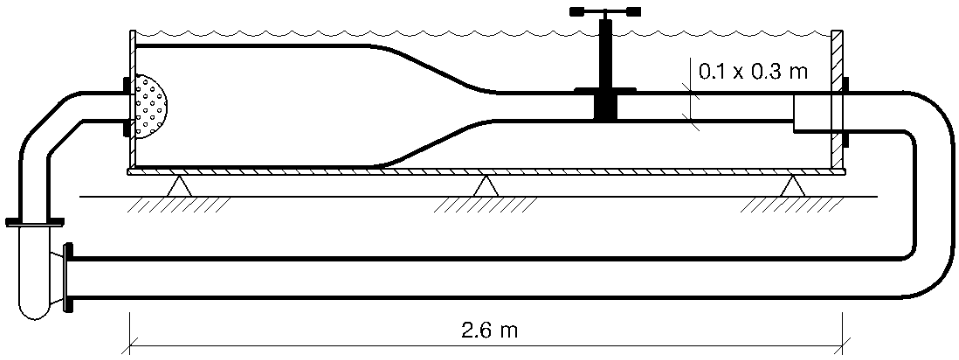

Figure 4.20 Closed circuit 0.1 m x 0.3 m water tunnel at ETH, Zürich, Switzerland.

The measurement set-up comprised prismatic Perspex models of constant cross section having a chord length B = 0.05 m and a span length of 0.1 m. The models were suspended vertically in the tunnel spanning the height of the measurement section. The upper end of the models was attached at mid-chord to a vertical shaft supported by two ball bearings, thus allowing the model to rotate about the spanwise mid-chord axis. Outside the tunnel, the shaft carried a crossbar / counterweight allowing adjustment of the mass moment of inertia of the shaft / model assembly. A helical spring connected to the vertical shaft and the ball-bearing support comprised the adjustable torsion spring element, Figure 4.21. The counterweight/crossbar assembly was adjusted to yield a non-dimensional mass moment of inertia $I/\rho B^4$ = 6.2627 / unit length and the torsion spring was adjusted to yield an eigenfrequency f_α = 0.31 Hz of the model assembly in torsion when submerged in water. This "slow" setting allowed video recordings using standard digital video equipment. The damping of the submerged model assembly was estimated as δ_s = 0.16 relative-to-critical from video recordings at zero flow speed.

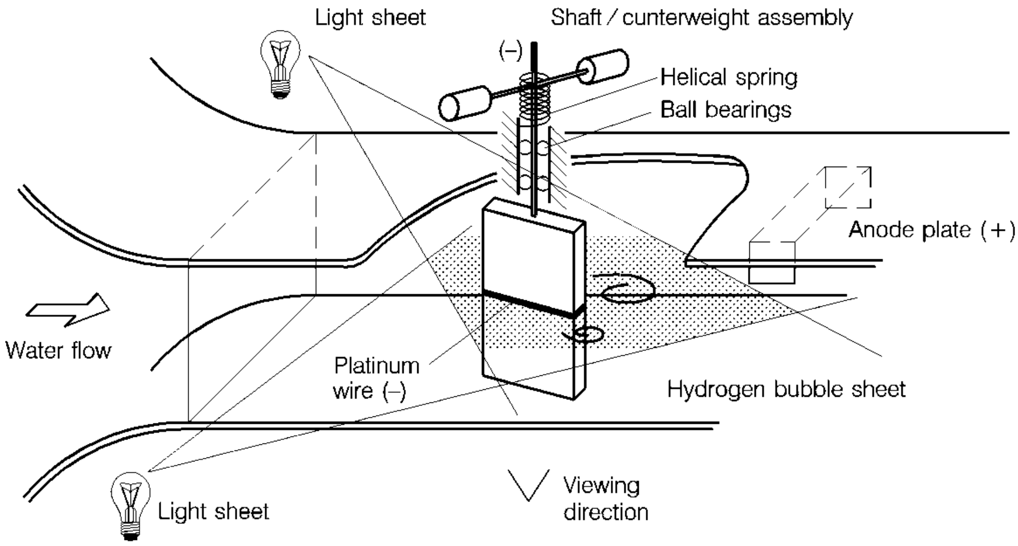

Figure 4.21 Model and flow visualization set-up in the ETH water tunnel.

The flow about the model was visualized using the hydrogen bubble technique, Schraub, Kline, Henry et. al. [18]. A 30 μm diameter platinum wire was wrapped around the mid-span section of the model and taken outside the tunnel via a canal in the vertical shaft to be connected to the cathode (-) of the DC voltage supply. The anode (+) was connected to a stainless steel plate projecting from the measurement section ceiling approximately 0.1 m downstream of the model. Hydrogen bubbles produced by the electrolysis process at the model surface and trapped in the flow were made visible by two light sheets emitted by standard 1000 W slide projectors. The flow pattern forming around the oscillating model was viewed "end on" and was recorded by a standard digital video camera.

A comparison between selected physical flow patterns recorded in the water tunnel and the corresponding simulated flow patterns developed around the H-section at a non-dimensional flow speed U/fB = 9.3 is shown in Figure 4.22. Also Figure 4.22 presents simulated time traces of the angular displacement from zero degree incidence (equilibrium position) and the fluid dynamic moment ($50 \cdot C_M$) acting at the centroid (rotational axis). From the time traces it is noted that the angular response is divergent as expected in case of an non-dimensional flow speed twice the threshold value. The reason for the divergent oscillations becomes obvious when observing the moment trace. It is noted that the moment is oscillatory and is leading the response and thus "driving" it. This behaviour is supported by the flow visualization clips and flow field simulations shown above and below the time traces.

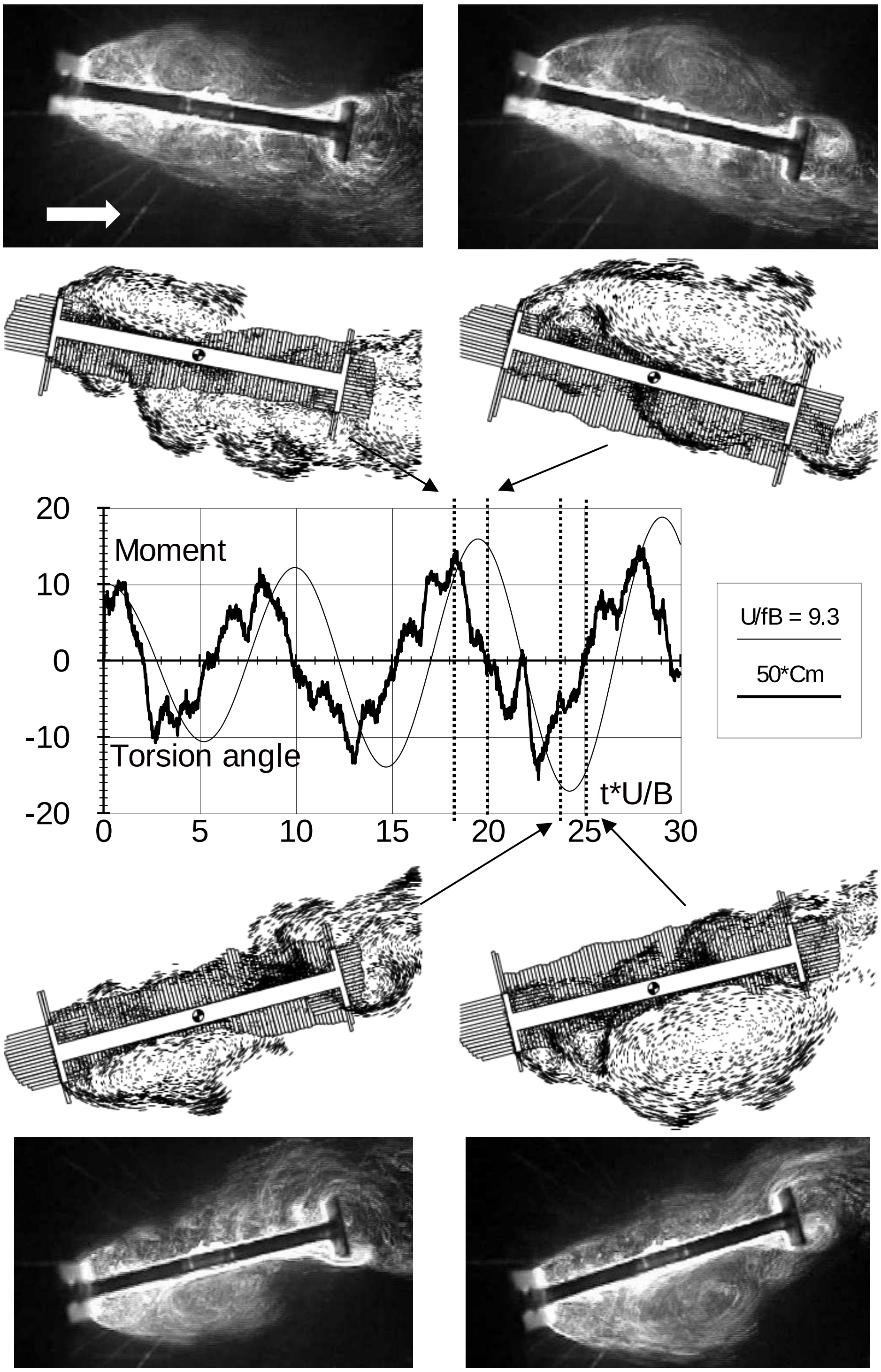

Figure 4.22 Comparison of the vortex movement and section twisting motion in a physical water tunnel model (hydrogen bubble visualization) and the corresponding discrete vortex model at $U/fB = 9.3$. The hatched area in the computer model shows the pressure distribution on the cross section. A region of low pressure is found below the centre of the vortices.

The top left video-clip and flow plot is obtained at non-dimensional time tU/B= 18.3 where the section is rotating towards the maximum angle of incidence. The leading edge vortex is at a position upstream of the centroid leading to minimum surface pressure here, thus yielding a nose-up moment. At tU/B = 20.0 the section is past the maximum angle of incidence and is being forced toward lower angles by the elastic force and the leading edge vortex has drifted to a position just above the centroid and the fluid dynamic moment is now zero. At tU/B = 23.5 the section has passed the equilibrium position and a new leading edge vortex has formed below the section upstream of the centroid yielding a nose-down (negative) moment. Still later at tU/B = 25.3 the section has passed the minimum angle of incidence and the new leading edge vortex has drifted to a position downwind of the centroid exerting a nose-up (positive) moment on the section which act together with the elastic force. Clearly the fluid dynamic moment, which is induced by the vortex formation and drift, drives the cross section in divergent oscillations and may be interpreted as "negative" damping.

To further emphasize the key finding that the leading edge vortex formation and drift is responsible for one-degree-of-freedom flutter of elongated bluff sections, flow visualization and simulations were carried out for trapezoidal cross section, which is known not to be prone to one-degree-of-freedom torsion flutter. The result is displayed in Figure 4.23 in similar format as Figure 4.22. From the time trace of torsion angle and moment it is noted that the oscillations convergent displaying decreasing amplitude with time. The moment trace is more or less in phase with the displacement trace indicating negligible fluid dynamic damping. An estimate of the damping from the displacement trace yields $\delta \approx 0.12$ in good agreement with the input damping of $\delta = 0.16$ (experimental damping level). Review of the flow visualization clips and flow field simulations reveal smaller vortices formed along section surface, but not the large drifting vortex structure that was apparent on the H-section shown in Figure 4.22. The absence of the drifting leading edge vortex on the trapezoidal box section is taken as a further support for the key role on the drifting vortex in one-degree-of-freedom flutter of bluff sections.

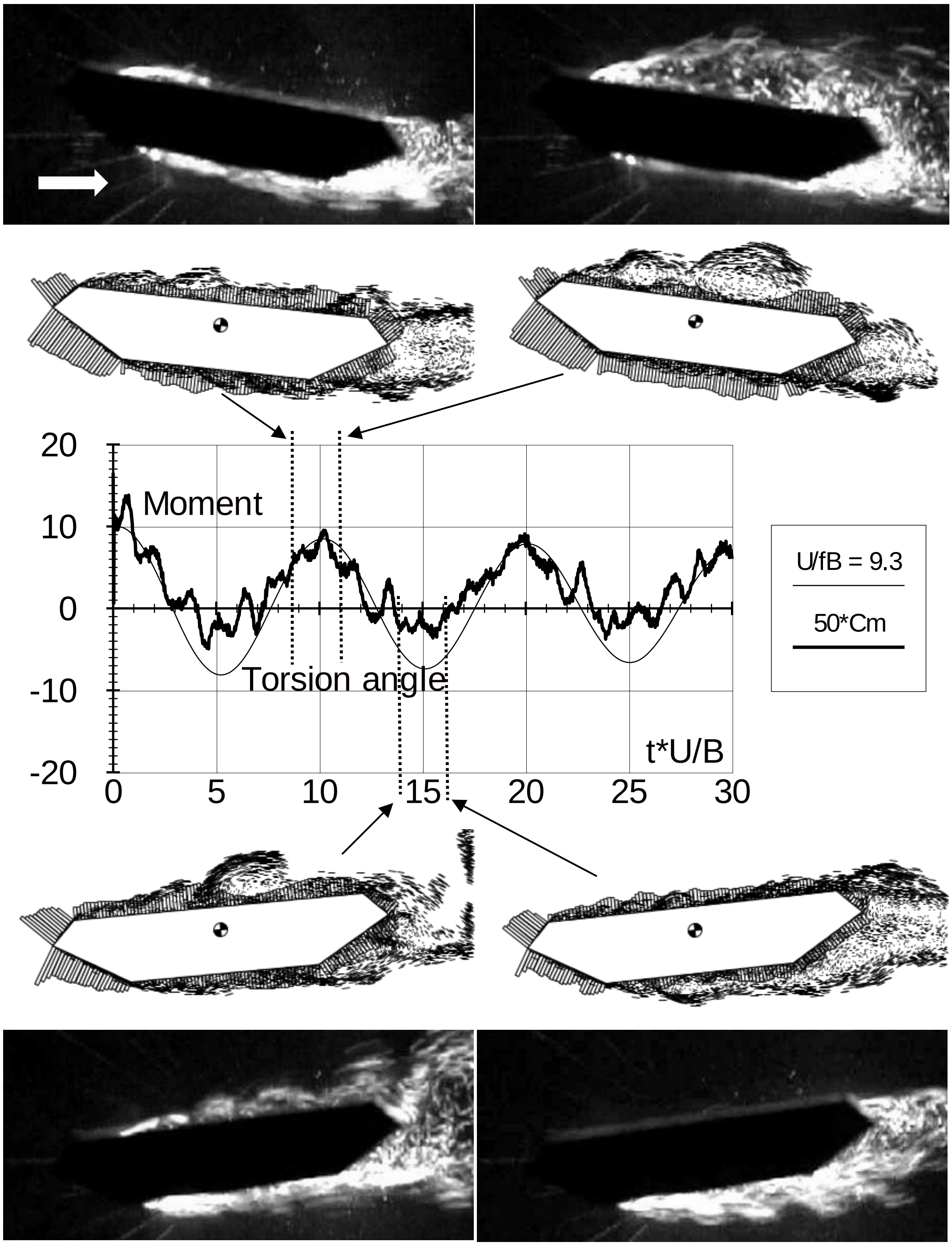

Figure 4.23 Simulations and flow visualizations of torsion oscillations of a trapezoidal box cross section at non-dimensional flow speed *U*/*fB* = 9.3.

The flow visualizations shown in Figure 4.22 are not the first to reveal the large coherent vortex structures forming just downstream of the windward vertical girder of the shallow H-section. The Carmody report [2] reproduced flow visualization pictures obtained in a water tank at the Case School of Applied Sciences. The asymmetric and distinct vortex pattern forming on the upper and lower sides of the model roadway lead von Kármán to propose that vortex formation behind the upwind vertical girder in some way was responsible for the observed self-induced vibrations of the deck cross section.

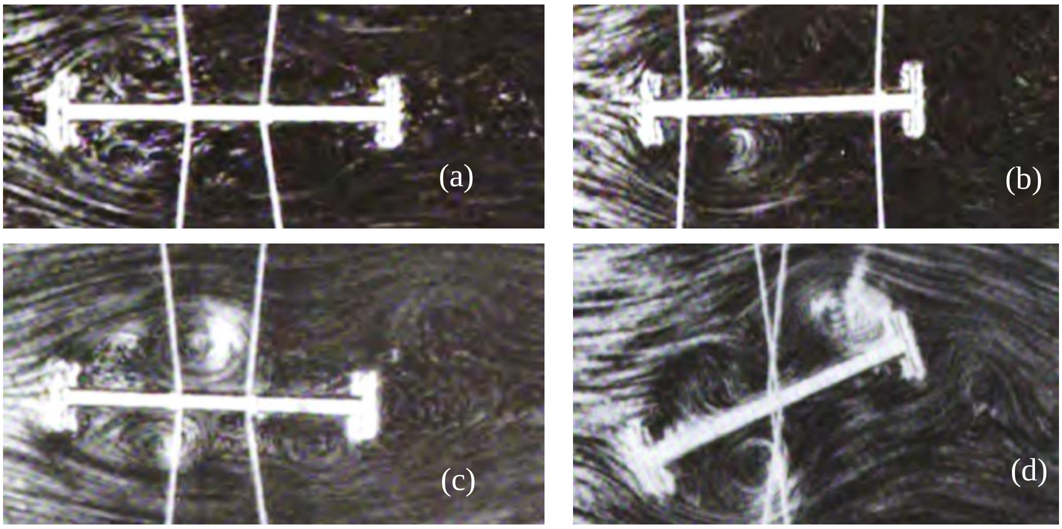

Figure 4.24 Visualization of flow about the shallow H-shaped section presented in the Carmody report [2]. (a) Section at rest displaying symmetric vortex formation on the upper and lower sides of the horizontal road deck. (b), (c), (d) Section performing self-induced torsion oscillations displays asymmetric vortex formation on the horizontal road deck.

Similar vortex patterns were also shown in flow visualizations performed by Nakamura and Nakashima [19] for the H-shaped section with and without the presence of a splitter plate inserted in the wake. An important conclusion of these experiments was that the self-induced vibrations were related to vortices forming on the cross section itself and not to vortex formation in the wake, which obviously was prevented when the splitter plate was inserted.

Miyata [11] in a review paper establishes that: *The mechanism of torsional flutter lead to the collapse* (of the Tacoma Narrows Bridge) *was caused by dynamic vortex separation from the windward edges of the vertical stiffening girder that descends along the floor web always synchronized with the torsional motion*. This statement is backed by the flow visualization pictures reproduced in Figure 4.25

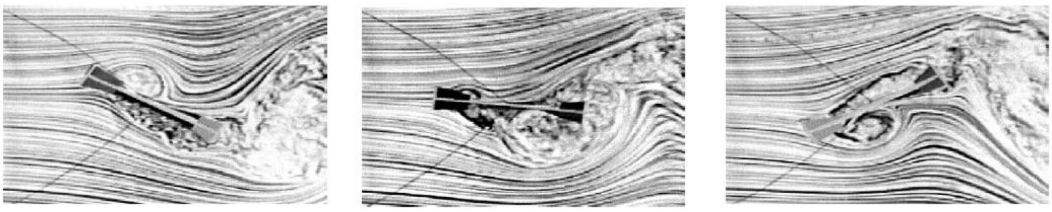

Figure 4.25 Flow visualization of the formation and drift of vortices on a generic model of the Tacoma Narrows H-section. From Miyata [11]

4.10 Dynamic vortex model for asymmetric deck sections

The discussion of one-degree-of-freedom flutter has to this point focussed on the stability of the shallow H-shaped cross section, which is symmetric about a horizontal plane through the roadway. Other plate girder section designs may be asymmetric about a horizontal plane and thus offer different aerodynamic characteristics depending on whether they twist in the nose up or nose down direction. A channel shaped section with triangular nose fairings  may thus act aerodynamically as a semi streamlined trapezoidal box section when twisting nose upwards but as a shallow H-section when twisting nose downwards. An estimate of the aerodynamic torsion damping for such a type of section can be obtained by combining the quasi-steady aerodynamic damping model for flat plate airfoil (11) over the first half of an oscillation circle with travelling point vortex model (23) over the second half of the oscillation circle. It is assumed that the moment slope of the flat plate airfoil is $\partial C_M/\partial\alpha_0 = \pi/2$ and that the ratio of the moment slope to the lift slope is r = 0.25. From Figure 4.26 it is noted that the effect of the flat plate aerodynamic damping present over one half of the oscillation circle is to push the zero crossing of the δ_a/μ to higher non-dimensional wind speeds than U/fB = 4 which is characteristic for the travelling vortex model.

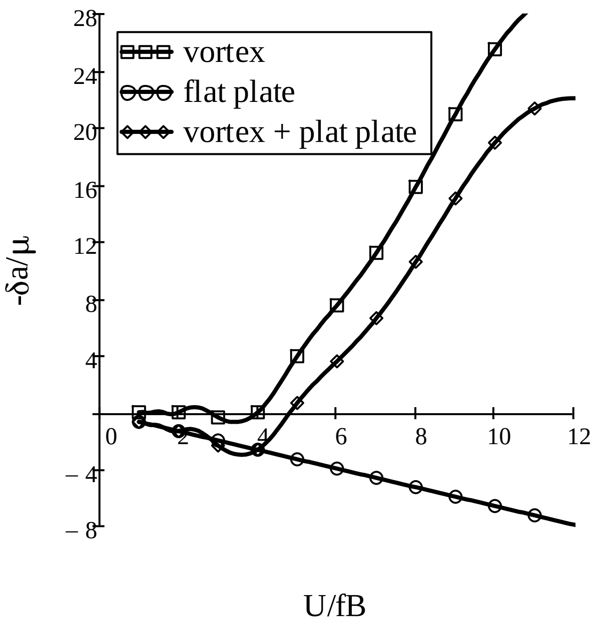

Figure 4.26 Combined aerodynamic damping (◊) due to the travelling vortex (□) over half an oscillation circle and the aerodynamic damping developed by a flat plate (○) over the other half of the oscillation circle.

4.11 Vortex models expressed in terms of the A_2^* aerodynamic derivative

Scanlan and Tomko expressed the aerodynamic damping in torsion in terms of the A_2^* aerodynamic derivative, which is a function of non-dimensional wind speed and is defined as follows:

$$A_2^* = \frac{2I\zeta_a}{\rho B^4} = \frac{\delta_a}{\pi}\left(\frac{I}{\rho B^4}\right) \tag{4.42}$$

As will be seen later and perhaps intuitively, it is more appropriate to normalise the torsion damping by the rotary inertia ratio $I/\rho B^4$ than the linear mass ratio μ chosen in the Carmody report. Negative aerodynamic damping responsible for self-induced oscillations is thus represented by positive values of A_2^*. With the above definition the vortex models for the aerodynamic damping are easily converted to expressions for A_2^*. The A_2^* equivalent of the travelling point vortex damping assuming is obtained as:

$$A_{2p}^*(U^*) = \frac{1}{8\pi^2}(U^*)^2 \frac{C_{M0}}{\alpha} \frac{\left(\frac{U^*}{4\pi}\left(1 - \cos\left(\frac{8\pi}{U^*}\right)\right) - \sin\left(\frac{8\pi U^*}{U^*}\right)\right)}{\left(\frac{8\pi}{U^*} + \frac{1}{2}\sin\left(\frac{16\pi}{U^*}\right)\right)} \tag{4.43}$$

A similar expression for the expanding vortex model is obtained as:

$$A_{2e}^*(U^*) = \frac{1}{32\pi^3}(U^*)^3 \frac{1}{\alpha}$$
$$\frac{\left(\frac{U^*}{4\pi}\right)\sin\left(\frac{4\pi}{U^*}\right)\left(3 - 2\cos\left(\frac{4\pi}{U^*}\right)\right) + \frac{1}{2}\left(\cos\left(\frac{8\pi}{U^*}\right) - \cos\left(\frac{4\pi}{U^*}\right)\right) - 1}{\left(\frac{8\pi}{U^*} + \frac{1}{2}\sin\left(\frac{16\pi}{U^*}\right)\right)} \tag{4.44}$$

Where $U^* = U/fB$ is the non-dimensional wind velocity.

A comparison of A_2^* obtained from (4.44) and directly from discrete vortex simulations is shown in Figure 4.27. A_2^* values obtained from (4.44) are multiplied by ½ in order to conform to the original normalisation by $\rho U^2 B$ utilized in [8].

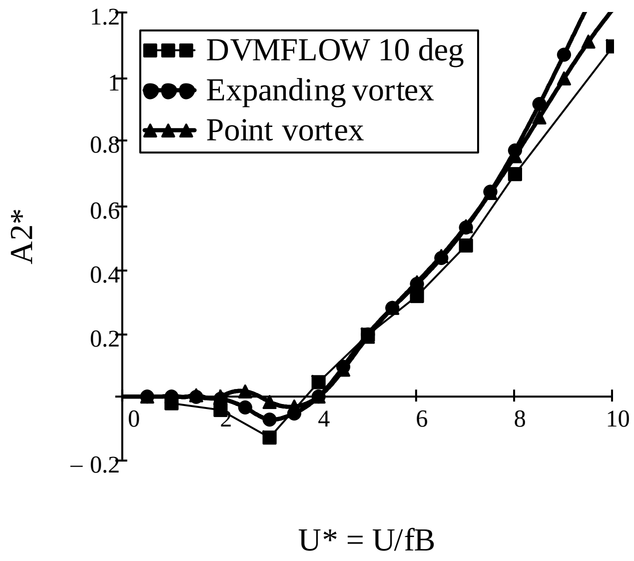

Figure 4.27 Comparison of the A_2^* aerodynamic derivative for the shallow H-section obtained from (32) and directly discrete vortex simulations.

4.12 The Tacoma Narrows collapse and von Kármán vortex shedding excitation

The Tacoma Narrows Bridge collapse is sometimes attributed to resonance between von Kármán vortex shedding in the wake of the bridge girder and the eigenmodes of the bridge – a wrong conclusion as thoroughly explained by Billah and Scanlan [20]. In view of this common misunderstanding, it is appropriate to stress the fundamental difference between the travelling point vortex process leading to one-degree-of-freedom flutter and that of classical von Kármán vortex shedding. One-degree-of-freedom flutter or torsion flutter is controlled entirely by the time-scale of the structural motion, i.e. the torsion frequency. The instability will be encountered once the wind speed transcends the critical value given by (4.41) at which more energy is supplied by the wind than dissipated by the structural damping. In contrast the frequency f_v of von Kármán vortex shedding is governed by a time-scale set by a characteristic dimension of the section B and the approach mean wind speed U. Vortex shedding response is understood as a resonance phenomenon occurring at wind speeds when the vortex shedding frequency f_v is close to or coincides with a structural eigenfrequency f. The University of Washington report [3] identifies the relationship between wind speed, deck width and vortex shedding frequency as $U/f_vB = 2.06$. This is only half the non-dimensional wind speed for onset of the torsion instability and at = U/f_vB =2.06 the section possesses positive aerodynamic damping according to the GALCIT experimental data in Figure 4.1 (left). At a wind speed of 19 m/s the von Kármán vortex shedding frequency would be $f_v = 0.77$ Hz almost 4 times the torsion frequency f =0.2 Hz of the bridge and thus way off resonance.

As mentioned in section 3.2, the Tacoma Narrows Bridge had encountered von Kármán vortex shedding oscillations at many occasions during its short life but always in a vertical mode [2], [3]. From Figure 4.28 it is quite clear that the vertical von Kármán oscillations (1-V, 2-V) are of limited amplitude and that they occur in a limited wind speed range starting when the vortex shedding frequency becomes at resonance with the structural eigenfrequency. In contrast, the response in the torsion mode (1-T) grows with increasing amplitudes for increasing wind speeds once a threshold wind speed has been exceeded.

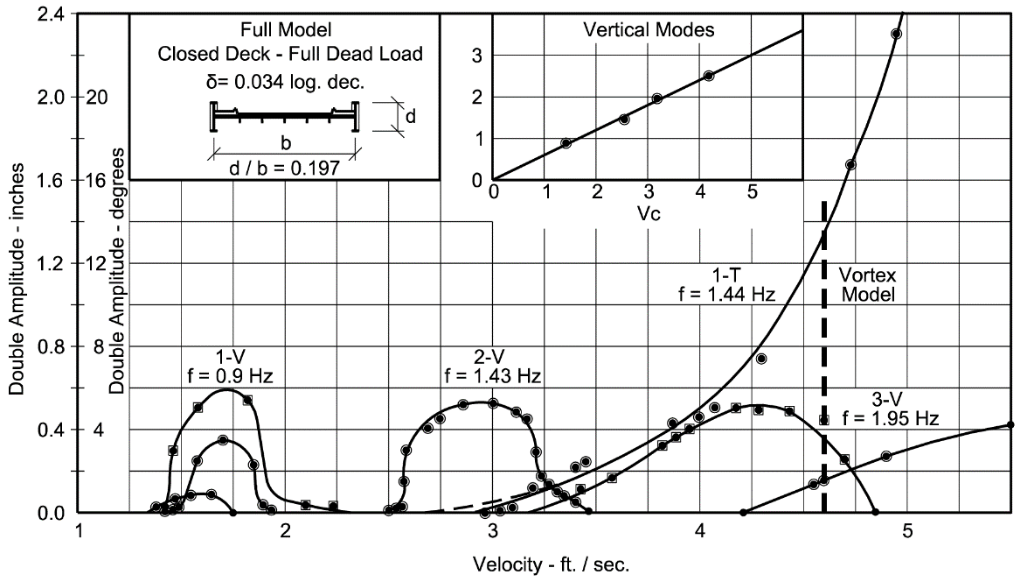

Figure 4.28 Wind induced response as function of model wind speed of the 1:50 scale Tacoma Narrows full aeroelastic bridge model tested at the University of Washington Experimental Station [3]. The heavy dashed line marks the onset wind speed of flutter calculated according to (4.13).

5. Two-degree-of-freedom Flutter

Having discussed a mathematical model for one-degree-of-freedom flutter in detail it is appropriate to review the fundamentals of the mathematical model for two-degree-of-freedom bridge flutter as an introduction to recent developments in the field. Before embarking on the development of the aerodynamic loading on a bridge deck undergoing small amplitude in oscillatory motion, it is helpful to review the physics of the steady-state lift and moment developed on a generic model of a semi-streamlined bridge deck at a small angle of incidence to the wind.

5.1 Vortex model of a stationary bridge deck at incidence to the wind

Streamlined bridge decks and airfoils experience a crosswind lift and twisting moment when subjected to a steady stream of air at incidence. The simplest possible model of the resulting aerodynamic forces is a single potential flow vortex located at the ¼ chord point of the deck, Figure 5.1. The strength Γ of the bound vortex and thus lift and moment is found by equating the circumferential velocity w introduced by the vortex in the ¾ chord point (control point) to the vertical projection of the free stream velocity U normal to the deck nose-tail line (chord). This is a manifestation of the Kutta-Jukowski theorem which states that that flow at the trailing edge of the deck shall be parallel to the nose-tail line and that the wind cannot flow through the solid boundary of the deck. In mathematical terms this simple vortex model follows from the Biot-Savart theorem and may be expressed as:

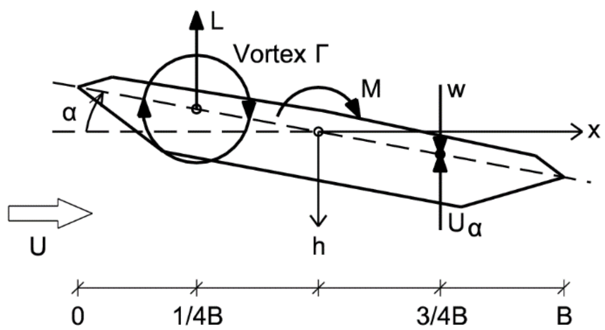

Figure 5.1 Simple vortex model for lift force and moment on a stationary streamlined deck section at incidence to the wind. The right hand coordinate system is chosen to have the vertical axis positive downwards in accordance with Theodorsens theoretical treatment [5]

$$U \sin\alpha + w \approx U\alpha + w = U\alpha + \frac{\Gamma}{2\pi\left(x_{1/4} - x_{3/4}\right)} = 0 \tag{5.1}$$

The lift force L is related to the circulation as follows:

$$L = \rho U \Gamma \tag{5.2}$$

Thus the lift coefficient is obtained as:

$$C_L = \frac{L}{½\rho U^2 B} = \frac{\Gamma}{½UB} \tag{5.3}$$

Inserting $x_{1/4} = -B/4$ and $x_{3/4} = B/4$ in (5.1) and substituting the resulting circulation in (5.3) yields the well-known results for the lift and moment coefficients relative to the mid-chord position:

$$C_L = -2\pi\alpha \tag{5.4}$$

$$C_M = \frac{M}{½\rho U^2 B^2} = \frac{L\cdot(-B/4)}{½\rho U^2 B^2} = \frac{\pi}{2}\alpha \tag{5.5}$$

The lift and moment slopes are finally obtained from (5.4) and (5.5) by differentiation with respect to α:

$$\frac{\partial C_L}{\partial \alpha} = -2\pi \tag{5.6}$$

$$\frac{\partial C_M}{\partial \alpha} = \frac{\pi}{2} \tag{5.7}$$

The lift and moment slopes in (5.6) and (5.7) are theoretical values determined by potential flow theory which does not account for real fluid effects such as viscosity. In a real viscous flow internal shear forces will create a boundary layer which will tend to separate once the angle of attack α reaches angles of about 15 deg in which case (5.6) and (5.7) are no longer valid. Geometrical obstacles such as finite thickness of the bridge deck and railings also tend to promote flow separation and thus make lift and moment coefficients for real bridge deck structures diverge from the potential flow values.

5.2 Vortex model for aeroelastic loads on a bridge deck in oscillatory small amplitude motion

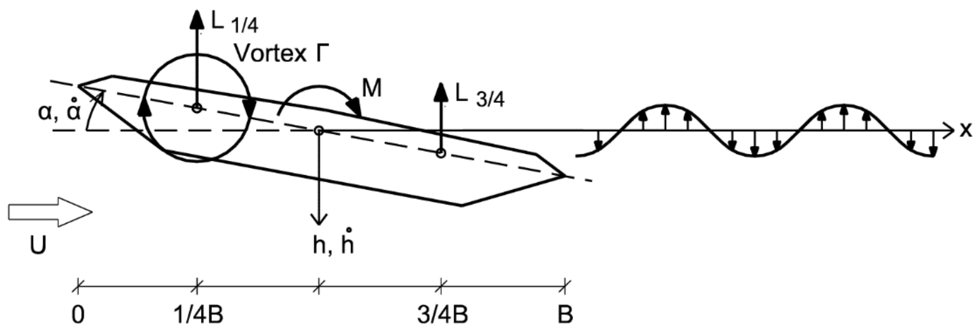

Figure 5.2 Simple vortex model for a bridge deck in oscillatory bending motion and twist about mid-chord indicating position of bound vortex and vertical wake extending form the trailing edge to infinity.

The single vortex model is still valid for streamlined bridge decks in small amplitude oscillatory motion but the strength of the bound vortex is modified by a continuous vortex sheet shed in the wake of the deck by virtue of the Helmholtz theorem. This configuration is sketched in Figure 5.2

The strength of the wake vorticity γ is governed by the time rate of change of the strength of the bound vortex thus the lift force in the ¼ chord point will now have a component in phase with the structural displacement as well as in phase with the structural velocity of the ¾ chord point and will be of smaller amplitude. Splitting of the aerodynamic forces into components in phase with structural displacement and velocity is a consequence of the oscillatory trailing wake and the aerodynamic factor governing for two-degree-of-freedom flutter. Non-circulatory effects associated with the finite chord length of the deck cannot be predicted from the single vortex model but must be introduced from Thoedorsens theory [5] in which the bound circulation is distributed along the chord length of the deck.

The model for the aerodynamic forces acting on the deck section in oscillatory motion is obtained similarly to (5.1) by equating the vertical velocity induced by the bound vortex and the trailing vertical wake to the vertical structural velocity of the ¾ chord point:

$$U\alpha + \frac{B}{4}\dot{\alpha} + \dot{h} + \frac{\Gamma}{2\pi(B/2)} + \frac{1}{2\pi}\int_0^\infty \frac{\gamma(t,x)}{x_{3/4} - x}dx = 0 \tag{5.8}$$

For harmonic motion $\alpha(t) = \alpha \cdot e^{i\omega t}$, $h(t) = h \cdot e^{i\omega t}$ of the bridge deck the bound vorticity is also assumed to be harmonic in time $\Gamma(t) = \Gamma \cdot e^{i\omega t}$ thus the vertical wake is assumed to be harmonic both in time and space $\gamma(t,x) = \gamma \cdot e^{i\omega t}e^{-i(\omega/U)x}$. Introducing the non-dimensional coordinate $\xi = 2x/B$ in the wake integral and observing the spatial harmonic structure of the wake allows (5.8) to be expressed as:

$$\Gamma + \frac{\gamma B}{2}\int_0^\infty \frac{e^{-i\frac{K}{2}\xi}}{\xi_{3/4} - \xi}d\xi = -\pi B\left(U\alpha + \frac{B}{4}\dot{\alpha} + \dot{h}\right) \tag{5.9}$$

where $K = \omega B/U$ is the non-dimensional frequency.

Solution of (5.9) is possible once a relation between Γ and γ is established. Such a relation is provided by Hemholtz theorem which states that the sum of vorticity in a given domain remains constant at any time. At the trailing edge ($\xi = 0$) the Helmholtz theorem transforms to the statement that the rate of change of the bound circulation must be balanced by the strength / unit length of the trailing wake swept downwind with the mean wind speed U:

$$\frac{d\Gamma}{dt} + U\gamma_{\xi=0} = 0 \tag{5.10}$$

Introducing the harmonic time dependence $e^{i\omega t}$ in (5.10) yields the following relation between Γ and γ:

$$\gamma = -i\frac{\omega}{U}\Gamma \tag{5.11}$$

Equation (5.11) may now be put in its final form:

$$\Gamma\left(1 - i\frac{K}{2}\int_0^\infty \frac{e^{-i\frac{K}{2}\xi}}{\xi_{3/4} - \xi}d\xi\right) = -\pi B\left(U\alpha + \frac{B}{4}\dot{\alpha} + \dot{h}\right) \tag{5.12}$$

Introducing (5.12) into (5.3) yields the following expression for the lift coefficient C_L^Γ of the lift force $L_{1/4}$ in the ¼ point due to the bound vortex:

$$C_L^\Gamma = -2\pi \cdot c(K)\left(\alpha + \frac{B}{4U}\dot{\alpha} + \frac{\dot{h}}{U}\right) \tag{5.13}$$

where:

$$c(K) = \frac{1}{\left(1 - i\frac{K}{2}\int_0^\infty \frac{e^{-i\frac{K}{2}\xi}}{\xi_{3/4} - \xi}d\xi\right)} \tag{5.14}$$

$c(K)$ is the single vortex equivalent of the well-known Theodorsen circulation function $C(K)$ which is valid for the case where the circulation is distributed over the entire length of the deck chord B. The integral over the wake (5.14) may be expressed in terms of the exponential integral, Abramowitz and Stegun [21] and evaluated by standard numerical methods:

$$\int_0^\infty \frac{e^{-i\frac{K}{2}\xi}}{\xi_{3/4} - \xi}d\xi = -e^{-i\frac{K}{2}\xi_{3/4}}E_1(\xi_{3/4}) \tag{5.15}$$

The complimentary equation for the aerodynamic moment due to the bound circulation is obtained similarly to (5.13) by substitution of (5.12) into (5.5):

$$C_M^\Gamma = \frac{\pi}{2} \cdot c(K)\left(\alpha + \frac{B}{4U}\dot{\alpha} + \frac{\dot{h}}{U}\right) \tag{5.16}$$

The single vortex model for the oscillation streamlined bridge deck is evaluated by comparison of the "single vortex" circulation function $c(K)$ to the Theodorsen circulation function $C(K)$ valid for the "flat plate" airfoil with distributed bound vorticity, Fung [22]. Figure 5.3 compares the real and imaginary parts $F(K)$, $G(K)$ of the Theodorsen circulation function to the real and imaginary parts $f(K)$, $g(K)$ of $c(K)$. Reasonable agreement is demonstrated for $K < 0.5$. Numerical evaluation of the circulation functions is detailed in Appendix B.

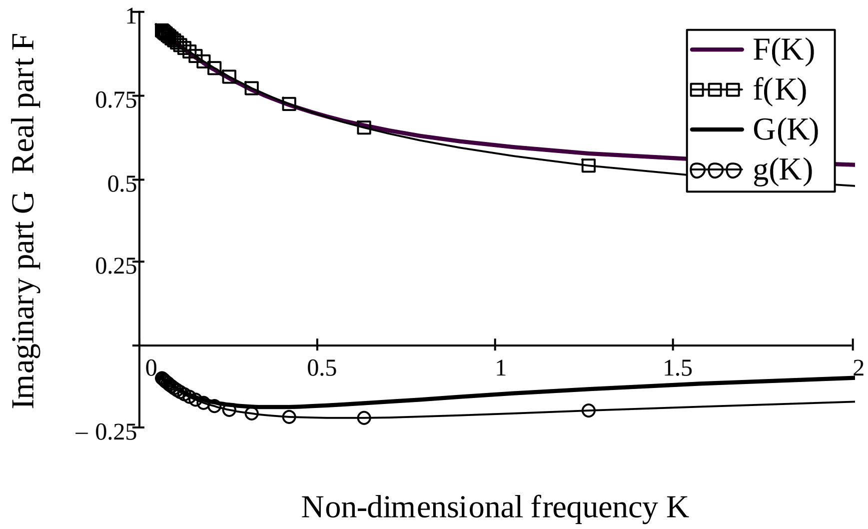

Figure 5.3 Comparison of real and imaginary parts F, G of the Theodorsen circulation function (heavy line) to real and imaginary parts of the "single vortex" circulation function equation (46) (light line, markers).

Equations (5.13) and (5.16) model the effect of the oscillatory lift force $L_{1/4}$ and moment due to the bound circulation. As indicated in Figure 5.2 a second lift force $L_{3/4}$ which acts in the ¾ chord point and corresponding moment $M_{3/4}$ exists. These forces are associated with the centrifugal action and the added mass $m_a = \pi\rho(B/2)^2$ of the air entrained by oscillatory motion of the deck, [22]:

$$L_{3/4} = -\pi\rho(B/2)^2 U\dot{\alpha} \qquad (5.17)$$

$$M_{3/4} = L_{3/4} \cdot (B/4) = \frac{-\pi}{2}\rho(B/2)^3 U\dot{\alpha} \qquad (5.18)$$

Or in non-dimensional form:

$$C_L^{3/4} = \frac{L_{3/4}}{½\rho U^2 B} = -2\pi \frac{B}{4U}\dot{\alpha} \qquad (5.19)$$

$$C_M^{3/4} = \frac{M_{3/4}}{½\rho U^2 B^2} = \frac{-2}{\pi}\frac{B}{4U}\dot{\alpha} \qquad (5.20)$$

Finally inertia forces associated with acceleration of the added mass may be added

$$L^a = -\pi\rho(B/2)^2\ddot{h} \qquad (5.21)$$

$$M^a = \pi\rho(B/2)^2(B/4)^2\ddot{\alpha} \qquad (5.22)$$

Which can be expressed in non-dimensional coefficient form as:

$$C_L^a = \frac{L^a}{½\rho U^2 B} = -\frac{\pi}{2}\frac{B}{U^2}\ddot{h} \tag{5.23}$$

$$C_M^a = \frac{M_{3/4}}{½\rho U^2 B^2} = -\frac{\pi}{64}\frac{B^2}{U^2}\ddot{\alpha} \tag{5.24}$$

From (5.21) and (5.22) it is noted that the forces due to acceleration of the added mass is independent of the wind speed U. For analysis purposes it can thus be chosen to include the added inertia with the structural inertia or subtract them from the aerodynamic forces. Often it is found that the added inertia is small in comparison to the structural inertia and can be neglected.

Addition of the ¾ chord forces to the circulatory terms yields the form of the aeroelastic load coefficients for the oscillating bridge deck presented by Bleich [4] save that half the chord length $b = B/2$ was used as characteristic dimension instead of B.

$$C_{Lae} = \left[\frac{\partial C_L}{\partial \alpha}C(K)\left(\alpha + \frac{\dot{h}}{U}\right) + \frac{B}{4U}\dot{\alpha}\left(\frac{\partial C_L}{\partial \alpha}C(K) + 2\pi\right) - \frac{\pi}{2}\left(\frac{B}{U^2}\right)\left(\frac{\ddot{h}}{B}\right)\right] \tag{5.25}$$

$$C_{Mae} = \left[\frac{\partial C_M}{\partial \alpha}C(K)\left(\alpha + \frac{\dot{h}}{U}\right) + \frac{B}{4U}\dot{\alpha}\left(\frac{\partial C_M}{\partial \alpha}C(K) - \frac{\pi}{2}\right) - \frac{\pi}{64}\left(\frac{B^2}{U^2}\right)\ddot{\alpha}\right] \tag{5.26}$$

In (5.25), (5.26) the theoretical "flat plate" derivatives -2π and $\pi/2$ has been replaced by the more general terms $\partial C_L/\partial \alpha$ and $\partial C_M/\partial \alpha$ for future reference.

Equations (5.25) and (5.26) are in a mixed form format as the assumption of harmonic motion for flutter was evoked for derivation of the circulation function. Introducing $\alpha(t) = \alpha \cdot e^{i\omega t}$, $h(t) = h \cdot e^{i\omega t}$ in (5.25) and (5.26) and letting $K = \omega B/U$ allows the equations to be recast in complex algebraic form. $C(K)$ (or $c(K)$) has been replaced by its real and imaginary parts $F(K) = F$ and $G(K) = G$. The final form of the aeroelastic lift and moment L_{ae} and M_{ae} normalized by dynamic head and characteristic dimension is finally obtained as:

$$\begin{aligned}\frac{L_{ae}}{½\rho U^2 B} = \Bigg[&\frac{\partial C_L}{\partial \alpha}\left(F - \frac{K}{4}G\right)\alpha + i\left(\frac{\partial C_L}{\partial \alpha}\left(G + \frac{K}{4}F\right) - \frac{\pi}{2}K\right)\alpha \\ &+ \left(\frac{\pi}{2}K^2 - \frac{\partial C_L}{\partial \alpha}KG\right)\left(\frac{h}{B}\right) + i\frac{\partial C_L}{\partial \alpha}KF\left(\frac{h}{B}\right)\Bigg]\end{aligned} \tag{5.27}$$

$$\begin{aligned}\frac{M_{ae}}{½\rho U^2 B^2} = \Bigg[&\left(\frac{\partial C_M}{\partial \alpha}\left(F - \frac{K}{4}G\right) + \frac{\pi}{64}K^2\right)\alpha \\ &+ i\left(\frac{\partial C_M}{\partial \alpha}\left(G + \frac{K}{4}F\right) - \frac{\pi}{8}K\right)\alpha - \frac{\partial C_M}{\partial \alpha}KG\left(\frac{h}{B}\right) \\ &+ i\frac{\partial C_M}{\partial \alpha}KF\left(\frac{h}{B}\right)\Bigg]\end{aligned} \tag{5.28}$$

A few comments are appropriate at this point. First it is noted that the oscillatory aeroelastic lift and moment coefficients are both functions of the reduced frequency, are complex valued and have components proportional to the non-dimensional torsion and bending displacement α, (h/B) as well as the torsion and bending velocities $i\alpha$, $i(h/B)$. Secondly it is noted that the aeroelastic loads tends to their steady values for vanishing non-dimensional frequency $K \to 0$ as $F(K) \to 1$ and $G(K) \to 0$, Figure 5.3.

5.3 Scanlans model of aeroelastic loads on a bridge deck in small amplitude oscillatory motion

Scanlan and Tomko [8] proposed the model for the aeroelastic loads on a bridge deck in oscillatory motion presented in section 3.3. This model borrows from Theodorsens potential flow model as it specifies the same dependence of the loads on the components of motion as (5.27), (5.28) but with the theoretical determined coefficients replaced by experimental data:

$$\frac{L_{ae}}{\rho U^2 B} = \left[K H_1^* \frac{\dot{h}}{U} + K H_2^* \frac{B\dot{\alpha}}{U} + K^2 H_3^* \alpha + K^2 H_4^* \frac{h}{B} \right] \tag{5.29}$$

$$\frac{M_{ae}}{\rho U^2 B^2} = \left[K A_1^* \frac{\dot{h}}{U} + K A_2^* \frac{B\dot{\alpha}}{U} + K^2 A_3^* \alpha + K^2 A_4^* \frac{h}{B} \right] \tag{5.30}$$

The original formulation [8] included 6 coefficients or aerodynamic derivatives $A_{1..3}^*$, $H_{1..3}^*$ which are functions of the non-dimensional wind speed U/fB or reduced frequency K and are to be determined from experiments. Also the aeroelastic forces were normalized by twice the dynamic head ρU^2 instead of $½\rho U^2$ which is common in aerodynamics. During the 80'ties the formulation of the aeroelastic loads was changed to include 8 aerodynamic derivatives (5.29), (5.30) in agreement with (5.27), (5.28). The normalizing head was also changed to $½\rho U^2$ in line with common aerodynamic practice. It is noted that the factor 2 in the normalizing head carries over in the numerical values of the aerodynamic derivatives. For practical applications of experimental data it is thus important to be aware of the underlying formulation. Aerodynamic derivatives measured in accordance with "new" formulation must be multiplied by ½ if applied in flutter calculation routines developed in accordance with the "early" formulation. For the present discussion the "early" formulation normalized by ρU^2 is retained.

The mixed format of (5.29), (5.30) can be changed by introducing the time complex formulation $\alpha(t) = \alpha \cdot e^{i\omega t}$, $h(t) = h \cdot e^{i\omega t}$ to yield:

$$\frac{L_{ae}}{\rho U^2 B} = K^2 \left[(H_4^* + iH_1^*) \frac{h}{B} + (H_3^* + iH_2^*) \alpha \right] \tag{5.31}$$

$$\frac{M_{ae}}{\rho U^2 B^2} = K^2 \left[(A_4^* + iA_1^*) \frac{h}{B} + (A_3^* + iA_2^*)\alpha \right] \tag{5.32}$$

Comparison of the individual coefficients to the α, $i\alpha$ and h/B, $i\,h/B$ terms in (5.29), (5.30) and (5.31), (5.32) yields theoretical expressions for the aerodynamic derivatives.

$$H_1^*(K) = \frac{1}{2K^2}\left[\frac{\partial C_L}{\partial \alpha} KF\right] \tag{5.33}$$

$$H_2^*(K) = \frac{1}{2K^2}\left[\frac{\partial C_L}{\partial \alpha}\left(G + \frac{K}{4}F\right) - \frac{\pi}{4}K\right] \tag{5.34}$$

$$H_3^*(K) = \frac{1}{2K^2}\left[\frac{\partial C_L}{\partial \alpha}\left(F - \frac{K}{4}G\right)\right] \tag{5.35}$$

$$H_4^*(K) = \frac{1}{2K^2}\left[\frac{\pi}{2}K^2 - \frac{\partial C_L}{\partial \alpha} KG\right] \tag{5.36}$$

$$A_1^*(K) = \frac{1}{2K^2}\left[\frac{\partial C_M}{\partial \alpha} KF\right] \tag{5.37}$$

$$A_2^*(K) = \frac{1}{2K^2}\left[\frac{\partial C_M}{\partial \alpha}\left(G + \frac{K}{4}F\right) - \frac{\pi}{8}K\right] \tag{5.38}$$

$$A_3^*(K) = \frac{1}{2K^2}\left[\frac{\partial C_M}{\partial \alpha}\left(F - \frac{K}{4}G\right) + \frac{\pi}{64}K^2\right] \tag{5.39}$$

$$A_4^*(K) = \frac{1}{2K^2}\left[-\frac{\partial C_M}{\partial \alpha} KG\right] \tag{5.40}$$

The aerodynamic derivatives for the flat plate is obtained by replacing $\partial C_L/\partial\alpha$ by -2π and $\partial C_M/\partial\alpha$ by $\pi/2$ in (5.33) – (5.40).

Other formulations of the aeroelastic forces on bridge decks are available in the literature [11], [23]. However, the Scanlan formulation has gained a certain popularity amongst practitioners in the field of bridge aerodynamics and appears to be the "de facto" industry standard today.

5.4 Assembly of the flutter equations

The flutter equations are assembled by combining the aeroelastic forces with the equations of motion for a one-degree-of-freedom oscillator. One for each degree-of-freedom to be considered. The simplest possible case is the two-degree-of-freedom motion allowed in a spring supported section model for which the flutter equations can be written as:

$$I\ddot{\alpha} + 2\zeta_\alpha I\omega_\alpha\dot{\alpha} + I\omega_\alpha^2\alpha = \rho U^2 B^2 K^2 \left[(A_4^* + iA_1^*)\frac{h}{B} + (A_3^* + iA_2^*)\alpha \right] \tag{5.41}$$

$$Bm\frac{\ddot{h}}{B}+2\zeta_h m\omega_h\frac{\dot{h}}{B}+m\omega_h^2\frac{h}{B} = \rho U^2 BK^2\left[(H_4^*+iH_1^*)\frac{h}{B}+(H_3^*+iH_2^*)\alpha\right] \tag{5.42}$$

Equations (5.41) and (5.42) can be cast into complex algebraic form assuming harmonic motion at a common frequency ω on the left hand side of the equations:

$$(\omega_\alpha^2+i2\zeta_\alpha\omega_\alpha\omega-\omega^2)\alpha=\frac{\rho B^4}{I}\omega^2\left[(A_4^*+iA_1^*)\frac{h}{B}+(A_3^*+iA_2^*)\alpha\right] \tag{5.43}$$

$$(\omega_h^2+i2\zeta_h\omega_h\omega-\omega^2)\frac{h}{B}=\frac{\rho B^2}{m}\omega^2\left[(H_4^*+iH_1^*)\frac{h}{B}+(H_3^*+iH_2^*)\alpha\right] \tag{5.44}$$

The 8 flutter coefficients or aerodynamic derivatives $A_1^*..A_4^*$, $H_1^*..H_4^*$ appearing on the right hand side of equations (5.43), (5.44) are to be determined from wind tunnel tests and are functions of the wind speed U and the frequency ω of motion. It is common practice to present the flutter coefficients as functions of the non-dimensional wind speed U/fB where $f=\omega/2\pi$ and B is the deck width. An example of the aerodynamic derivatives measured according to Scanlans "early" definition (normalization by ρU^2) and obtained for the deck of the Izmit suspension bridge Figure 5.4 is shown in Figure 5.5.

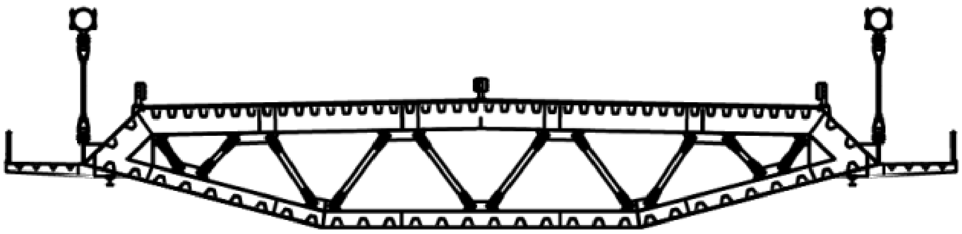

Figure 5.4 Trapezoidal box girder bridge deck cross section of the Izmit Suspension Bridge

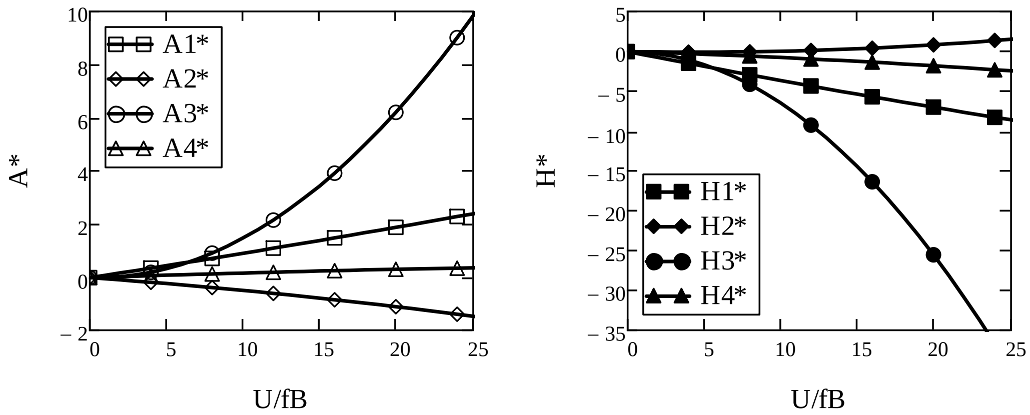

Figure 5.5 Aerodynamic derivatives or flutter coefficients for the Izmit suspension bridge deck section obtained from forced motion wind tunnel tests.

From Figure 5.5 it is noted that the aerodynamic are all zero at zero wind speed at which the torsion and vertical degrees-of-freedom are uncoupled. At higher wind speeds the flutter coefficients introduces coupling between the torsion and vertical degree of freedom which are proportional to displacement and velocity respectively, but they also changes the magnitude and phase angle of the aerodynamic lift force and moment relative to the instant torsion angle. The reason being that the aerodynamic force and moment acting on the moving deck is composed of two parts, a bound stationary vortex Γ situated approximately at the upwind ¼ deck width point and an oscillating sheet of vorticity shed in the wake as outlined in section 5.2. In contrast the aerodynamic forces on a stationary deck at inflow angle are related to the bound vortex only.

To gain insight into how the flutter coefficients influences the otherwise uncoupled structural two-degree-of-freedom system it is useful to observe the frequency response function of (5.43), (5.44) i.e. the ratio of the response to a dynamic force relative to a static force for varying wind speeds and different ratios of the natural frequency of torsion ω_α and vertical ω_h motion, Figure 5.6.

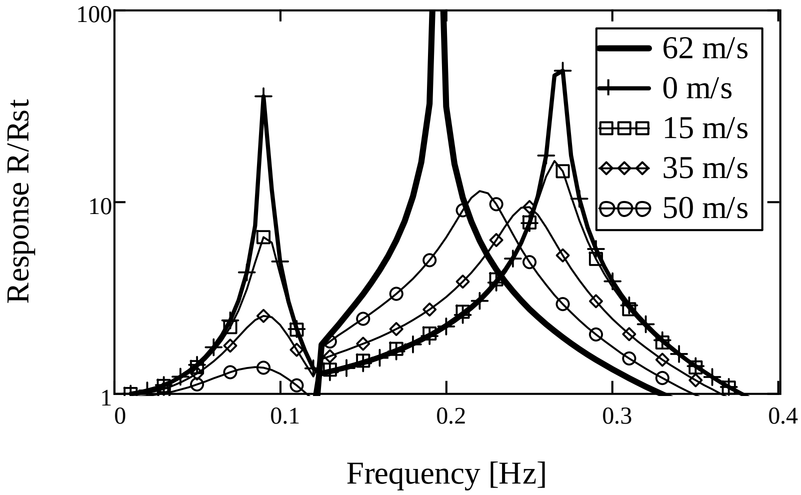

Figure 5.6 Frequency response plots for the Izmit suspension bridge deck section model. Frequency ratio $\omega_\theta/\omega_z = 2.93$ (as designed).

For $U = 0$ a distinct peak for each of the natural frequencies are observed. For increasing wind speeds the peaks becomes lower signifying increased damping of the motion with the vertical peak being at the same frequency as for zero wind speed but with the torsion peak moving progressively towards lower frequencies. At the critical wind speed ($U_c = 62$ m/s in the $\omega_\theta/\omega_z = 2.93$ case) the torsion peak becomes un-damped with the response tending to infinity which marks the flutter point. For $\omega_\theta/\omega_z = 1.67$, the behavior repeats but the flutter point is now at lower critical wind speed $U_c = 55$ m/s emphasizing the importance of the frequency ratio. Inertia and frequency data relevant to the Izmit suspension bridge are presented in section 5.5.

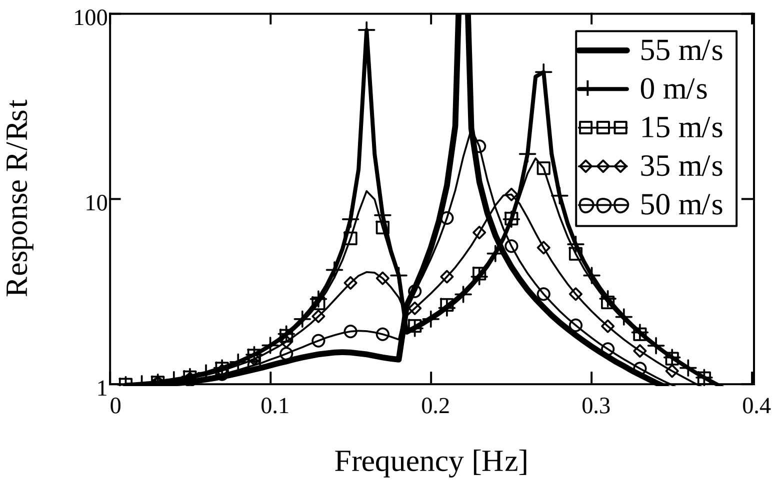

Figure 5.7 Frequency response plots for the Izmit suspension bridge deck section model. Frequency ratio $\omega_\theta/\omega_z = 1.67$.

The flutter equations (5.43), (5.44) can be solved for critical wind speed and flutter frequency by different methods. Two such methods are outlined in the following sections.

5.5 Solution of the flutter equations, the Theodordsen method

A first step for solving the flutter equations is to arrange the flutter equations (5.43), (5.44) in matrix form:

$$\begin{bmatrix} \left(\frac{\omega_\alpha}{\omega}\right)^2 + i2\zeta_\alpha\left(\frac{\omega_\alpha}{\omega}\right) - 1 - A_{\alpha\alpha} & -A_{\alpha h} \\ -H_{\alpha h} & \left(\frac{\omega_h}{\omega}\right)^2 + i2\zeta_h\left(\frac{\omega_h}{\omega}\right) - 1 - H_{hh} \end{bmatrix} \begin{Bmatrix} \alpha \\ \frac{h}{B} \end{Bmatrix} = 0 \qquad (5.45)$$

The coefficient matrix in (5.45) is divided by the common but unknown flutter frequency squared ω^2 to yield the flutter determinant:

$$\begin{vmatrix} \left(\frac{\omega_\alpha}{\omega}\right)^2 + i2\zeta_\alpha\left(\frac{\omega_\alpha}{\omega}\right) - 1 - A_{\alpha\alpha} & -A_{\alpha h} \\ -H_{\alpha h} & \left(\frac{\omega_h}{\omega}\right)^2 + i2\zeta_h\left(\frac{\omega_h}{\omega}\right) - 1 - H_{hh} \end{vmatrix} \qquad (5.46)$$

Where the $A_{\alpha h}$, $H_{\alpha h}$ terms are shorthand notation for the terms including the aerodynamic derivatives which are functions of the non-dimensional wind speed:

$$\begin{aligned} A_{\alpha\alpha} &= \frac{\rho B^4}{I}(A_3^* + iA_2^*) & H_{\alpha h} &= \frac{\rho B^2}{m}(H_3^* + iH_2^*) \\ A_{\alpha h} &= \frac{\rho B^4}{I}(A_4^* + iA_1^*) & H_{hh} &= \frac{\rho B^2}{m}(H_4^* + iH_1^*) \end{aligned} \qquad (5.47)$$

The next step is to multiply (5.45) by the ratio of the flutter frequency the bending frequency squared $(\omega/\omega_h)^2 = X^2$ and after introducing the eigenfrequency ratio $(\omega_\alpha/\omega_h)^2 = \gamma^2$ (5.46) is recast into the following form:

$$\begin{vmatrix} \gamma^2 + i2\zeta_\alpha X\gamma - X^2 - X^2 A_{\alpha\alpha} & -X^2 A_{\alpha h} \\ -X^2 H_{\alpha h} & 1 + i2\zeta_h X - X^2 - X^2 H_{hh} \end{vmatrix} \qquad (5.48)$$

Solution of (5.45) is obtained by setting the flutter determinant (5.46) equal to zero yielding a complex 4th order algebraic equation in X:

$$\begin{aligned} (\gamma^2 + i2\zeta_\alpha X\gamma - X^2 - X^2 A_{\alpha\alpha})(1 + i2\zeta_h X - X^2 - X^2 H_{hh}) \\ - X^2 A_{\alpha h} H_{\alpha h} = 0 \end{aligned} \qquad (5.49)$$

(5.49) can be expanded to yield a 4th order equation for the real part and a 3th order equation for the imaginary part, see Appendix C. Determination of the flutter wind speed and the flutter frequency proceeds graphically by plotting the real and imaginary root curves of (5.49) as function of the non-dimensional wind speed. The flutter point is obtained as the coordinates $(U/fB_c,\ X_c)$ of intersection point of the root curves. Having established the abscissa U/fB_c and the ordinate X_c of the intersection point, the flutter wind speed and the flutter frequency are obtained as:

$$U_c = \left(\frac{U}{fB}\right)_c X_c f_h B \tag{5.50}$$

$$f_c = X_c f_h \tag{5.51}$$

where $f_h = \omega_h / 2\pi$.

The above procedure is illustrated in Figure 5.8 applying the measured aerodynamic derivatives of Izmit deck section shown in Figure 5.4 and section mass properties and eigenfrequencies given in Table 5.1. Solution of the real and imaginary root curves is carried out by means of a commercially available numerical routine included in the PC based MathCad mathematical calculus environment.

m [kg/m]	I [kgm^2/m	f_h [Hz]	f_α [Hz]	B [m]	$\partial C_M/\partial\alpha_0$	$\partial C_L/\partial\alpha_0$
$21.09\cdot10^3$	$2.506\cdot10^6$	0.091	0.268	35.8	1.17	4.6

Table 5.1 Structral and aerodynamic properties of the Izmit Suspension Bridge.

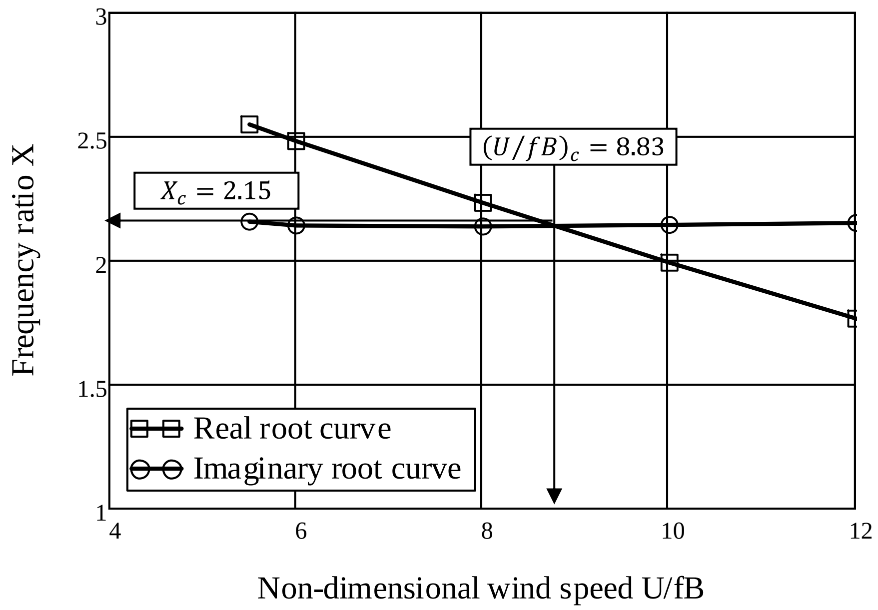

Figure 5.8 Determination of flutter wind speed and frequency from intersection of real and imaginary root curves according to the Theodorsens method. Izmit structural and aerodynamic properties.

Application of (5.50), (5.51) to the coordinates of the intersection point yields a critical wind speed $U_c = 61.9$ m/s and a flutter frequency $f = 0.182$ Hz in good agreement with Figure 5.6.

5.6 Solution of the flutter equations, the AMC method

The Theodorsen method becomes cumbersome in practical use for flutter calculations that includes more than two modes as the order of the algebraic root curves increases linearly with the number of modes included in the analysis. The AMC method (Air Material Command) [21] constitutes a procedure which is better suited for analyses involving multiple modes. A formal drawback is that it requires that the structural damping to be identical for all modes considered.

The basic assumption taken is taken is that the structural damping forces in the bridge is proportional to the displacement, but phase shifted 90 degrees. The flutter equations thus takes on the following form:

$$\left((1+ig)\omega_\alpha^2-\omega^2\right)\alpha=\frac{\rho B^4}{I}\omega^2\left[(A_4^*+iA_1^*)\frac{h}{B}+(A_3^*+iA_2^*)\alpha\right] \tag{5.52}$$

$$((1+ig)\omega_h^2-\omega^2)\frac{h}{B}=\frac{\rho B^2}{m}\omega^2\left[(H_4^*+iH_1^*)\frac{h}{B}+(H_3^*+iH_2^*)\alpha\right] \tag{5.53}$$

Where g is the apparent damping coefficient, which for low damping levels is equal to twice the structural viscous damping relative-to-critical g = 2ζ. Proceeding as before by arranging the flutter equations in matrix form, the flutter determinant is obtained as:

$$\begin{vmatrix}\left(\frac{\omega_\alpha}{\omega}\right)^2(1+ig)-1-A_{\alpha\alpha} & -A_{\alpha h}\\ -H_{\alpha h} & \left(\frac{\omega_h}{\omega}\right)^2(1+ig)-1-H_{hh}\end{vmatrix} \tag{5.54}$$

Multiplying the lower row by the frequency ratio squared $(\omega_\alpha/\omega_h)^2=\gamma^2$ and changing sign for all terms in the determinant allows (5.54) to be rewritten as follows:

$$\begin{vmatrix}1+A_{\alpha\alpha}-\left(\frac{\omega_\alpha}{\omega}\right)^2(1+ig) & A_{\alpha h}\\ \gamma^2H_{\alpha h} & \gamma^2(1+H_{hh})-\left(\frac{\omega_\alpha}{\omega}\right)^2(1+ig)\end{vmatrix} \tag{5.55}$$

Setting the flutter determinant equal to zero and substituting $\lambda=(\omega_\alpha/\omega)^2(1+ig)$ (5.55) is recognized as a complex eigenvalue problem (5.56) which may be solved by standard numerical methods.

$$\begin{vmatrix}1+A_{\alpha\alpha}-\lambda_1 & A_{\alpha h}\\ \gamma^2H_{\alpha h} & \gamma^2(1+H_{hh})-\lambda_2\end{vmatrix}=0 \tag{5.56}$$

Once the complex eigenvalues λ_1, λ_2 has been determined as functions of the non-dimensional wind speed, the apparent aerodynamic damping g, the flutter frequency ratio f/f_α and the corresponding wind speed U are obtained from the identity $\lambda=(\omega_\alpha/\omega)^2(1+ig)$ as follows:

$$g = \frac{Im(\lambda)}{Re(\lambda)} \tag{5.57}$$

$$\frac{f}{f_\alpha} = \frac{1}{\sqrt{Re(\lambda)}} \tag{5.58}$$

$$U = \left(\frac{U}{fB}\right)\frac{Bf_\alpha}{\sqrt{Re(\lambda)}} \tag{5.59}$$

Where $Re(\lambda)$, $Im(\lambda)$ are the real and imaginary parts of the eigenvalues determined as function of the non-dimensional wind speed. The analyses in the following examples are carried out by means of a commercially available numerical routine included in the PC based MathCad mathematical calculus environment.

Determination of the critical wind speed follows from balancing the apparent aerodynamic damping g with the structural damping $2\zeta_s$ of the bridge. This is conveniently done in graphical form as shown in Figure 5.9 (top).

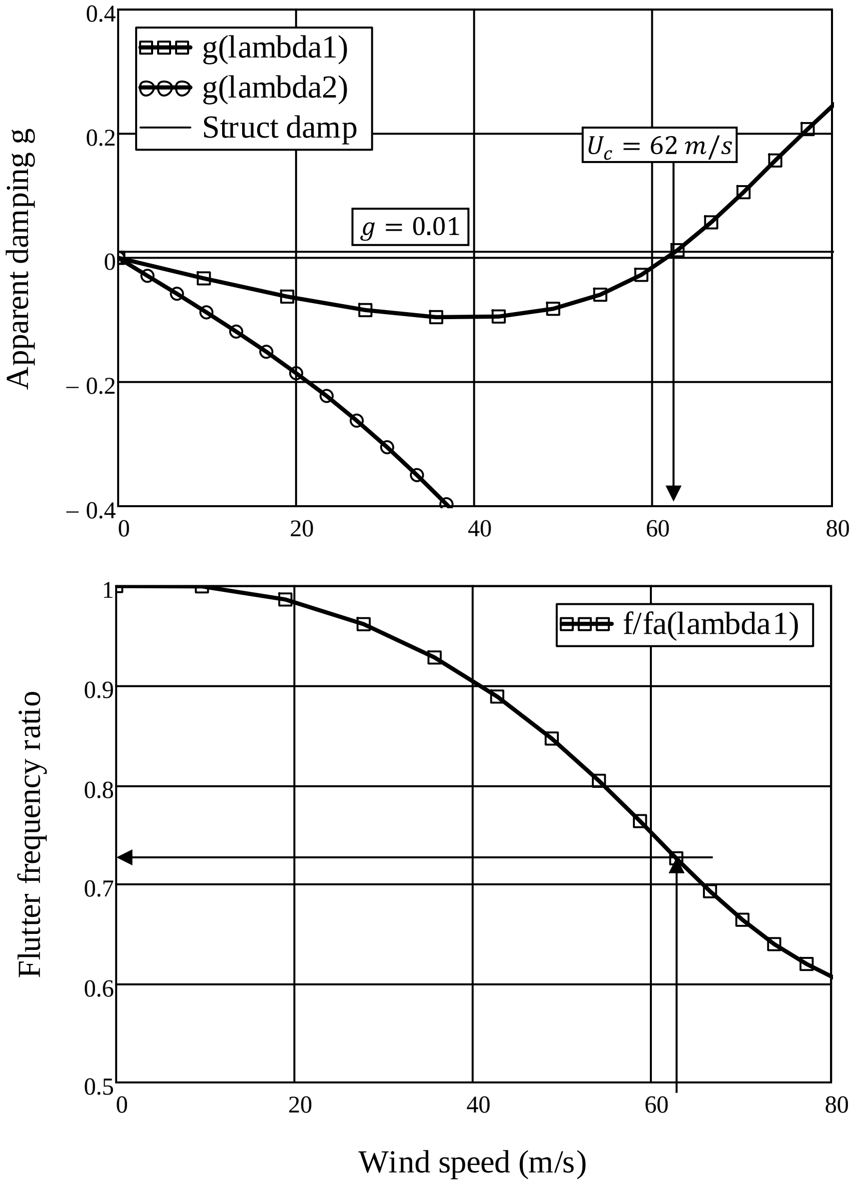

Figure 5.9 Determination of flutter wind speed from balancing of the apparent aerodynamic damping g to the structural damping $2\zeta_s$ (top) and determination of frequency ratio at flutter point according to the AMC method. Izmit structural and aerodynamic properties.

It is noted that one of the eigenvalue curves λ_1 defines an aerodynamic damping that starts out being negative at low wind speeds but tends towards positive values at higher wind speeds and balances the structural damping at 62 m/s. This defines the flutter wind speed of the bridge. The other eigenvalue curve λ_2 remains negative at all wind speeds and is not associated with aerodynamic instability. The flutter frequency is determined from Figure 5.9 (bottom) as the ordinate of the point of intersection between frequency ratio curve (5.58) and a vertical line at the critical wind speed. At $U = 62$ m/s the frequency ratio is obtained as $f/f_\alpha = 0.72$ or $f = 0.19$ Hz in reasonable agreement with the result of the Theodordsen method. Lastly it is noted that structural damping has little influence on the critical wind speed as U_c = 61 m/s is read off Figure 5.9 (top) for $g = 0$.

5.7 Measured or "flat plate" aerodynamic derivatives?

It is often stated that the critical wind speed of semi-streamlined bridge girders like the Izmit deck section is well predicted by the theoretical aerodynamic derivatives (5.33) – (5.40) either by applying the "flat plate" lift and moment slopes $\partial C_L/\partial\alpha = -2\pi$ and $\partial C_M/\partial\alpha = \pi/2$ or by introducing lift and moment slopes determined from static load tests of section models. These options are investigated in Figure 5.10 applying the AMC method.

The critical wind speed determined from the measured aerodynamic derivatives is approximately 62 m/s as mentioned above. Applying the theoretical aerodynamic derivatives with "flat plate" lift and moment slope yields a critical wind speed of 67 m/s slightly higher than experimental aerodynamic derivatives. Application of the measured static lift slopes $\partial C_L/\partial\alpha = -4.6$ and $\partial C_M/\partial\alpha = 1.17$, Table 5.1, yields a critical wind speed of 81 m/s approximately 30 % higher than obtained from experiment. The example thus supports the notion that "flat plate" theory is a reasonable approximation to the critical wind speed of semi-streamlined bridge girder sections likely to err on the non-conservative side.

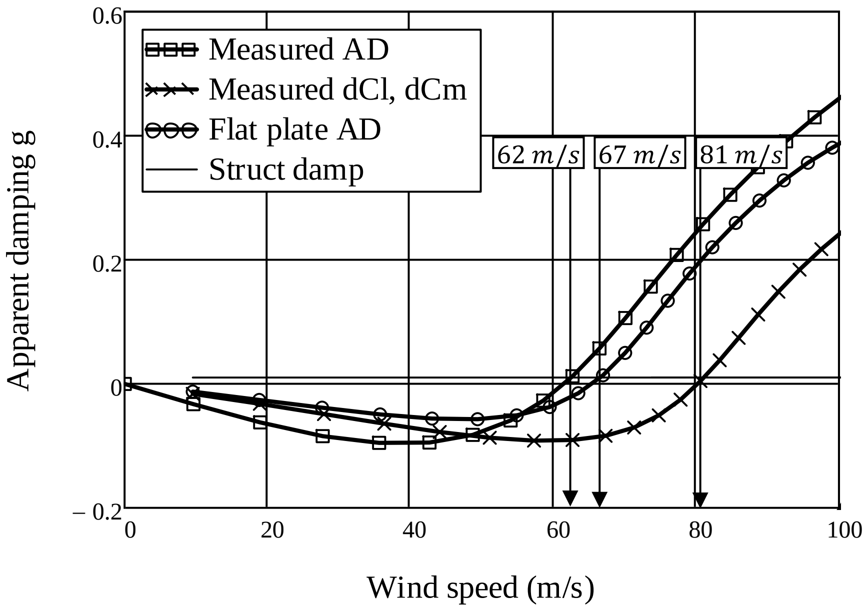

Figure 5.10 Critical wind speeds determined for the Izmit bridge section model applying measured and theoretical aerodynamic derivatives.

5.8 Selbergs formula, eigenfrequency ratio and static divergence

The success of the "flat plate" theory to predict the critical wind speed of semi-streamlined bridge sections prompted Selberg [6] to develop a simple formula for estimation of the critical wind of the "flat plate" bridge deck. The original formulation included the eigenfrequencies expressed in rad/s. Current formulations usually involves the eigenfrequencies in Hz [24].

$$U_c = 3.71 f_\alpha B \sqrt{\frac{Rm}{\rho B^3}\left(1 - \left(\frac{f_h}{f_\alpha}\right)^2\right)} \tag{5.60}$$

Where $R = \sqrt{I/m}$ is the radius of gyration of the bridge deck including the inertia of the main cables and the empirical constant 3.71 include the effect of the aerodynamic loads. Selberg did not detail the development of (5.60) in [6] but a clue to how the formula was conceived can be obtained from the following argument.

The equation of motion for the torsional mode (5.43) can be reformulated in a simplified form by neglecting structural damping and aerodynamic the derivatives associated with torsion damping and the vertical mode A_2^*, A_1^*, A_4^* and substituting the leading term of the "flat plate" value (5.39) for A_3^*:

$$(\omega_\alpha^2 - \omega^2)\alpha = \frac{\rho B^4}{I}\omega^2 \frac{1}{2K^2}\left[\frac{\pi}{2}F(K)\right]\alpha \tag{5.61}$$

Inserting $K = \omega B/U$, observing that $I = R^2 m = Rm\sqrt{I/m}$ and making the bold assumption that $\omega^2 = ½(\omega_\alpha^2 + \omega_h^2)$ (which is not unreasonable in light of Figure 5.7) allows (5.61) to be rearranged as:

$$U_c = \left[\sqrt{\frac{8\pi}{F(K)}\sqrt{\frac{I}{mB^2}}}\right] f_\alpha B \sqrt{\frac{Rm}{\rho B^3}\left(1 - \left(\frac{f_h}{f_\alpha}\right)^2\right)} \tag{5.62}$$

Selberg made his estimate of the empirical aerodynamics constant of 3.71 based on a long series of "flat plate" calculations for varying structural parameters representative of suspension bridges. The first term in the square brackets in (5.62) is the equivalent of Selbergs empirical constant. Taking the Izmit bridge section as a single example the non-dimensional frequency at flutter is obtained from Figure 5.8 as $K_c = 2\pi/8.83 = 0.71$. The first term in (5.62) assumes a value of 3.43 for $F(K_c) = 0.65$, Figure 5.3, giving some credibility to the above argument.

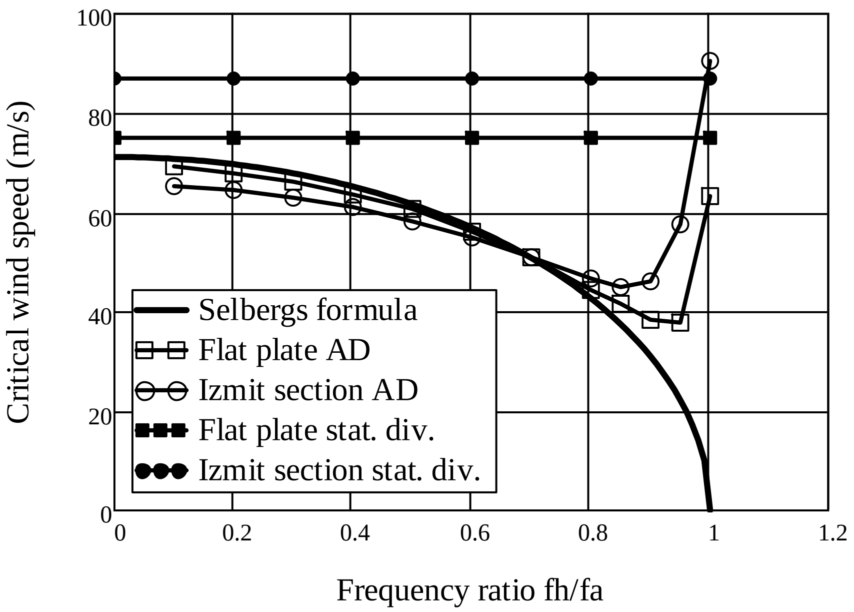

Figure 5.11 Critical wind speed predicted by the Selberg formula and from "flat plate" and experimental aerodynamic derivatives obtained for the Izmit deck section applying Izmit bridge structural properties.

Figure 5.11 presents a plot of the critical wind speed obtained by Selbergs formula (5.60) and by a two-degree-of-freedom flutter analysis. It is noted that Selbergs formula predicts that the critical wind speed approaches 0 when the eigenfrequency ratio f_h/f_α approaches unity. Critical wind speeds obtained from two-degree-of-freedom flutter calculations applying "flat plate" and experimental aerodynamic derivatives demonstrate a good agreement with the Selberg formula for frequency ratios less than 0.8, with the "flat plate" values yielding a slightly better agreement as to be expected. The critical wind speed according to Selbergs formula drops rapidly off at f_h/f_α ratios higher than 0.8 whereas the two-degree-of-freedom calculations display and increasing critical wind speed as f_h/f_α approaches unity.

The fact that the critical wind speed grows rapidly as the frequency ratio approaches unity has sparked off proposals to design "flutter free" suspension bridges for which the frequency ratio is kept very close to unity. While the idea cannot be dismissed from theoretical considerations another type of aerodynamic instability, static divergence, must also be accounted for. Static divergence marks a condition by which the twisting action of static aerodynamic moment exceeds the resisting capacity of the structural stiffness and thus makes the girder yield once the threshold wind speed is exceeded. The threshold wind speed for static divergence U_d can be obtained from (5.63) assuming that $\omega = 0$ and that A_3^* is replaced by its steady state value $A_3^* = \partial C_M/\partial\alpha$:

$$U_d = \omega_\alpha B \sqrt{\frac{I}{\rho B^4}\frac{2}{\partial C_M/\partial\alpha}} \tag{5.63}$$

The divergence wind speeds obtained for the Izmit deck section assuming either "flat plate" ($\partial C_M/\partial\alpha = \pi/2$) and measured moment slopes ($\partial C_M/\partial\alpha = 1.17$) are marked by horizontal lines in Figure 5.11. It is noted that static divergence becomes the governing factor for aerodynamic stability as the frequency ratio approaches unity.

5.9 The influence of mode shape

The structural and aeroelastic loads on a cable supported bridge is dependent on the amplitude of the motion of the bridge structure as is apparent from (5.43), (5.44). For real bridge structures the amplitudes will vary as a function of the span wise position, as given by the mode shapes of the bridge participating in the flutter motion. Flutter is driven by the torsion mode having the lowest frequency and will couple to the vertical modes of lower frequency but of similar symmetric or asymmetric form. To illustrate this concept the basic torsion and bending mode shapes of the Izmit suspension bridge as determined from Finite Element analysis are shown in Figure 5.12, Figure 5.13.

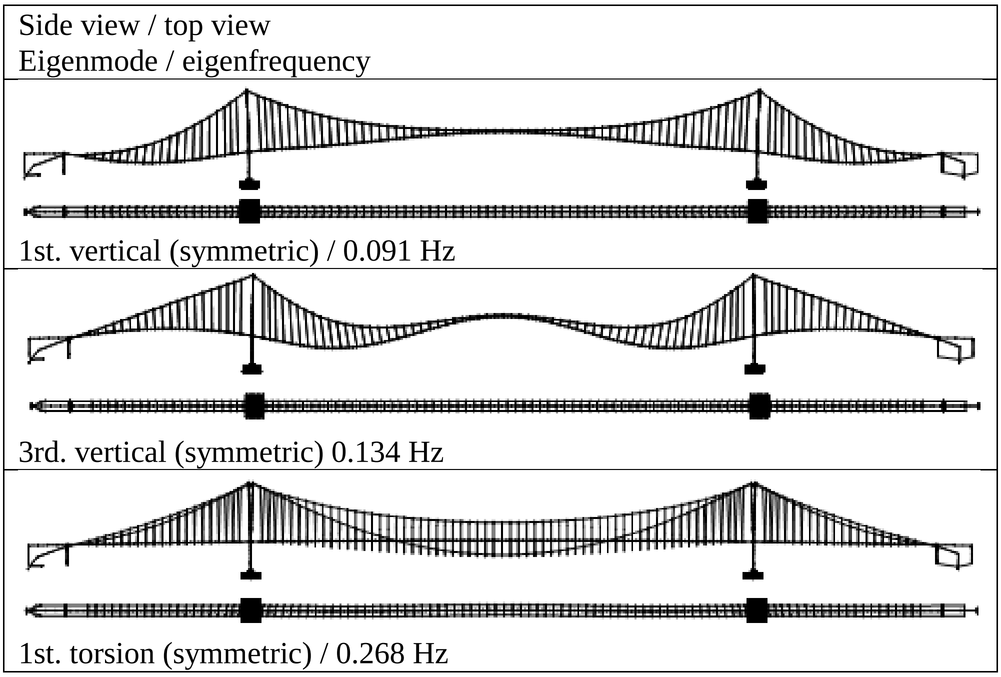

Figure 5.12 Symmetric eigenmodes of the Izmit suspension bridge determined by Finite Element analysis.

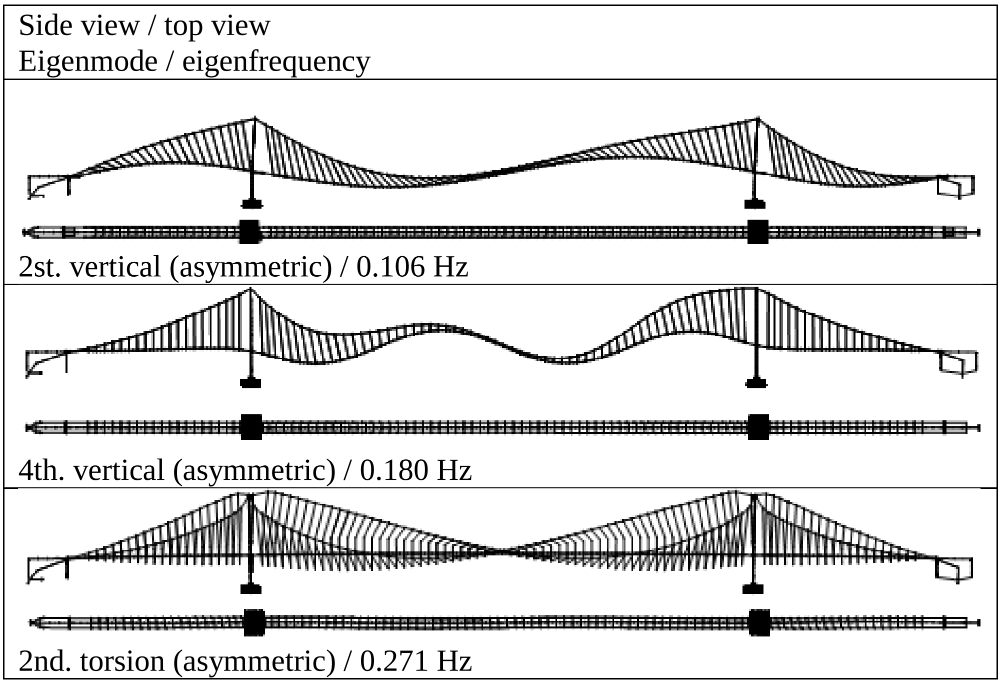

Figure 5.13 Asymmetric eigenmodes of the Izmit suspension bridge determined by Finite Element analysis.

The principle involved in combining the structural modes to the inertial and aeroelastic forces is well known form standard textbooks on structural dynamics and wind engineering such as Scanlan and Simiu [27] and will not be discussed in further detail. It can be demonstrated that the effect of mode shape is included in the $A_{\alpha\alpha}$, $A_{\alpha h}$, $H_{\alpha h}$, H_{hh} terms as follows:

$$
\begin{aligned}
A_{\alpha\alpha} &= \frac{\rho B^4}{I^*} C_{\alpha\alpha}(A_3^* + iA_2^*) \qquad & H_{\alpha h} &= \frac{\rho B^2}{m^*} C_{\alpha h}(H_3^* + iH_2^*) \\
A_{\alpha h} &= \frac{\rho B^4}{I^*} C_{\alpha h}(A_4^* + iA_1^*) \qquad & H_{hh} &= \frac{\rho B^2}{m^*} C_{hh}(H_4^* + iH_1^*)
\end{aligned}
\tag{5.64}
$$

Where the generalized masses / unit span length and mode shape coefficients are evaluated as integrals of the mode shapes $\alpha(s)$, $h(s)$ over span length L.

$$
\begin{aligned}
I^* &= \frac{1}{L}\int_0^L I(s)\alpha(s)^2 ds \qquad & C_{\alpha\alpha} &= \frac{1}{L}\int_0^L \alpha(s)^2 ds \qquad & C_{\alpha\alpha} &= \frac{1}{L}\int_0^L \alpha(s)^2 ds \\
m^* &= \frac{1}{L}\int_0^L m(s)h(s)^2 ds \qquad & C_{\alpha h} &= \frac{1}{L}\int_0^L \alpha(s)h(s) ds \qquad & C_{h\alpha} &= C_{\alpha h}
\end{aligned}
\tag{5.65}
$$

From (5.64) it is noted that for purely sinusoidal mode shapes $\alpha(s) = \sin(\pi s/L)$, $h(s) = \sin(\pi s/L)$ and for constant mass properties along the span, the aerodynamic coefficients (5.64) resumes their section model properties.

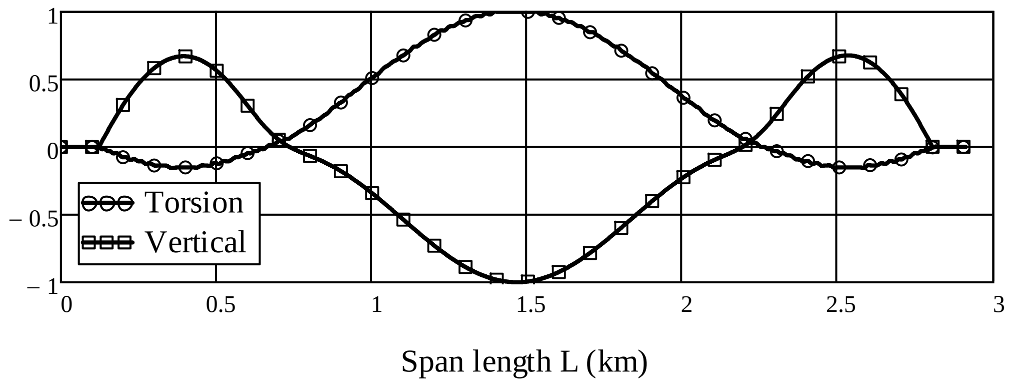

Figure 5.14 Basic symmetric torsion and vertical bending mode shapes for the Izmit suspension bridge.

The modal masses / unit length and mode shape coefficients evaluated according to (5.65) for the Izmit bridge are listed in Table 5.2. The corresponding critical wind speed for the bridge mode shapes and the section having unit mode shape are shown in Figure 5.15. It is noted that critical wind speed of the bridge is 66 m/s i.e. slightly above 62 m/s found for the unit mode shape case.

m^* [kg/m]	I^* [kgm^2/m	$C_{\alpha\alpha}$	C_{hh}	$C_{\alpha h}$
$6.09 \cdot 10^3$	$0.619 \cdot 10^6$	0.247	0.289	0.237

Table 5.2 Modal masses and mode shape coefficients obtained for the torsion and bending mode shapes displayed in Figure 5.14.

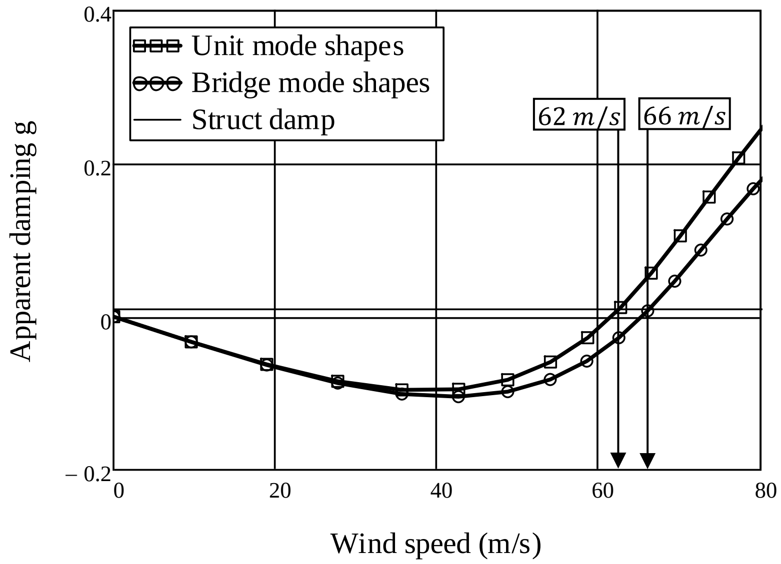

Figure 5.15 Determination of critical wind speed for the Izmit bridge section and bridge based on the basic symmetric modes show in Figure 5.14.

6. Three-degree-of-freedom multimode flutter analysis

During the 1980'ies Scanlan and co-workers expanded the two-degree-of-freedom theory to include the horizontal (along wind) degree-of-freedom expressed in terms of the P^* derivatives, Jones et al. [26]. While the inclusion of the third degree of freedom was meant to make flutter predictions more accurate, it complicates wind tunnel testing considerably by increasing the number of required derivatives from 8 to 18. Despite the theoretical advantage of including the horizontal aerodynamic effects in flutter predictions for bridges the adequacy has to the authors knowledge only been published for a single practical design application. Miyata [11] reports that in case of the Akashi-Kaikyo Bridge inclusion of the horizontal P^* derivatives was required in order to establish agreement between the critical wind speed obtained from flutter analyses and from full bridge model tests. Probably more important, the effect of the horizontal aerodynamic derivatives was to secure that flutter instability occurred in agreement with the 1/100 scale full aeroelastic model. Flutter was not predicted from the analysis when the horizontal aerodynamic derivatives were omitted from the analysis.

The author´s company is carrying out aerodynamic analyses of long span cable-stay and suspension bridges on a regular basis and the apparent importance of the horizontal aerodynamic derivatives has been an ongoing concern. The effect of the horizontal aerodynamic derivatives has been investigated for three cases involving a cable-stayed bridge of 1088 m main span and two suspension bridges of 1550 m and 3300 m main span, the latter being a tri-girder deck structure with large wind screens generating considerable along-wind drag loading. The flutter analyses of the three bridges mentioned above is discussed in the following with the objective of clarifying the relative importance of the horizontal aerodynamic derivatives.

6.1 Three-degree-of-freedom aeroelastic forces

The key assumption in three-degree-of-fredom flutter analyses is that the aeroelastic drag force D_{ae} may be expressed in a similar format as the aeroelastic lift L_{ae} and moment M_{ae} (5.29), (5.30). The complete set of equations for the aeroelastic forces on the deck in small amplitude oscillatory motion then becomes:

$$\frac{L_{ae}}{\rho U^2 B} = K^2 \left[(H_4^* + iH_1^*)\frac{h}{B} + (H_3^* + iH_2^*)\alpha + (H_6^* + iH_5^*)\frac{p}{B} \right] \tag{6.1}$$

$$\frac{D_{ae}}{\rho U^2 B} = K^2 \left[(P_6^* + iP_5^*)\frac{h}{B} + (P_3^* + iP_2^*)\alpha + (P_4^* + iP_1^*)\frac{p}{B} \right] \tag{6.2}$$

$$\frac{M_{ae}}{\rho U^2 B^2} = K^2 \left[(A_4^* + iA_1^*)\frac{h}{B} + (A_3^* + iA_2^*)\alpha + (A_6^* + iA_5^*)\frac{p}{B} \right] \tag{6.3}$$

Where α, h and p is the torsion, vertical and horizontal displacement respectively.

The decrease of structural stiffness due to the wind loading is the primary mechanism for flutter as discussed in section 5.8. However, the cross coupling between the vertical and twisting degrees of freedom, i.e. the aerodynamic moment caused by vertical movement or aerodynamic vertical lift caused by twisting motion, is necessary to secure prediction of the correct critical wind speed as discussed in the previous sections. Hence the coupling between the basic twisting and vertical modes and defines the flutter wind speed of a given bridge to a first approximation. The cross coupling between the horizontal and the vertical and twisting degrees of freedom postulated in (6.1) – (6.3) may be speculated to affect the flutter dynamics in two ways:

1) Twisting motion of a vertically or horizontally curved bridge girder (i.e. due to mean wind loading) will have a horizontal component. The structurally coupled horizontal motion will create drag forces which in turn will influence the flutter dynamics.

2) Aerodynamic coupling between vertical and twisting motions will cause horizontal modes to be excited which in turn will influence the flutter dynamics.

Multimode flutter analysis based on structural modal analysis has been a reoccurring topic at wind engineering conferences for the past three decades. A good state-of-the-art review is presented in [26]. A more recent paper [24] discusses multimode flutter analysis applied to a long single span suspension bridge built recently in Norway. One of the conclusions of this work is that the flutter wind speed is reasonably well predicted if the flutter analysis is based on three structural modes only being the lowest torsion mode which happened to be the first symmetric torsion and the lowest two symmetrical vertical bending modes. Inclusion of a third bending mode only changes the flutter wind speed by only 0.3%. Based on this result and for the sake of simplicity, the following discussion will involve four modes: The first symmetric or asymmetric torsion mode depending on which mode has the lowest eigenfrequency, the corresponding two lowest vertical modes (symmetric or antisymmetric to match the torsion mode) and the lowest horizontal mode to match the torsion or alternatively horizontal component of the lowest torsion mode.

The flutter determinant for the 4 mode case is assembled similar to (5.55) adopting the structural damping formulation applied in the AMC method:

$$\begin{vmatrix} 1 + A_{\alpha\alpha} - \lambda_1 & A_{\alpha h1} & A_{\alpha h2} & A_{\alpha p} \\ H_{h1\alpha}\left(\frac{\omega_\alpha}{\omega_{h1}}\right)^2 & (1 + H_{h1h1})\left(\frac{\omega_\alpha}{\omega_{h1}}\right)^2 - \lambda_2 & H_{h1h2}\left(\frac{\omega_\alpha}{\omega_{h1}}\right)^2 & H_{h1p}\left(\frac{\omega_\alpha}{\omega_{h1}}\right)^2 \\ H_{h2\alpha}\left(\frac{\omega_\alpha}{\omega_{h2}}\right)^2 & H_{h2h1}\left(\frac{\omega_\alpha}{\omega_{h2}}\right)^2 & (1 + H_{h2h2})\left(\frac{\omega_\alpha}{\omega_{h1}}\right)^2 - \lambda_3 & H_{h2p}\left(\frac{\omega_\alpha}{\omega_{h1}}\right)^2 \\ P_{p\alpha}\left(\frac{\omega_\alpha}{\omega_p}\right)^2 & P_{ph1}\left(\frac{\omega_\alpha}{\omega_p}\right)^2 & P_{ph2}\left(\frac{\omega_\alpha}{\omega_p}\right)^2 & (1 + P_{pp})\left(\frac{\omega_\alpha}{\omega_p}\right)^2 - \lambda_4 \end{vmatrix} = 0 \tag{6.4}$$

With each of the elements of the flutter determinant are defined similarly to (5.64):
1st row, torsion:

$$A_{\alpha\alpha} = \frac{\rho B^4}{I^*} C_{\alpha\alpha}(A_3^* + iA_2^*) \quad A_{\alpha h1} = \frac{\rho B^4}{I^*} C_{\alpha h1}(A_4^* + iA_1^*) \quad A_{\alpha h1} = \frac{\rho B^4}{I^*} C_{\alpha h2}(A_4^* + iA_1^*) \quad A_{\alpha p} = \frac{\rho B^4}{I^*} C_{\alpha p}(A_6^* + iA_5^*)$$

2nd row, vertical bending:

$$H_{h1\alpha} = \frac{\rho B^2}{m_{h1}^*} C_{h1\alpha}(H_3^* + iA_2^*) \quad H_{h1h1} = \frac{\rho B^2}{m_{h1}^*} C_{h1h1}(H_4^* + iH_1^*) \quad H_{h1h2} = \frac{\rho B^2}{m_{h1}^*} C_{h1h2}(H_4^* + iH_1^*) \quad H_{h1p} = \frac{\rho B^2}{m_{h1}^*} C_{h1p}(H_6^* + iH_5^*)$$

3rd row, vertical bending:

$$H_{h2\alpha} = \frac{\rho B^2}{m_{h2}^*} C_{h2\alpha}(H_3^* + iA_2^*) \quad H_{h2h1} = \frac{\rho B^2}{m_{h2}^*} C_{h2h1}(H_4^* + iH_1^*) \quad H_{h2h2} = \frac{\rho B^2}{m_{h2}^*} C_{h2h2}(H_4^* + iH_1^*) \quad H_{h2p} = \frac{\rho B^2}{m_{h2}^*} C_{h2p}(H_6^* + iH_5^*)$$

4th row, horizontal bending:

$$P_{p\alpha} = \frac{\rho B^2}{m_p^*} C_{p\alpha}(P_3^* + iP_2^*) \quad P_{ph1} = \frac{\rho B^2}{m_p^*} C_{ph1}(P_6^* + iP_5^*) \quad P_{ph2} = \frac{\rho B^2}{m_p^*} C_{ph2}(P_6^* + iP_5^*) \quad P_{pp} = \frac{\rho B^2}{m_p^*} C_{pp}(P_4^* + iP_1^*)$$

The calculation of modal masses and mode shape coefficients is straight forward following the model set out by (5.65) and will not be detailed further.

6.2 Measurement of flutter derivatives

Flutter derivatives are traditionally measured in a wind tunnel using a spring mounted section model of the bridge deck under investigation. This free oscillation technique originates from the Scanlan and Tomko 1971 landmark paper on bridge deck flutter [8]. In the free oscillation method decay traces of the deck section model are measured following either an impulsive displacement or random excitation by turbulence. The aerodynamic derivatives are then inferred from either the damping or the frequency shifts measured relative to a situation with no air flow in the wind tunnel. While the free oscillation technique is experimentally simple it becomes increasingly inaccurate as the test conditions approaches the flutter point mainly because only a few oscillation cycles are available for making the required analysis. This point becomes particularly critical for extraction of the horizontal derivatives as responses in this degree of freedom are observed to be small compared to the vertical and torsional degrees of freedom. The inherent accuracy of the free oscillation technique is often sought compensated for by repeating the individual sub-tests a large number of times.

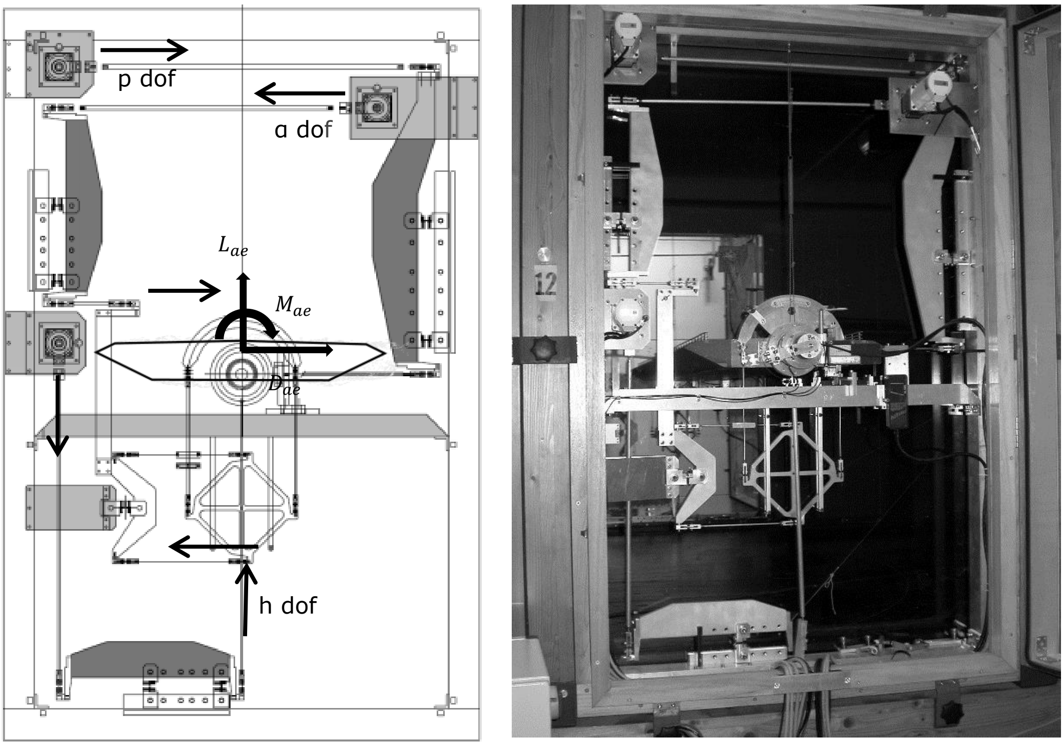

Figure 6.1 Schematic view of the three-degree-of-freedom forced oscillation apparatus (left). Photo of the H9.1 deck section mounted in the forced oscillation apparatus in the Force Technology wind tunnel (right).

A much more accurate experimental method is the forced oscillation technique by which the aerodynamic derivatives are obtained directly as transfer functions between imposed oscillatory motions and resulting measured aerodynamic forces. The drawback is that the experimental apparatus is much more complicated than what is called for when using the free oscillation technique. The wind tunnel set-up must be capable of moving the deck section model in accurate horizontal, vertical and twisting motions while the resulting aerodynamic forces are measured simultaneously. FORCE Technology, Copenhagen owns and operates a 2.2 m x 1.7 m wind tunnel with a forced oscillation apparatus, Figure 6.1, Larsen et. al. [28]. This set-up was applied for obtaining the three sets of aerodynamic derivatives shown in Appendix D and applied in the analyses discussed in the following. It is noted that the important aerodynamic derivatives H_1^*, H_3^*, A_2^*, A_3^*, are almost identical for the two mono box deck sections but markedly different for the tri-box deck of the Messina Bridge.

For the discussion in the previous sections, the Izmit bridge aerodynamic derivatives were expressed as continuous functions of the non-dimensional wind speed by means of curve fitted polynomials. When applied in the flutter analysis this process allows the apparent damping to be estimated at close spaced points as function of wind speed. For the analysis in the following sections, the aerodynamic derivatives are introduced at discrete points in the analysis corresponding to the measurement points in the wind tunnel tests. The critical wind speed is then determined by linear interpolation between the two points of the apparent damping level closest to and at either side of the anticipated structural damping level.

6.3 The SuTong cable-stayed bridge

The cable-stayed Finite Element model represents the 1088 m main span SuTong Bridge crossing the Yangtze River in China. The bridge carries a 6 lane highway on a 41.0 m wide and 4.0 m deep steel box girder of trapezoidal cross section. The bridge girder is supported by edge anchored stay cables arranged in 8 fans, 4 radiating from each pylon.

The three degree of freedom flutter derivatives were never measured for the design work of the SuTong Bridge, hence the present analysis uses aerodynamic derivatives for a somewhat similar bridge deck cross section designated H9.1, Figure 6.3. The flutter derivatives were measured for the H9.1 section as part of the design and verification of the wind tunnel set-up discussed in the previous section. With an over-all width of 31.0 m and a depth of 4.4 m the H9.1 section is slightly more bluff than the SuTong deck section with an over-all deck width of 41.0 m and a depth of 4.0 m. However, with the steady state lift, drag and moment slopes being almost identical for the two deck sections it is expected that the flutter derivatives of the H9.1 section will be fairly representative of the SuTong Bridge.

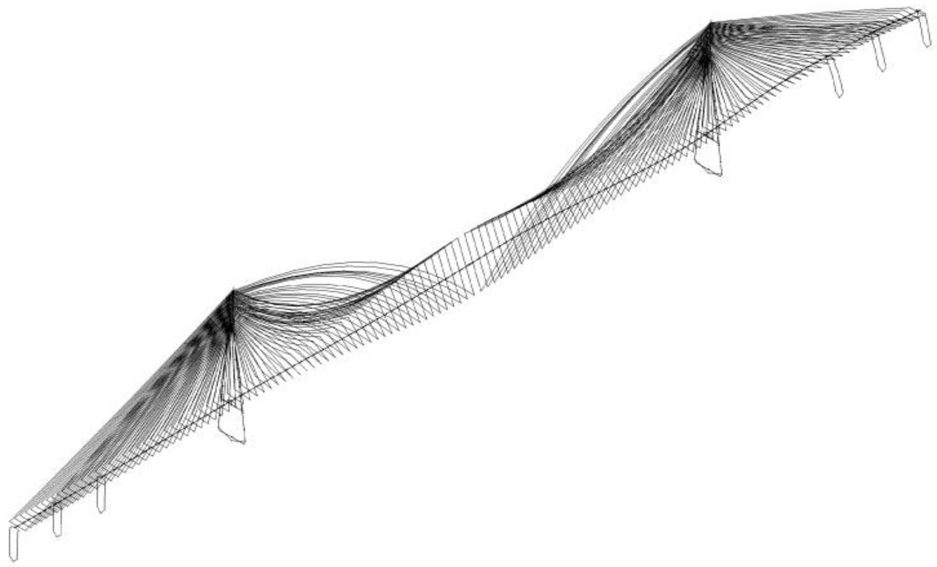

Figure 6.2 Isometric view of the FEM model of the SuTong Bridge displaying the first torsion mode (symmetric).

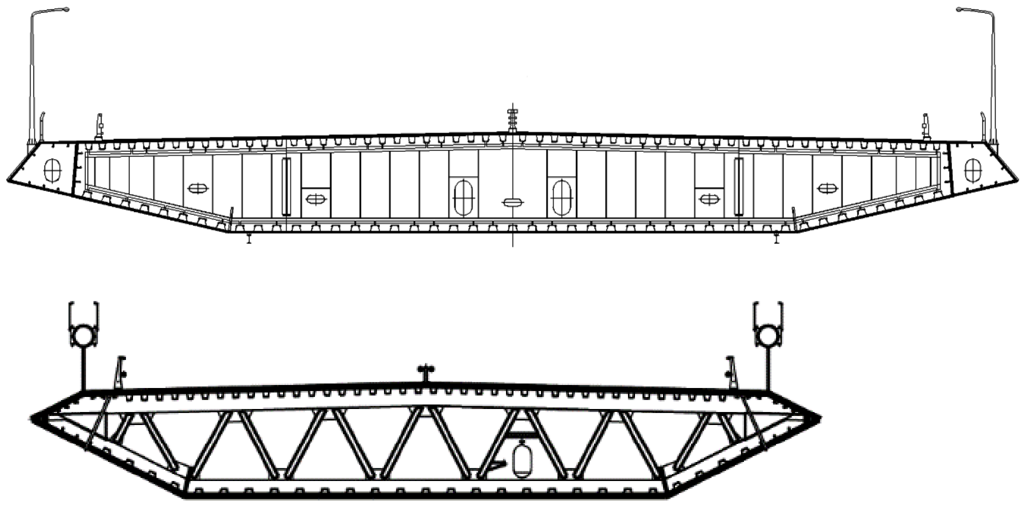

Figure 6.3 Comparison of the SuTong deck section (top) to the H9.1 deck section (bottom).

From the isometric view of the FE model representation of the lowest torsion mode of the SuTong Bridge, Figure 6.2, it is noted, that the lowest torsion mode is symmetric about mid-span but it may also be recognized that the torsion mode has a pronounced horizontal component brought about by structural coupling. This fact is highlighted in Figure 6.4 which shows the modes ($h1, h2, \alpha16, p16$) corresponding to the deflection of the centre line of the bridge deck considered in the present analysis. Dynamic properties such as inertia and eigenfrequencies of relevance to the SuTong Bridge are given in Table 6.1.

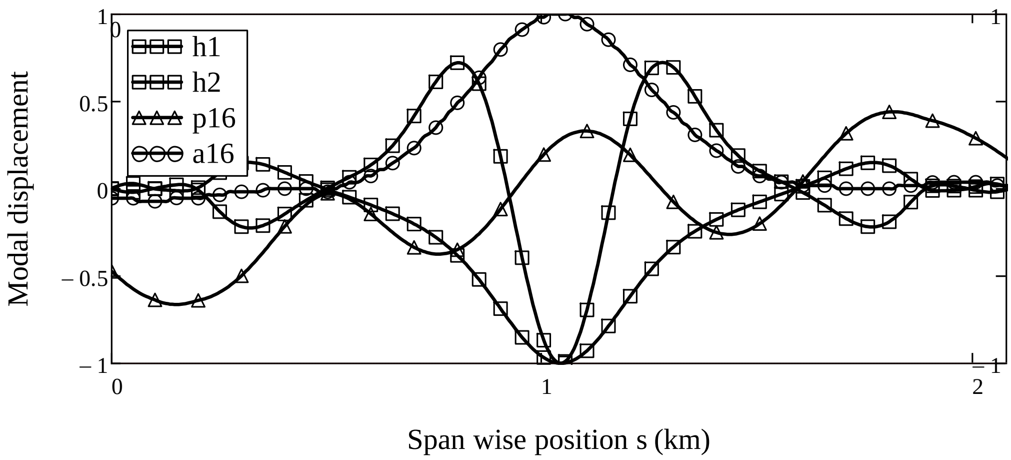

Figure 6.4 Vertical $h1, h2$, horizontal $p16$ and torsion mode shapes $\alpha16$ considered for the SuTong Bridge flutter analysis.

The result of the flutter analysis with and without the $P^*_{1..6}$ aerodynamic derivatives is shown in Figure 6.5. It is noted that the critical wind speed corresponding to g = 0.01 is virtually unaffected by the horizontal aerodynamic derivatives. Zooming in on the intersection points with the horizontal g = 0.01 line it is found that U_c = 112 m/s in case the horizontal aerodynamic derivatives are included and U_c = 113 m/s if the horizontal aerodynamic derivatives are omitted. Assuming unity mode shapes for $h1$, $\alpha16$ (section model) a critical wind speed U_c = 111 m/s is obtained.

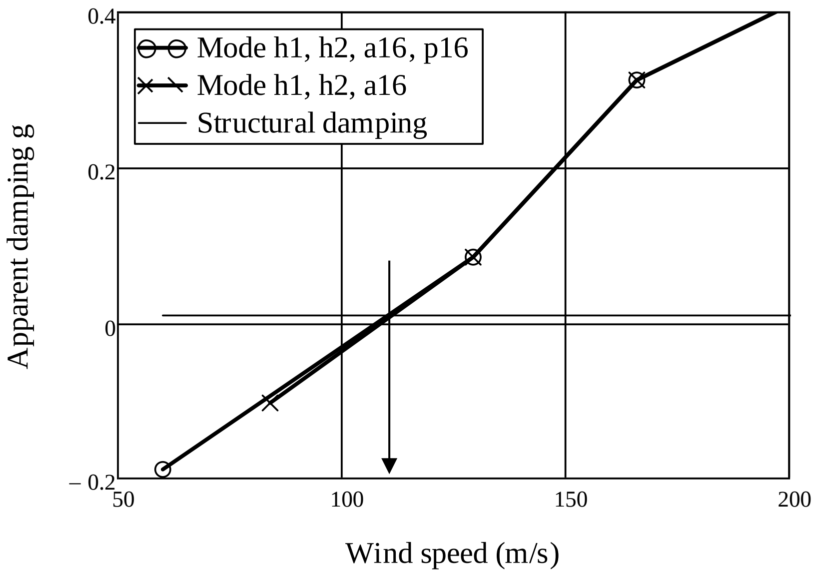

Figure 6.5 Result of the 4 mode flutter analysis for the SuTong Bridge with and without the horizontal aerodynamic derivatives.

Mode	Eigenfrequency	Inertia
1. Torsion (α16)	f_{α} = 0.506 Hz	I = $2.98 \cdot 10^6$ kgm^2/m
1. Vertical (h1)	f_{h1} = 0.177 Hz	m = $21.7 \cdot 10^3$ kg/m
2. Vertical (h2)	f_{h2} = 0.307 Hz	m = $21.7 \cdot 10^3$ kg/m
1. Horizontal (p16)	f_p = 0.506 Hz	m = $21.7 \cdot 10^3$ kg/m

Table 6.1 SuTong Bridge dynamic properties applied in the flutter analysis.

6.4 The Izmit suspension bridge

The first suspension bridge FE model considered represents the 1550 m main span Izmit Bridge currently under construction in Turkey. This bridge, which has been used as an example when discussing two-degree-of-freedom analysis, carries a 6 lane highway on a trapezoidal box girder. Two walkways are cantilevered at the apex points of the 35.8 m wide and 4.75 m deep section, Figure 5.4. The bridge girder is carried by two classical wire suspension cables arranged over the attachment points of the cantilevered walkways. An isometric view of the FE model representation of the lowest torsion mode of the Izmit bridge is shown in Figure 6.6. It is noted that the mode is symmetric about mid-span and it may also be recognized that the torsion mode $\alpha 21$ has very little horizontal movement $p21$ due to structural coupling as is highlighted in Figure 6.7.

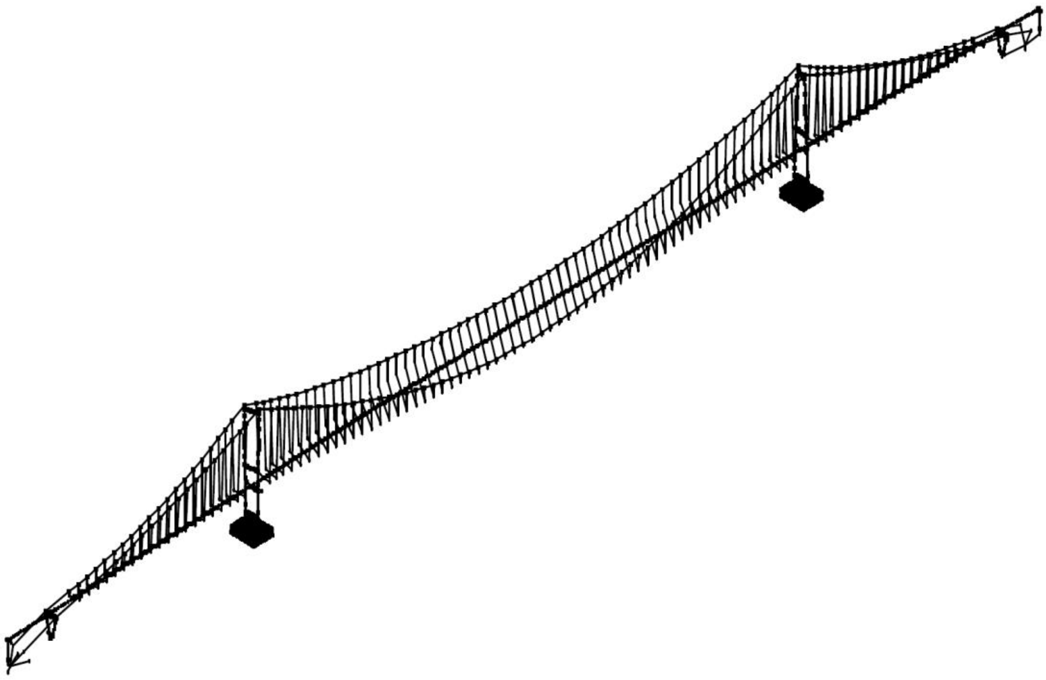

Figure 6.6 Isometric view of the FEM model of the Izmit bridge displaying the first torsion mode (symmetric).

The FE model is loaded by a horizontal static load corresponding to a mean wind speed of 40 m/s at bridge girder level yielding a horizontal mean deck deflection of approximately 2.5 m at mid span. The participating modes in the analysis are shown in Figure 6.7. Dynamic properties such as inertia and eigenfrequencies of relevance to the flutter analysis are given in Table 6.2.

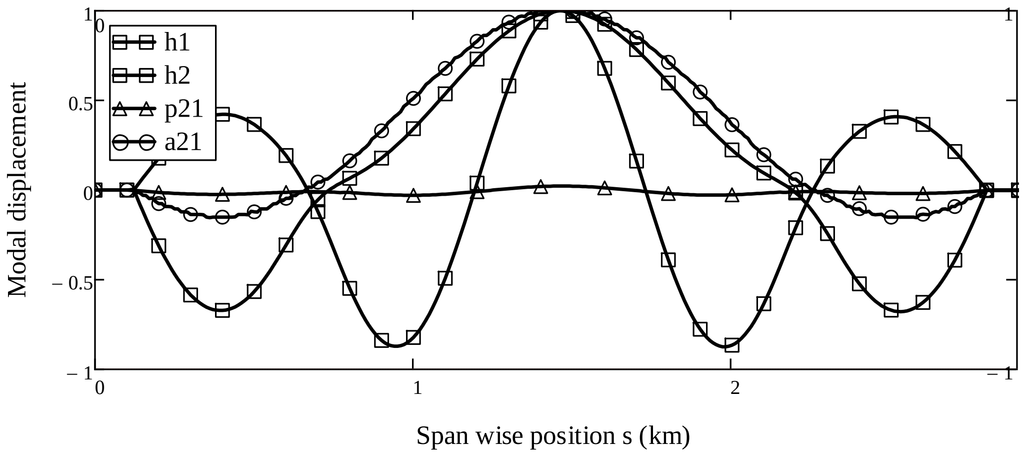

Figure 6.7 Vertical $h1, h2$, horizontal $p21$ and torsion mode shapes $\alpha21$ considered for the Izmit Bridge flutter analysis. Mean wind deflection at mid span = 2.5 m.

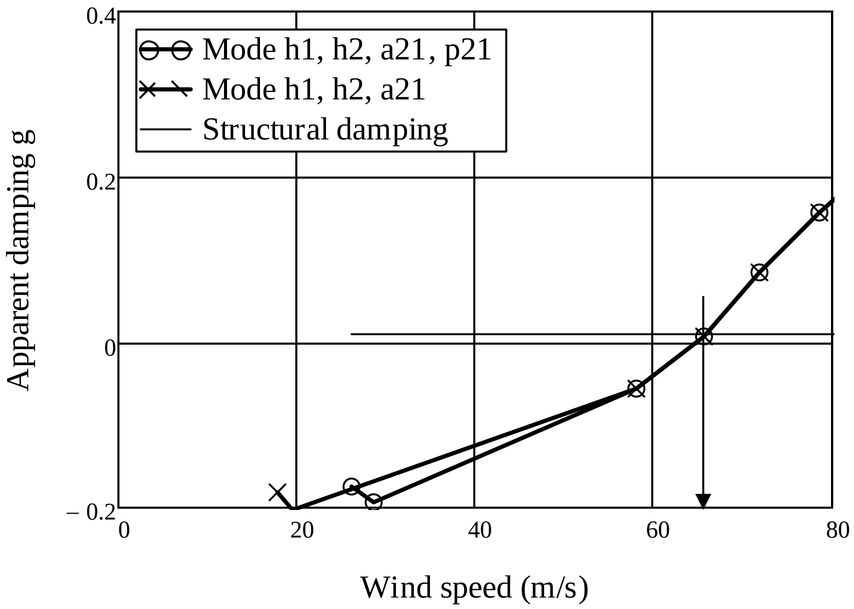

Figure 6.8 Result of the 4 mode flutter analysis for the Izmit Bridge with and without the horizontal aerodynamic derivatives. Mean wind deflection at mid span = 2.5 m.

The result of the flutter analysis is shown in Figure 6.8. It is noted that the critical wind speed corresponding to g = 0.01 is U_c = 66 m/s irrespective of the horizontal aerodynamic derivatives ($P^*_{1..6}$) are included or not. This is not surprising in view of the very small horizontal deflection brought about by the structural coupling to the torsion mode. Full aeroelastic testes of a 1:220 scale model of this bridge carried out at the University of Milan yielded a critical wind speed U_c= 65 m/s in surprisingly good agreement with the flutter predictions.

The experience gained from the flutter analysis and the full aeroelastic model wind tunnel tests of the Akashi-Kaikyo Bridge referred to in section 6.1 indicates that the torsion/horizontal coupling due to large mean wind deflections may yield a significant decrease of the flutter wind speed relative to the undeflected bridge. In order to investigate this scenario the mean wind deflection of the finite element model was increased to 36 m corresponding to approximately one deck width. The resulting mode shapes and the flutter calculation are shown in Figure 6.9, Figure 6.10 below.

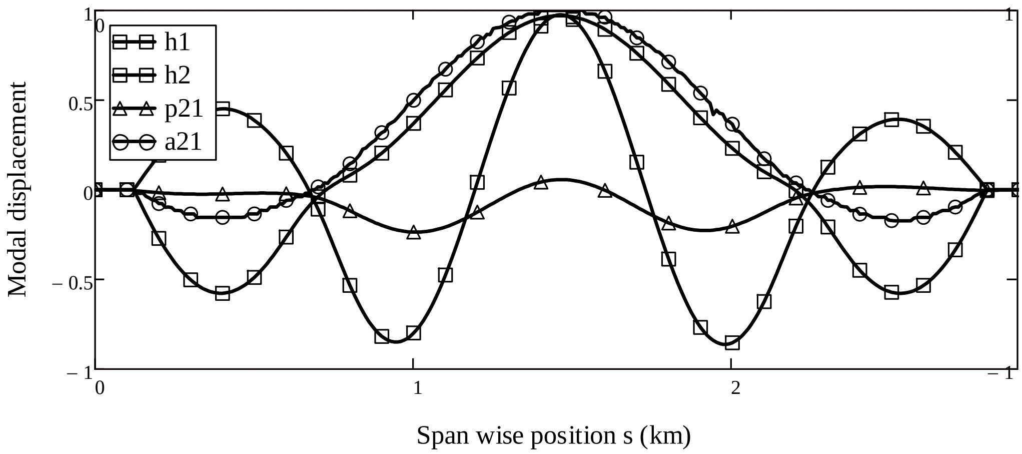

Figure 6.9 Vertical $h1, h2$, horizontal $p21$ and torsion mode shapes $\alpha21$ considered for the Izmit Bridge flutter analysis. Mean wind deflection at mid span = 36.0 m.

Comparison of the mode shapes in Figure 6.7 and Figure 6.9 reveals that the increased horizontal static deflection gives rise to an increased amplitude of the horizontal mode shape. Also the torsion/horizontal eigenfrequency increases slightly from f_α = 0.258 Hz to f_α = 0.271 Hz. However, the critical wind speed is not significantly affected yielding a critical wind speed U_c = 64 m/s whether or not the horizontal aerodynamic derivatives are included.

Mode	Eigenfrequency	Inertia
1. Torsion (α21)	f_α = 0.258 Hz	I = $2.51 \cdot 10^6$ kgm^2/m
1. Vertical (h1)	f_{h1} = 0.091 Hz	m = $21.09 \cdot 10^3$ kg/m
2. Vertical (h2)	f_{h2} = 0.136 Hz	m = $21.09 \cdot 10^3$ kg/m
1. Horizontal (p21)	f_p = 0.258 Hz	m = $21.09 \cdot 10^3$ kg/m

Table 6.2 Izmit bridge dynamic properties applied in the flutter analysis.

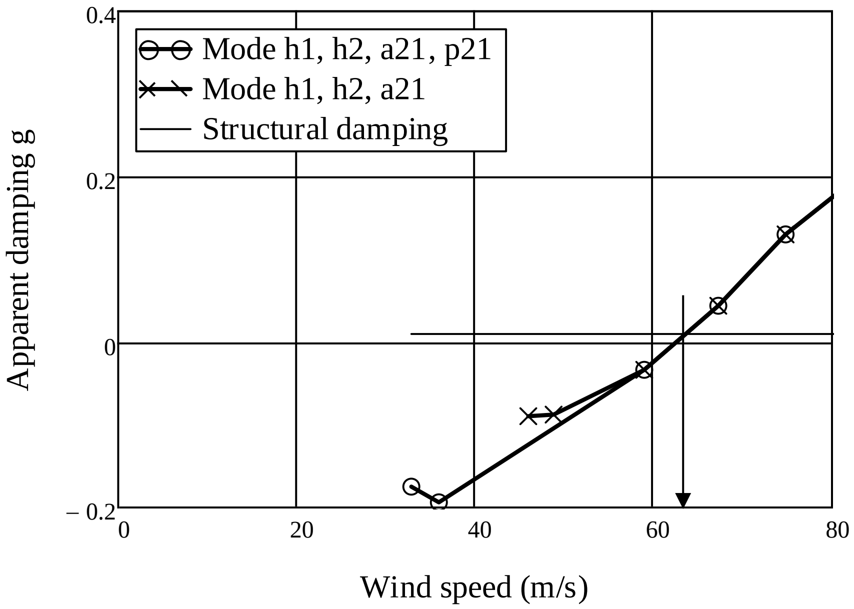

Figure 6.10 Result of the 4 mode flutter analysis for the Izmit Bridge with and without the horizontal aerodynamic derivatives. Mean wind deflection at mid span = 36.0 m.

6.5 The Messina suspension bridge

The second suspension bridge FE model considered represents the 3300 m main span Messina Bridge designed for crossing the Messina Strait, linking Sicily to the Italian main land. The bridge carries 6 lanes of highway traffic and two railway tracks as well as cantilevered maintenance paths. The bridge deck is unique in that it is split in three separate box girder structures separated by air gaps but held structurally together by heavy cross beams. A design developed for enhancement of the aerodynamic stability. The bridge girder is supported by two twinned classical wire suspension cables arranged over the attachment points of the cantilevered maintenance paths. The deck cross section is a total of 60.0 m wide and the individual girders have a depth of 2.5 m, Figure 6.11.

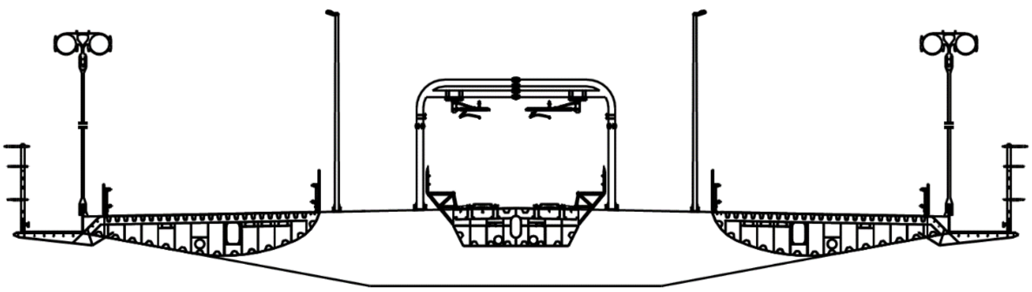

Figure 6.11 Deck cross section of the planned Messina Straits suspension bridge.

An isometric view of the FE model representation of the lowest torsion mode of the Messina Bridge is shown in Figure 6.12. It is noted that the torsion mode now is asymmetric about mid-span contrary to that of the Izmit Bridge but little horizontal girder movement due to structural coupling is noted, Figure 6.13 as in the case of the Izmit Bridge. Dynamic properties such as inertia and eigenfrequencies of relevance to the analysis are given in Table 6.3.

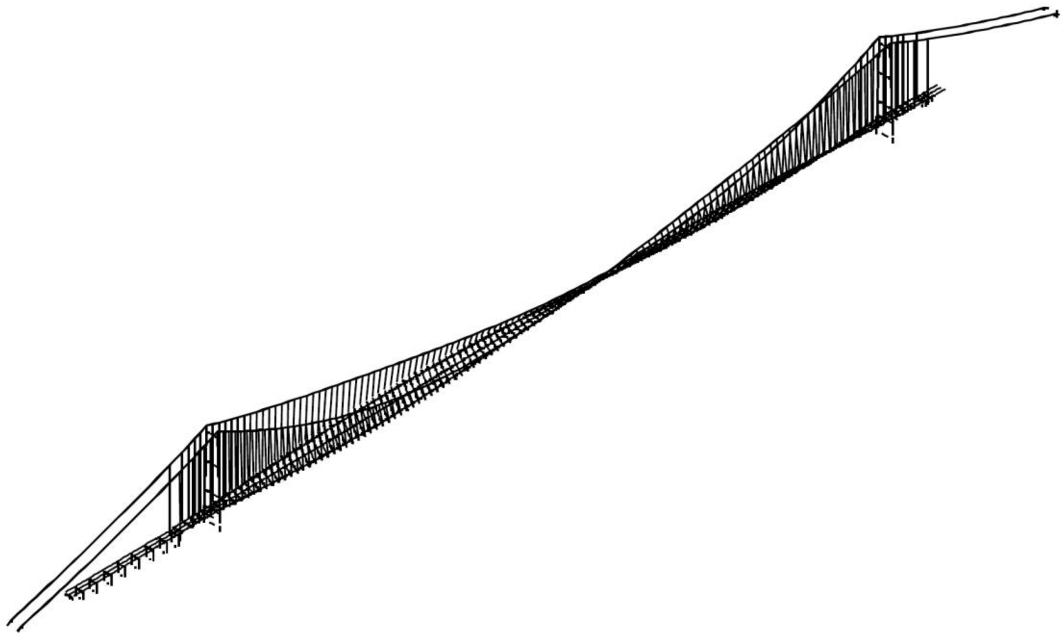

Figure 6.12 Isometric view of the FEM model of the Messina Bridge displaying the first torsion mode (asymmetric).

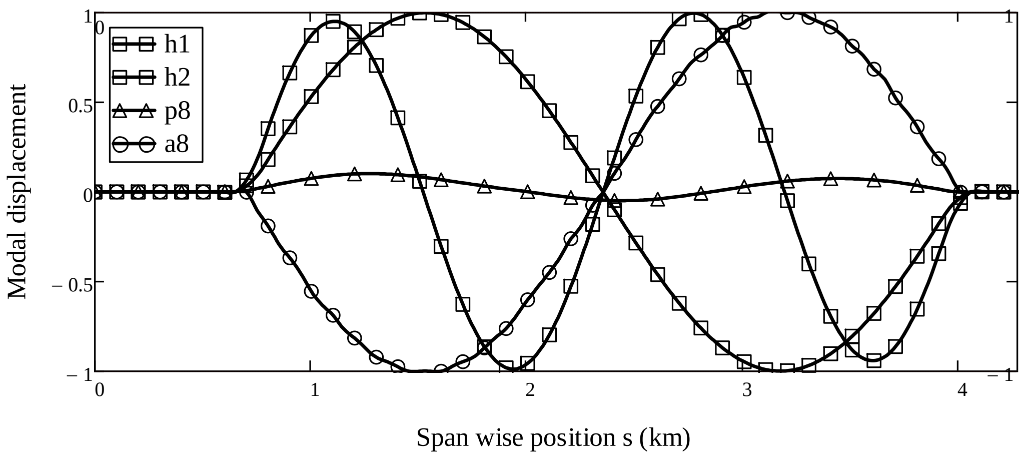

Figure 6.13 Vertical $h1, h2$, horizontal $p8$ and torsion mode shapes $\alpha 8$ considered for the Messina Bridge flutter analysis. Mean wind displacement at mid span = 11.0 m.

The Messina Bridge is equipped with large wind screens with airfoil dampers at the outer edges of the cantilevered maintenance service lanes and solid noise barriers running along the central railway girder. This configuration yields a relatively high drag coefficient which in turn results in a horizontal static mean wind displacement of approximately 11 m at the design wind speed of 54 m/s.

As in the case of the Izmit Bridge the horizontal mean wind deflection produces a horizontal component of the governing asymmetric torsion mode (mode p8 in Figure 6.13). From Figure 6.14 it is noted that the horizontal component of the torsion mode has virtually no influence on the critical wind speed which is identified as U_c = 87.5 m/s in case the horizontal aerodynamic derivatives are included or omitted from the analysis.

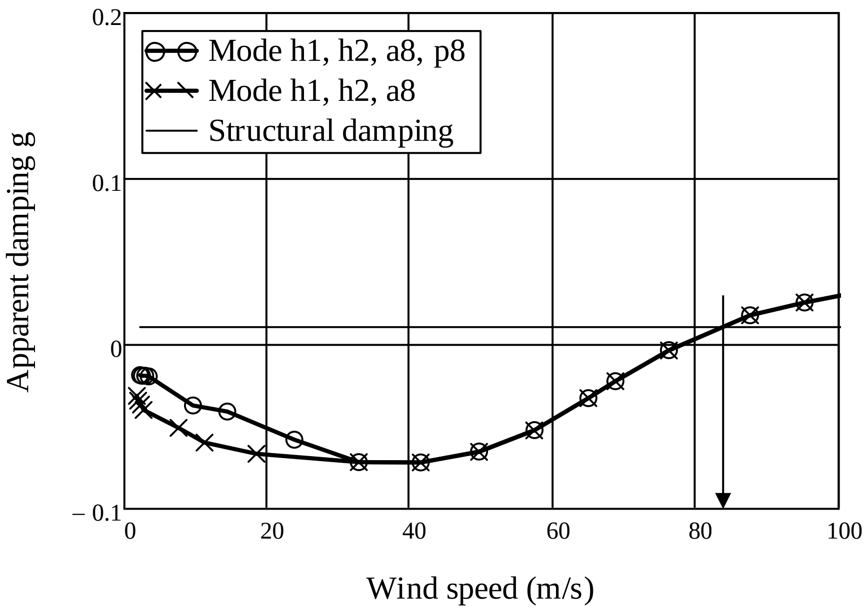

Figure 6.14 Result of the 4 mode flutter analysis for the Messina Bridge with and without the horizontal aerodynamic derivatives. Mean wind deflection at mid span = 11.0 m

From Table 6.3 it is noted that the basic horizontal mode $p2$ is much closer in frequency to the fundamental torsion mode (a frequency ratio f_{p1}/f_α of 0.68) than is common in suspension bridges with torsional stiff closed box girders. For the Izmit Bridge f_{p1}/f_α is 0.2 as an example. The large wind screens which create substantial drag combined with the small frequency difference between the basic horizontal and the torsion mode raises some concern that the basic horizontal mode would influence the flutter wind speed of the bridge through aerodynamic coupling. This situation was investigated by introducing the first asymmetric horizontal mode in the analysis. The four modes thus considered in the analysis are shown in Figure 6.15. It is noted that the horizontal component $p8$ has been replaced by the first asymmetric horizontal mode $p2$.

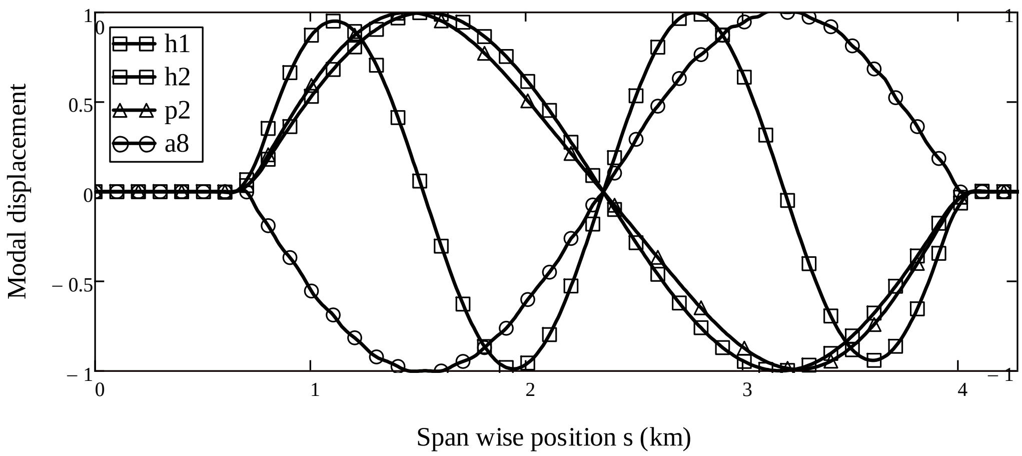

Figure 6.15 Vertical $h1, h2$, horizontal $p2$ and torsion mode shapes $\alpha 8$ considered for the Messina Bridge flutter analysis. Mean wind displacement at mid span = 11.0 m.

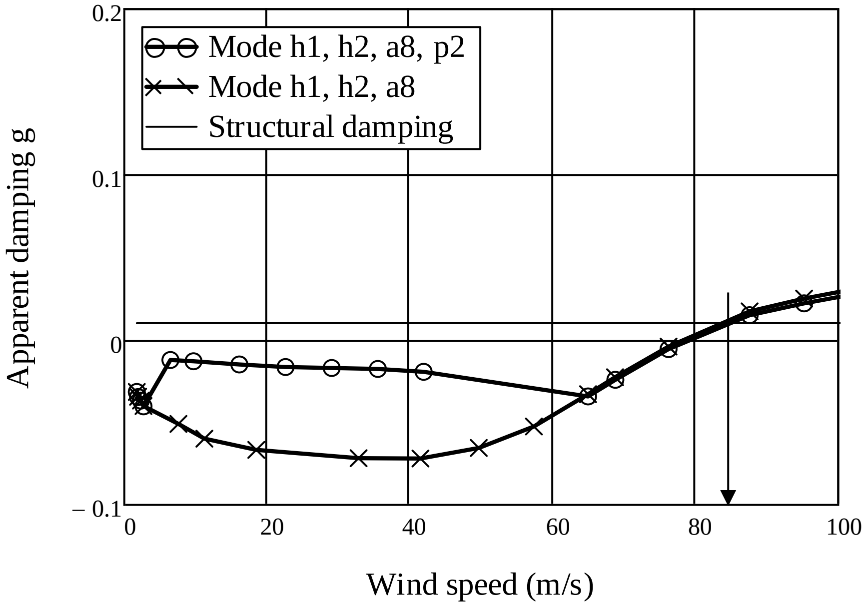

Figure 6.16 Result of the 4 mode flutter analysis for the Messina Bridge with and without the horizontal aerodynamic derivatives. Mean wind deflection at mid span = 11.0 m

From Figure 6.16 it is noted that the horizontal $p2$ mode has slightly more influence on the critical wind speed than the horizontal component of the torsion mode $p8$. The critical wind speed is identified as U_c = 89.5 m/s in case the horizontal aerodynamic derivatives are included. If the horizontal aerodynamic derivatives are omitted the critical wind speed becomes U_c = 87.5 m/s as in the $p8$ case discussed above. Assuming unity mode shapes for $h1$, $\alpha 8$ (section model) a critical wind speed U_c = 83 m/s is obtained.

Mode	*Eigenfrequency*	*Inertia*
1. Torsion (α8)	f_α = 0.081 Hz	I = 28.93·10^6 kgm^2/m
1. Vertical (h1)	f_{h1} = 0.065 Hz	m = 58.1·10^3 kg/m
2. Vertical (h2)	f_{h2} = 0.125 Hz	m = 58.1·10^3 kg/m
1. Horizontal (p1)	f_{p1} = 0.055 Hz	m = 58.1·10^3 kg/m
2. Horizontal (p8)	f_{p2} = 0.081 Hz	m = 58.1·10^3 kg/m

Table 6.3 Messina Bridge dynamic properties applied in the flutter analysis.

6.6 Conclusion of the three-degree-of-freedom flutter analyses

The three-degree-of-freedom flutter analyses presented in the preceding sections demonstrates that the horizontal degree-of-freedom has little influence on the flutter speed of the three cable supported bridges considered. In fact inclusion of the horizontal $p2$ for the Messina case yielded slightly higher critical wind speeds than if the horizontal mode was omitted from the analysis. This conclusion is perhaps surprising in view of the experience quoted by Miyata [11] for the Akashi-Kaikyo Bridge where flutter occurred at a lower wind speed when horizontal modes were included.

An illustration of the reason why the horizontal aerodynamic derivatives does not contribute much to the predicted flutter speeds of the cases discussed above can be given by assessing the relative importance of the torsion and horizontal aerodynamic dynamic derivatives. An estimate of the torsion frequency ratio squared which defines the loss of stiffness in torsion and aerodynamic damping can be obtained by considering the torsion equation of motion similar to (5.52) but retaining only the α and p degrees-of-freedom:

$$\left(\frac{\omega_\alpha}{\omega}\right)^2 \approx 1 + \frac{\rho B^4}{I^*} C_{\alpha\alpha} A_3^* \left[1 + \frac{C_{\alpha p} A_6^*}{C_{\alpha\alpha} A_3^*} \frac{p}{B\alpha} + \right] \tag{6.5}$$

$$g \approx \left(\frac{\omega}{\omega_\alpha}\right) \frac{\rho B^4}{I^*} C_{\alpha\alpha} A_2^* \left[1 + \frac{C_{\alpha p} A_5^*}{C_{\alpha\alpha} A_2^*} \frac{p}{B\alpha} + \right] \tag{6.6}$$

The mode shape coefficients and the aerodynamic derivatives appearing in (5.70) and (6.6) for the Izmit and Messina bridges examples ($p2$ mode included for the Messina case) are listed in Table 6.4.

	$C_{\alpha\alpha}$	$C_{\alpha p}$	$(U/fB)_c$	A_3^*	A_6^*	A_2^*	A_5^*
Izmit	0.245	-0.028	10	1.51	0.005	-0.47	0.04
Messina	0.389	-0.377	20	2.29	-0.014	-0.7	-0.13

Table 6.4 Mode shape coefficients and aerodynamic derivatives at the critical wind speed (Izmit $U/fB = 10$, Messina $U/fB = 20$).

Assuming that at flutter the amplitude ratio $p/B\alpha \approx 1$, the numerical value of the relative contribution of the horizontal mode at flutter is evaluated as shown in Table 6.5. In case of Izmit Bridge the estimated effect of the horizontal mode on stiffness and aerodynamic damping is less than 1% which is the likely reason that the critical wind speed is not affected by inclusion of the horizontal mode. For the Messina Bridge an 18% difference is noted on the aerodynamic damping which is in line with slight increase of the critical wind speed obtained when the horizontal mode is included.

	$(U/fB)_c$	$C_{\alpha p}A_6^*/C_{\alpha\alpha}A_3^*$	$C_{\alpha p}A_5^*/C_{\alpha\alpha}A_2^*$
Izmit	10	$-3.78\cdot10^{-4}$	$9.73\cdot10^{-3}$
Messina	20	$5.93\cdot10^{-3}$	$-1.8\cdot10^{-1}$

Table 6.5 Relative contribution of the horizontal terms to the stiffness and aerodynamic damping at flutter for the Izmit and Messina bridges.

Based on the cases studied above is it concluded that inclusion of horizontal modes in the flutter calculations are not significant for common cable supported bridges with single or tri- box girder decks. If any the effect of including the horizontal mode is to slightly increase the critical wind speed compared to a classical two-degree-of-freedom analysis. It is noted that the cable supported bridges considered in the present analysis are bridges having very long spans and thus are characterized by relatively small structural coupling between the individual modes. The above conclusion may not hold for some smaller contemporary cable supported foot bridges which sometimes are built with pronounced curvature in the horizontal plane of the deck.

References

[1] Provis, W.A. Observations on the effects produced by wind on the suspension bridge over the Menai Strait. *Transactions of the Institution of Civil Engineers*. Vol. III. London, 1842.

[2] Amman, O.H., von Kármán, Th., Woodruff, G.B. The failure of the Tacoma Narrows Bridge. *A report to the Honorable John H. Carmody, Administrator Federal Works Agency, Washington D.C.* Pasadena, CA, March 28, 1941.

[3] Farquharson, F.B. et al. Aeroelastic stability of suspension bridges with special reference to the Tacoma Narrows Bridge, part I-V. *University of Washington Experimental Station.* Bulletin 116, 1949-54.

[4] Bleich, F. Dynamic instability of truss-stiffened suspension bridges under wind action. *ASME Transactions, paper no. 2385.* 1177-1232, October 1948.

[5] Theodorsen, T. General theory of aerodynamic instability and the mechanism of flutter. NACA TR 496, 1935. *Classical Aerodynamic Theory. Jones, R.T. (ed) NASA Reference Publication 1050,* 1979.

[6] Selberg, A. Oscillation and aerodynamic stability of suspension bridges. *Acta Polytechnica Scandinavia. Civil engineering and building construction series no. 13.* Trondheim 1961.

[7] Frandsen, A.G. Wind stability of suspension bridges. *International symposium on suspension bridges. Laboratórió Nacional de Engenharia Civil, paper no. 43.* Lisboa 1966. Also published as *Publication IX, Bygningsstatiske Meddelelser Vol. 41 no. 2.* Copenhagen 1970.

[8] Scanlan, R.H. and Tomko, J.J. Airfoil and Bridge Deck Flutter Derivatives. *J. Eng. Mech., ASCE* (97) EM6, 1717-1737, 1971.

[9] Larsen, A. Walther, J: Aeroelastic analysis of bridge girder sections based on discrete vortex simulations. *Journal of Wind Engineering and Industrial Aerodynamics*. 67&68 (253 – 265). 1997.

[10] Schewe G. Nonlinear flow-induced resonances of an H-shaped cross section. *Journal of Fluids and structures*. 3 (327 – 348). 1983.

[11] Miyata, T. Historical review of long-span bridge aerodynamics. *Journal of Wind Engineering and Industrial Aerodynamics*. 91 (1393 – 1410). 2003.

[12] Kubo, Y., Hirata, K., Mikawa, K. Mechanism of aerodynamic vibrations of shallow bridge girder sections. *Journal of Wind Engineering and Industrial Aerodynamics*. 41 - 44 (1297- 1308). 1992.

[13] Larsen, A. Aerodynamics of the Tacoma Narrows Bridge – 60 years later. *Structural Engineering International.* Science and technology 4/2000.

[14] Scott, R: In the wake of Tacoma. *ASCE Press*. 2001.

[15] Hobbs, R.S. *Catastrophe to Triumph. Bridges of the Tacoma Narrows*. Washington State University Press. 2006.

[16] Green, D. Unruh, W.G. The failure of the Tacoma Narrows Bridge: A physical model. *American Journal of Physics.* 74 (8), August. 2006.

[17] Sapkaya, T. Computational methods with vortices - The 1988 Freeman Scholar Lecture. *ASME Journal of Fluids Engineering*. Vol. 111. March 1989

[18] Schraub, F.A., Kline, S.J., Henry, J., Runstadler, P.W. and Littell, A. Use of Hydrogen Bubbles for Quantitative Determination of Time-Dependent Velocity Fields in Low-Speed Water Flows. *Journal of Basic Engineering*. Transactions of the ASME, 1965, 429-444.

[19] Nakamura, Y., Nakashima, M. Vortex excitation of prisms with elongated rectangular, H and T cross-sections. *Journal of Fluid Mechanics*, vol. 163, 149-169, 1986.

[20] Billah, Y.K., Scanlan, R.H. Resonance, Tacoma Narrows Bridge failure and undergraduate textbooks. *American Journal of Physics.* 59 (2), February. 1991.

[21] Abramowitz, M. Stegun, I. A.: *Handbook of mathematical functions.* Dover Publications, New York, 1970.

[22] Fung, Y.C. *An introduction to the theory of aeroelasticity*. Dover Publications, New York, 1993.

[23] Zasso, A. Flutter derivatives: Advantages of a new representation convention. *Journal of Wind Engineering and Industrial Aerodynamics*. 60 (35 – 47). 1996.

[24] Jakobsen, J.B. Hjort-Hansen, E. Arne Selberg´s formula for flutter speed in light of multimodal flutter analysis. *Proceedings of the 12th International Conference on Wind Engineering*, Cairns, Australia, vol. 1, pp. 143-150. 2007.

[25] Richardson, J.R.. 1981: The development of the concept of the twin suspension bridge. *National Maritime Institute, R 125.* 1981.

[26] Jones, N.P., Scanlan, R.H., Aurang, J. and Katuchi, H., 1998. Advances (and challenges) in the prediction of long span bridge response to wind. In *Bridge Aerodynamics, Larsen and Esdahl (ed.) Balkema, Rotterdam.*

[27] Simiu, E. Scanlan, R.H.: *Wind Effects on Structures, second edition.* John Wiley & Sons, New York. 1986.

[28] Larsen, S.V., Sinding, P., Smitt, L.W., 2002. Extraction of aerodynamic flutter derivatives in newly developed forced motion rig with 3 degrees-of-freedom. *Proceedings, 13th International Conference on Wind Engineering.*

Symbols

$A^*_{1..6}$	Aerodynamic derivatives torsion degree of freedom
$H^*_{1..6}$	Aerodynamic derivatives vertical degree of freedom
$P^*_{1..6}$	Aerodynamic derivatives horizontal degree of freedom
B, b	Over all width of bridge deck
C_L	Lift coefficient $L_{ae}/½\rho U^2 B$
C_M	Moment coefficient $M_{ae}/½\rho U^2 B^2$
I	Deck section mass moment of inertia
K	Non-dimensional frequency $\omega B/U$
L	Span length
D_{ae}	Self-excited (motion induced) section drag force
L_{ae}	Self-excited (motion induced) section lift force
M_{ae}	Self-excited (motion induced) twisting moment
R	Radius of gyration
U, V	Mean wind speed
f, n, N	Frequency (Hz)
m	Deck section mass
i	Imaginary unit
$h, h(s)$	Vertical section displacement and mode shape
$p, p(s)$	Horizontal section displacement and mode shape
$\alpha, \alpha(s)$	Angular(twist) section displacement and mode shape
s	Span wise coordinate
x	Coordinate in the direction of flow
ξ	Relative coordinate in the direction of flow
Γ	Bound circulation
γ	Wake vorticity
μ	Mass ratio $\rho B^2/m$

ρ	Air density
ω	Circular frequency (rad/s)
δ	Logarithmic decrement of damping
ζ	Viscous damping relative to critical
g	Apparent damping level

Appendix A. Evaluation of Work Supplied by Travelling Point Vortex

This appendix details the mathematical evaluation of equation (4.19) valid for the travelling point vortex.

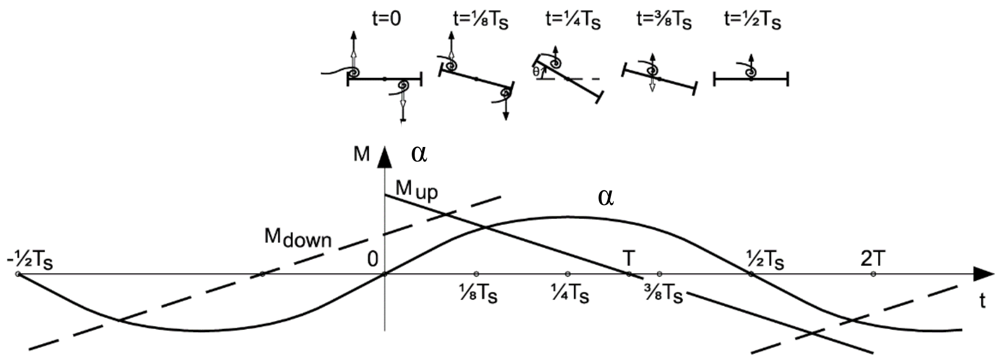

Figure A1 Model of the aerodynamic moment on cross section as function

The aerodynamic moment acting on the cross section during a half period (from t = 0 to t = $½T_s$) is composed of two components: The moment that is created when the cross section starts it's nose-up rotation at t = 0 (full line) and the moment that was created at previous time t = -$½T_s$ when the section started the nose-down rotation and still lingers (dashed line) as the half period is shorter than the time $2T$ it takes the vortices to travel from the upwind vertical girder to the downwind vertical girder.

The non-dimensional moment associated with the nose-up motion at t = 0 is proportional to the following function:

$$M_{up}(t) \simeq C_{M0}\left(1-\frac{t}{T}\right) \tag{A1}$$

Whereas the moment created at t = -$½T_s$ is proportional to:

$$M_{down}(t) \simeq C_{M0}\left(1-\frac{t+½T_s}{T}\right) \tag{A2}$$

The work supplied by the combination of the two vortices is obtained as the integration of the scalar product of moment and angular velocity over a half period:

$$W(T) \simeq \int_0^{½T_s}(M_{up}+M_{down})\cdot\dot{\alpha}dt = \int_0^{½T_s}(M_{up}+M_{down})\cdot \omega\cos(\omega t)dt \tag{A3}$$

Inserting (A1) and (A2) in (A3) and noting that $½T_s = \pi/\omega$ yields:

$$W(T) \simeq \int_0^{2T-\frac{\pi}{\omega}}\frac{\pi C_{M0}}{\omega T}\omega\cos(\omega t)dt + \int_{2T-\frac{\pi}{\omega}}^{\frac{\pi}{\omega}} C_{M0}\left(1-\frac{t}{T}\right)\cdot\omega\cos(\omega t)dt \tag{A4}$$

(A4) is evaluated as:

$$W(T) \simeq \frac{C_{M0}}{\omega T}(1-\cos(2\omega T)) - \sin(2\omega T) \tag{A5}$$

The above time integration over a half period of torsional oscillation $½T_s = \pi/\omega$ can be compared to integration of a single travelling point vortex over its travel time $2T$ across the deck:

$$W(T) \simeq \int_0^{2T} M_{up} \cdot \dot{\alpha} dt = \int_0^{2T} C_{M0}\left(1 - \frac{t}{T}\right) \cdot \omega\cos(\omega t) dt \qquad \text{(A6)}$$

(A6) is evaluated as:

$$W(T) \simeq \frac{C_{M0}}{\omega T}(1 - \cos(2\omega T)) - \sin(2\omega T) \qquad \text{(A7)}$$

Which is identical to (A5).

It is thus concluded that integration over a single vortex passage will supply exactly the same amount of work as integration of overlapping vortices over half an oscillation period.

(A5) or (A7) is finally cast into the form of (4.19) by inserting $T = 2B/U$.

Appendix B. Evaluation of circulation functions

The circulation functions discussed in 5.2 may be evaluated as given below.

The real and imaginary parts of the Theodorsen circulation function:

$$F(K) = \frac{J_1\left(\frac{K}{2}\right)\left(J_1\left(\frac{K}{2}\right)+Y_0\left(\frac{K}{2}\right)\right)+Y_0\left(\frac{K}{2}\right)\left(Y_0\left(\frac{K}{2}\right)-J_1\left(\frac{K}{2}\right)\right)}{\left(J_1\left(\frac{K}{2}\right)+Y_0\left(\frac{K}{2}\right)\right)^2+\left(Y_0\left(\frac{K}{2}\right)-J_1\left(\frac{K}{2}\right)\right)^2} \tag{B1}$$

$$G(K) = -\frac{Y_1\left(\frac{K}{2}\right)Y_0\left(\frac{K}{2}\right)+J_1\left(\frac{K}{2}\right)J_0\left(\frac{K}{2}\right)}{\left(J_1\left(\frac{K}{2}\right)+Y_0\left(\frac{K}{2}\right)\right)^2+\left(Y_0\left(\frac{K}{2}\right)-J_1\left(\frac{K}{2}\right)\right)^2} \tag{B2}$$

Where $J_0(x)$, $J_1(x)$ and $Y_0(x)$, $Y_1(x)$ are Bessel function of the first and second kind of order 0 and 1 respectively.

The real and the imaginary part of the "single vortex" circulation function:

$$f(K) = \frac{1-\left(\frac{K}{2}\right)Is\left(\frac{K}{2}\right)}{\left(1-\left(\frac{K}{2}\right)Is\left(\frac{K}{2}\right)\right)^2+\left(\left(\frac{K}{2}\right)Ic\left(\frac{K}{2}\right)\right)^2} \tag{B3}$$

$$g(K) = -\frac{\left(\frac{K}{2}\right)Ic\left(\frac{K}{2}\right)}{\left(1-\left(\frac{K}{2}\right)Is\left(\frac{K}{2}\right)\right)^2+\left(\left(\frac{K}{2}\right)Ic\left(\frac{K}{2}\right)\right)^2} \tag{B4}$$

Where the auxiliary functions $Is(x), Ic(x)$ are defined as follows:

$$Ic(x) = -\left(\frac{\pi}{2}\right)\sin\left(\frac{x}{2}\right)+Si\left(\frac{x}{2}\right)\sin\left(\frac{x}{2}\right)+Ci\left(\frac{x}{2}\right)\cos\left(\frac{x}{2}\right) \tag{B5}$$

$$Is(x) = -\left(\frac{\pi}{2}\right)\cos\left(\frac{x}{2}\right)+Si\left(\frac{x}{2}\right)\cos\left(\frac{x}{2}\right)-Ci\left(\frac{x}{2}\right)\sin\left(\frac{x}{2}\right) \tag{B6}$$

With Ci, Si being the cosine and sine integrals

$$Ci(x) = 0.57722+\ln(x)+\int_0^x \frac{\cos(t)-1}{t}\,dt \tag{B7}$$

$$Si(x) = \int_0^x \frac{\sin(t)}{t}\,dt \tag{B8}$$

Appendix C. Flutter Determinant, Theodorsens Method

Polynomial expansion of the two-mode flutter determinant following Thoedorsens method, section 5.5. Equation (81) can be expanded and split into the following algebraic equations:

Real part 4th order polynomial:

$$
\begin{aligned}
X^4 &\left(1 + \frac{\rho B^4}{I} A_3^* + \frac{\rho B^2}{m} H_4^* + \frac{\rho B^4}{I} \frac{\rho B^2}{m} (A_3^* H_4^* - A_2^* H_1^* - A_4^* H_3^* + A_1^* H_2^*)\right) \\
&+ X^3 \left(2\zeta_h \frac{\rho B^4}{I} A_2^* + 2\zeta_\alpha \left(\frac{\omega_\alpha}{\omega_h}\right)^2 \frac{\rho B^2}{m} H_1^*\right) \\
&+ X^2 \left(-\left(\frac{\omega_\alpha}{\omega_h}\right)^2 - 4\zeta_h \zeta_\alpha \left(\frac{\omega_\alpha}{\omega_h}\right) - 1 - \frac{\rho B^4}{I} A_3^* - \frac{\rho B^2}{m} H_4^*\right) \\
&+ \left(\frac{\omega_\alpha}{\omega_h}\right)^2 = 0
\end{aligned}
\tag{C1}
$$

Imaginary part 3th order polynomial:

$$
\begin{aligned}
X^3 &\left(\frac{\rho B^4}{I} A_2^* + \frac{\rho B^2}{m} H_2^* + \frac{\rho B^4}{I} \frac{\rho B^2}{m} (A_2^* H_4^* + A_3^* H_1^* - A_4^* H_2^* - A_1^* H_3^*)\right) \\
&+ X^2 \left(-2\zeta_h \left(1 + \frac{\rho B^4}{I} A_3^*\right) - 2\zeta_\alpha \left(\frac{\omega_\alpha}{\omega_h}\right)\left(1 + \frac{\rho B^2}{m} H_4^*\right)\right) \\
&+ X \left(-\frac{\rho B^2}{m} \left(\frac{\omega_\alpha}{\omega_h}\right)^2 H_1^* - \frac{\rho B^4}{I} A_2^*\right) + \left(2\zeta_h \left(\frac{\omega_\alpha}{\omega_h}\right)^2 + 2\zeta_\alpha \left(\frac{\omega_\alpha}{\omega_h}\right)\right) \\
&= 0
\end{aligned}
\tag{C2}
$$

Equations (C1), (C2) are usually solved by numerical iterative methods as function of non-the dimensional wind speed for which the aerodynamic derivatives are measured. The non-dimensional wind speed at which the root curves intersect defines the flutter point.

A useful first guess for the solution may be arrived at by setting the structural damping levels ζ_h, ζ_α equal to zero. In this case (C1), (C2) are reduced to second and first order equations for which the solution can be obtained analytically.

Appendix D. Aerodynamic derivatives for three bridge girder sections.

Vertical Aerodynamic Derivatives.

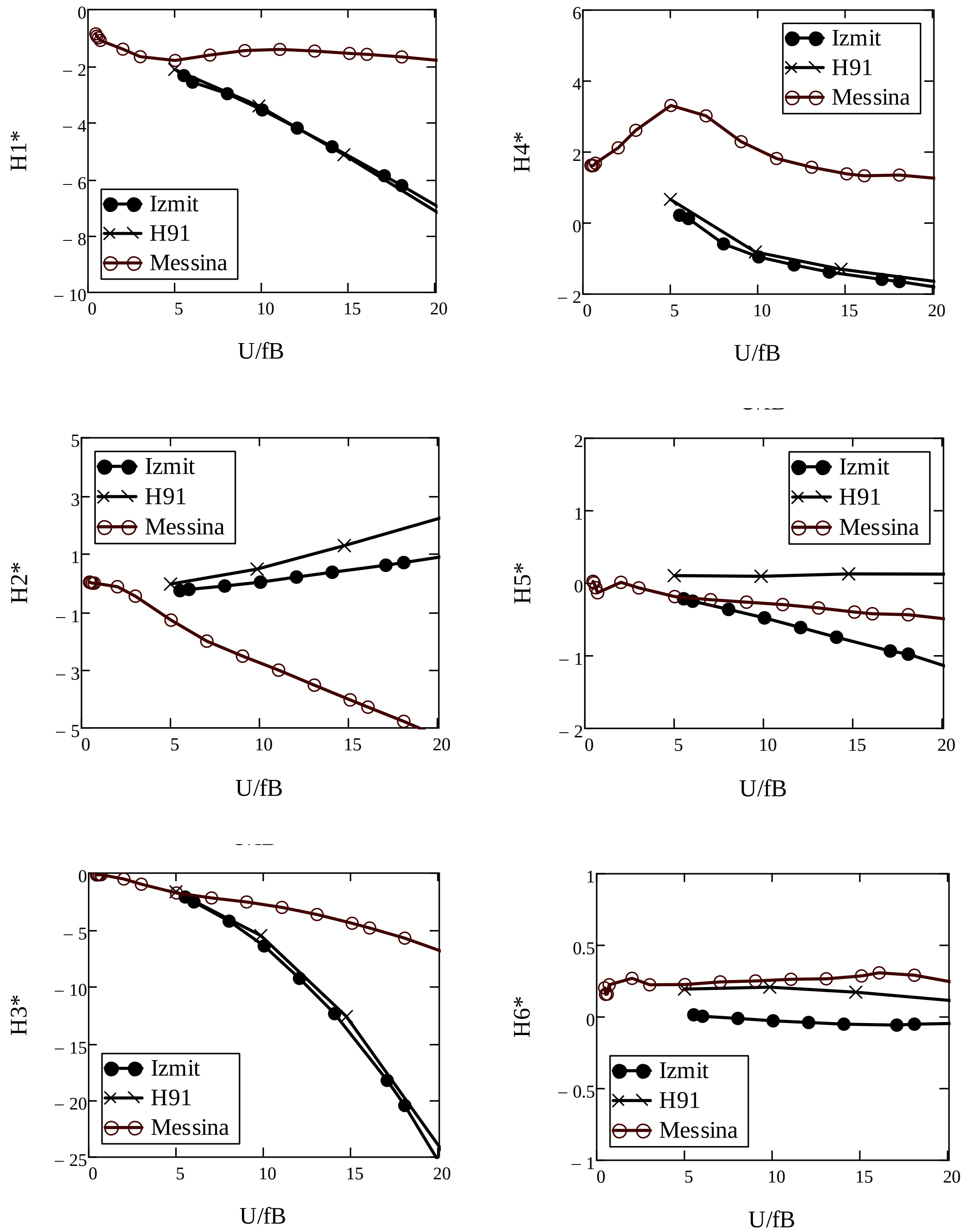

Torsion Aerodynamic Derivatives.

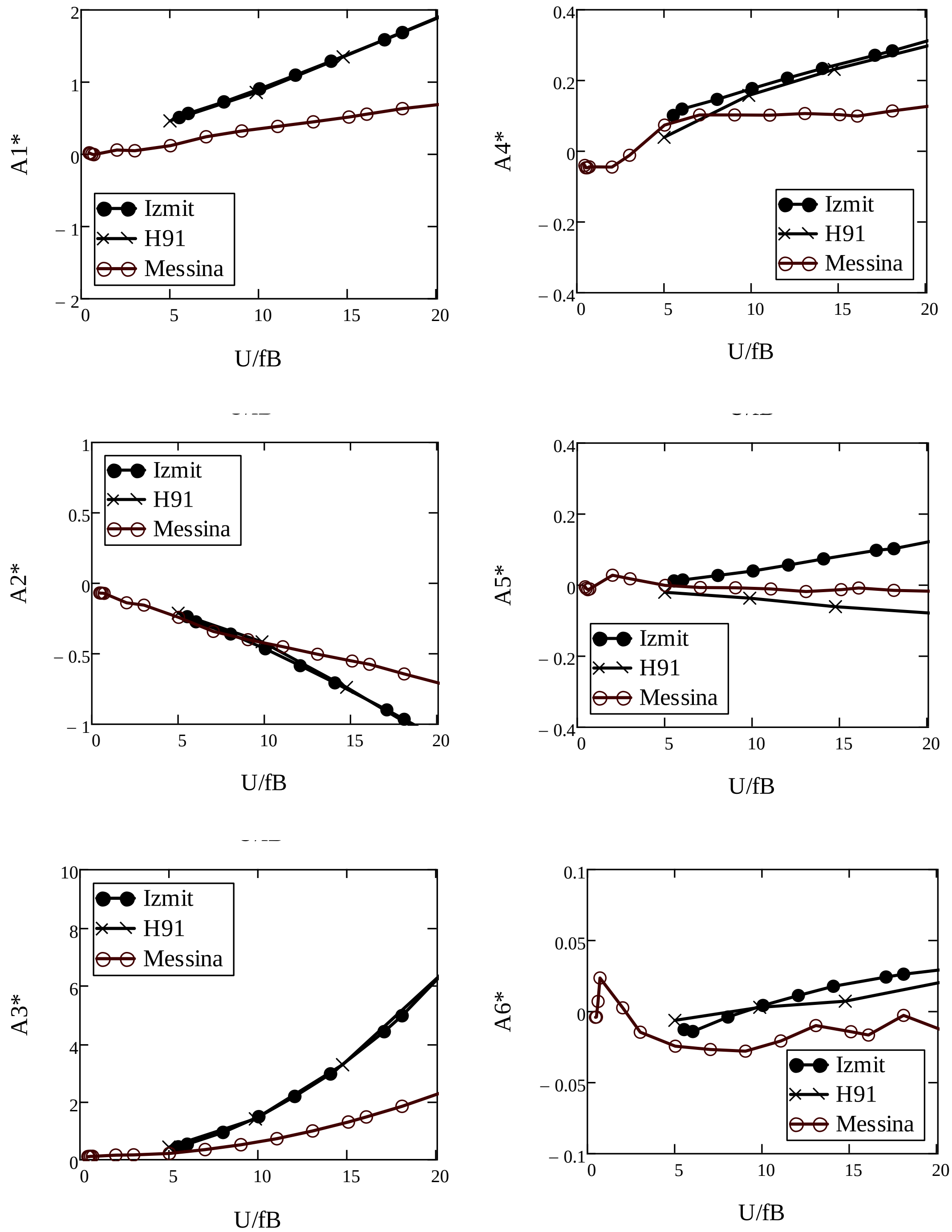

Horizontal Aerodynamic Derivatives.

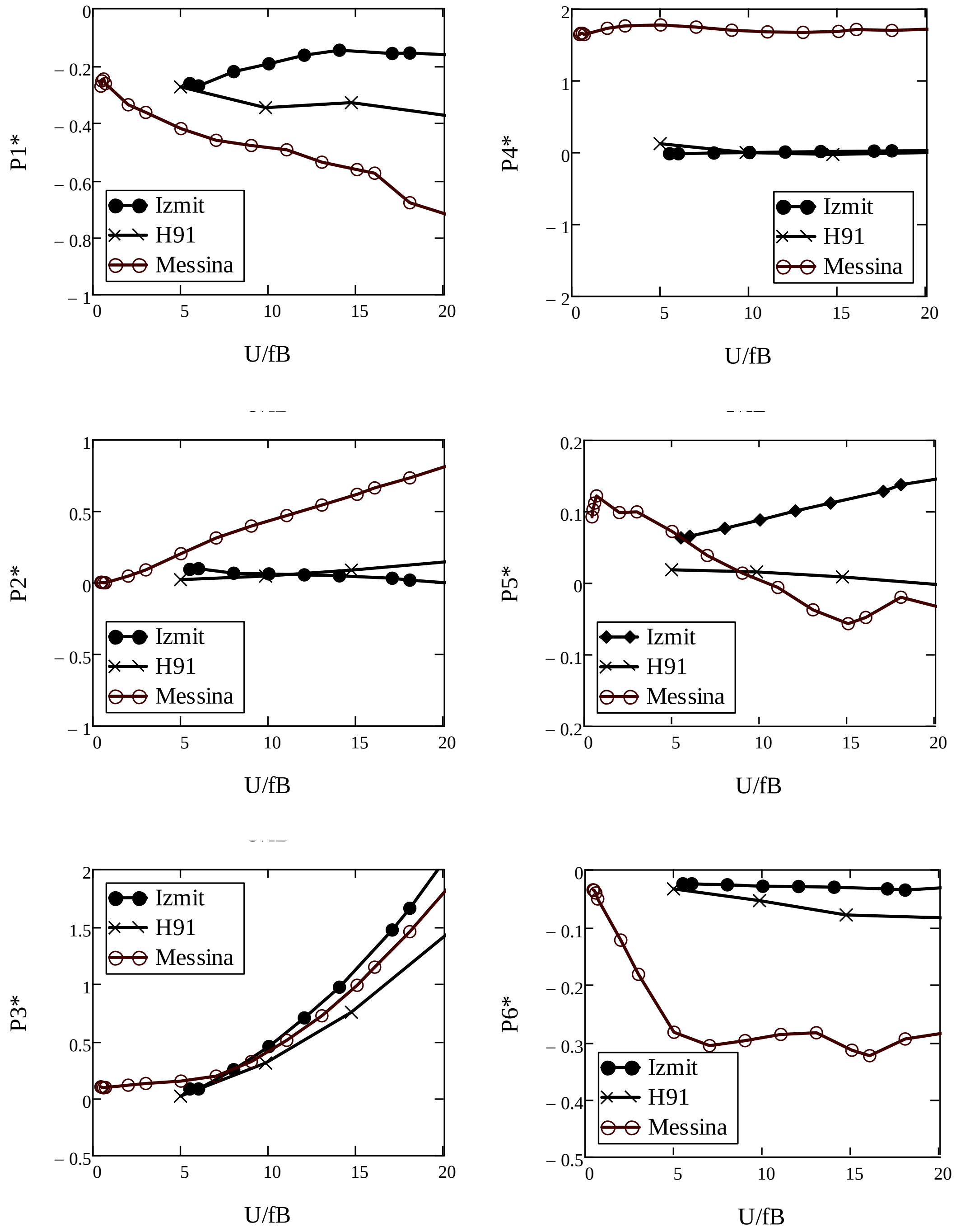

DANSK SELSKAB FOR BYGNINGSSTATIK

Anmodning om optagelse i selskabet indsendes til et af bestyrelsens medlemmer:

Linh Cao Hoang (formand). Tlf. 45 25 17 06
DTU, Institut for Byggeri og Anlæg. Brovej, 2800, Kgs. Lyngby

Niels Højgaard Pedersen (sekretær). Tlf. 72 44 75 34
Vejdirektoratet. Guldalderen 12, 2640 Hedehusene

Lars Krog Christensen (kasserer). Tlf. 70 12 24 00
MT Højgaard. Knud Højgaards Vej 9, 2860 Søborg

Uffe Graaskov Ravn. Tlf. 22 70 96 30
COWI A/S. Parallelvej 2, 2800 Kgs. Lyngby

Srirengan Thangarajah. Tlf. 29 40 32 19
Per Aarsleff A/S

Thomas Hansen. Tlf. 29 64 75 35
ALECTIA A/S. Teknikerbyen 34, 2830 Virum

Carsten Munk Plum. Tlf. 45 66 10 11
ES-Consult A/S. Sortemosevej 19, 3450 Allerød

Ronni Dam. Tlf. 51 61 61 19
RAMBØLL. Hannemanns Allé 53, 2300 København S

Selskabets formål er at arbejde for den videnskabelige udvikling af bygningsmekanikken - både teori for og konstruktion af alle slags bærende konstruktioner - fremme interessen for faget, virke for et kollegialt forhold mellem dets udøvere og hævde dets betydning overfor og i samarbejde med andre grene af ingeniørvidenskaben. Formålet søges bl.a. realiseret gennem møder med foredrag og diskussioner samt gennem udgivelse af ”Bygningsstatiske Meddelelser”.

Som medlemmer kan optages personlige medlemmer, firmaer og institutioner, som er særligt interesserede i bygningsmekanik, eller hvis virksomhed falder indenfor bygnings-mekanikkens område.

Det årlige kontingent er for personlige medlemmer 300 kr., for firmaer samt institutioner 1.800 kr. Studerende ved Danmarks Tekniske Universitet og andre danske ingeniørskoler samt indtil 2-års kandidater kan optages som juniormedlemmer uden stemmeret for et årskontingent på 80 kr. Pensionerede medlemmer med mindst 10 års medlemsanciennitet kan opnå status som pensionistmedlem med stemmeret for et årskontingent på 100 kr.

Selskabets medlemmer modtager frit ”Bygningsstatiske Meddelelser”, der udsendes kvartalsvis. Endvidere publiceres ”Bygningsstatiske Meddelelser” på Selskabets hjemmeside www.dsby.dk. Manuskripter til optagelse i ”Bygningsstatiske Meddelelser” modtages af redaktøren.